Microstructurally Explicit Simulation

of the Transport Behavior in Uranium Dioxide

by

Harn Chyi Lim

A Dissertation Presented in Partial Fulfillment
of the Requirements for the Degree
Doctor of Philosophy

Approved November 2014 by the
Graduate Supervisory Committee:

Pedro Peralta, Chair
Kiran Solanki
Hanqing Jiang

ARIZONA STATE UNIVERSITY

December 2014

ABSTRACT

Fission products in nuclear fuel pellets can affect fuel performance as they change the fuel chemistry and structure. The behavior of the fission products and their release mechanisms are important to the operation of a power reactor. Research has shown that fission product release can occur through grain boundary (GB) at low burnups. Early fission gas release models, which assumed spherical grains with no effect of GB diffusion, did not capture the early stage of the release behavior well. In order to understand the phenomenon at low burnup and how it leads to the later release mechanism, a microstructurally explicit model is needed. This dissertation conducted finite element simulations of the transport behavior using 3-D microstructurally explicit models. It looks into the effects of GB character, with emphases on conditions that can lead to enhanced effective diffusion. Moreover, the relationship between temperature and fission product transport is coupled to reflect the high temperature environment.

The modeling work began with 3-D microstructure reconstruction for three uranium oxide samples with different oxygen stoichiometry: $UO_{2.00}$ $UO_{2.06}$ and $UO_{2.14}$. The 3-D models were created based on the real microstructure of depleted UO_2 samples characterized by Electron Backscattering Diffraction (EBSD) combined with serial sectioning. Mathematical equations on fission gas diffusion and heat conduction were studied and derived to simulate the fission gas transport under GB effect. Verification models showed that 2-D elements can be used to model GBs to reduce the number of elements. The effect of each variable, including fuel stoichiometry, temperature, GB diffusion, triple junction diffusion and GB thermal resistance, is verified, and they are coupled in multi-physics simulations to study the transport of fission gas at different radial location of a fuel pellet. It was demonstrated that the microstructural model can be used to incorporate the effect of different physics to study fission gas transport. The results suggested that the GB effect is the most significant at the edge of fuel pellet where the temperature is the lowest. In the high temperature region, the increase in bulk diffusivity due to excess oxygen diminished the effect of GB diffusion.

ACKNOWLEDGMENTS

The work would not have been possible without the support of many people. First of all, I would like to acknowledge Dr. Pedro Peralta for the opportunity to work on this research project. The valuable experience of working under his guidance is greatly appreciated. I would also like to thank Dr. Karin Rudman for all the characterization work, Dr. Kapil Krishnan for the head start on the modeling work and Robert McDonald for the development of reconstruction procedures. The sharing of knowledge, work and fun in the office helped me meet all the deadlines and challenges in the past four years. Last but not least, I need to acknowledge Los Alamos National Lab for providing the samples and the funding for the work. This project is a part of the Advanced Fuel Cycle Initiative (AFCI) and the Fuel Cycle Research and Development (FCRD). This project was funded by Los Alamos National Laboratory (LANL), Award # DE-FC07-05ID14654 and ASU Fulton Fellowship.

TABLE OF CONTENTS

Page

LIST OF FIGURES ix

LIST OF TABLES xix

CHAPTER

1. INTRODUCTION 1

  1.1 Nuclear Power Overview 1

    1.1.1 History and Application 2

    1.1.2 Issues 4

    1.1.3 Current Status: new power plant (gen III and IV) 6

  1.2 Nuclear Physics Basics 8

    1.2.1 Nuclear Physics Basics 8

    1.2.2 Irradiation damage 10

  1.3 Nuclear Fuels 12

    1.3.1 Nuclear Fuels Overview 12

    1.3.2 Uranium Oxide Fuel Performance 15

    1.3.3 Fission Products 16

    1.3.4 Fuel Swelling and Microstructure Reconstruction 18

    1.3.5 Release of Fission Gases 21

1.3.6 Experimental Techniques 24

1.4 Motivation 25

2. LITERATURE REVIEW 27

2.1 UO_2 Properties 27

2.1.1 Thermal Properties 28

2.1.2 Fission Product Diffusivities 30

2.1.3 Stoichiometry Effect on Material Properties 33

2.2 Effects of Microstructure 37

2.2.1 Grain Boundary and Coincident Site Lattice 37

2.2.2 Grain Boundary Diffusion 40

2.2.3 Percolation Theory and Grain Boundary Networks 43

2.2.4 Grain Boundary Thermal Resistance 47

2.2.5 Effect of Triple Junctions 48

2.2.6 Defect Structure in Uranium Dioxide 51

2.3 Existing Fission Product Transport Models 53

2.3.1 Booth’s Model 53

2.3.2 Atomistic Simulation 55

2.3.3 Meso-scale Models and Percolation Theory 56

CHAPTER Page

3. OBJECTIVES 60

4. EXPERIMENTAL PROCEDURES AND CHARACTERIZATION RESULTS 63

4.1 Experimental Procedures 64

4.1.1 Sample Preparation 64

4.1.2 Microstructure Characterization Techniques 64

4.1.3 Three Dimensional Characterization Technique 67

4.2 Characterization Results 68

4.2.1 Microstructure Information in 2-D 69

4.2.2 Grain Boundary Misorientation Angle Distribution 70

4.2.3 Characterization Results from 3-D Reconstruction 72

4.3 Triple Junction Study and Grain Boundary Connectivity 77

4.3.1 Dihedral Angle at Triple Junctions 77

4.3.2 CHomP Study of Connectivity 80

5. FINITE ELEMENT MODEL DEVELOPMENT AND SIMULATION PROCEDURES 84

5.1 Model Reconstruction 84

5.1.1 Microstructure Reconstruction 84

5.1.2 Reconstructed 3-D Models 88

5.2 Analytical Approach 92

    - 5.2.1 Governing Equations 92
    - 5.2.2 Modeling Grain Boundary Diffusion 93
    - 5.2.3 Grain Boundary Thermal Resistance 96
  - 5.3 Simulation Parameters 99
    - 5.3.1 Fission Gas Diffusivity 99
    - 5.3.2 Grain Boundary Diffusivity and Effective Grain Boundary Diffusion 103
    - 5.3.3 Heat and Mass Generation Rate 106
    - 5.3.4 Temperature Profile 107
    - 5.3.5 Concentration Profile 110
    - 5.3.6 Boundary Conditions 114
    - 5.3.7 Effective Grain Boundary Diffusivity 115
- 6. SIMULATION RESULTS AND DISCUSSION 121
  - 6.1 Bicrystal Model Verification 121
    - 6.1.1 Grain Boundary Diffusion Verification 121
    - 6.1.2 Grain Boundary Thermal Resistance: Bicrystal Verification 124
  - 6.2 Controlling Parameters 126
    - 6.2.1 Baseline 3-D Microstructure Models 126
    - 6.2.2 Triple Junction Diffusion 133

6.2.3 Stoichiometry Effect 136

6.2.4 Temperature Effect 139

6.2.5 Effects of Heterogeneous Grain Boundary Properties 144

6.2.6 Mass Generation 152

6.2.7 Grain Boundary Kapitza Resistance in Polycrystalline Models 154

6.3 Multi-Physics Effects on Fission Product Transport 157

6.3.1 Microstructurally Explicit Simulation of $UO_{2.00}$, $UO_{2.06}$ and $UO_{2.14}$ 158

6.3.2 Sensitivity Analysis 163

7. CONCLUSIONS AND FUTURE WORKS 170

7.1 Conclusions 170

7.2 Future Work 173

REFERENCES 175

LIST OF FIGURES

Figure Page

1-1: Nuclear Electricity Production over the Years [1] 3

1-2: Illustrations of (a) Fission Reaction (b) Fusion Reaction... 9

1-3: (a) Fluorite Crystal Structure (b) UO_2 Fuel Pellet with a Diameter of about 1cm [11] 13

1-4: Tri-Structural Isotropic (TRISO) Fuel for VHTR 14

1-5: Fuel Assembly Illustration (a) the Layout of an Individual Fuel Rod (b) Pressurized Water Reactor Fuel Assembly [2]... 15

1-6: The evolution of fuel elements that lead to pellet- cladding interaction [2] 19

1-7: An Illustration of a Reconstructed Microstructure of a Fuel Rod Cross Section Irradiated in a Fast Reactor [6] 20

1-8: Fission Gas Bubbles Forming in the Grains and Coalesce in GBs [6]...................... 22

1-9: Fission Gas (^{88}Kr) Release to Birth Ratio (R/B) with Respect to Irradiation Time in Week in x: Small Grains and o: Large Grains [20] 23

1-10: Diagrams to Illustrate (a) In-pile Experiment and (b) Post Irradiation Heat Treatment [6] 25

2-1: Experimental Data for Thermal Conductivity of UO_2 [22]. 30

2-2: Oxygen Redistribution Results from Both Calculation and Experiments for $(U,Pu)O_{2+x}$ [6]. 34

Figure Page

2-3: The Change in Thermal Conductivity with O/M Ratio and Temperature for $U_{0.8}Pu_{0.2}O_{2\pm x}$ [6]. 35

2-4: Variation of D_{Xe} with Stoichiometry in UO_2 Powders [25]. 36

2-5: Variation of D_{Xe} with Sample Stoichiometry in UO_2 Powder [38]........................... 36

2-6: Relative GB Energy Data for Al and Cu for a Symmetric [100] Tilt Boundary That Shows the Increase in Energy with Misorientation Angle [43]. 38

2-7: Structure of Σ5 Tilt Boundary at (310) Plane in [001] Direction [44]. 39

2-8: The GB Energy at Different Misorientation Angles for a Ceramic (a) [110] Tilt (b) [100] Twist [43]. 39

2-9: A Micrograph of a UO_2 Grain Showing Different Pore Shapes at Different GBs [45]. 40

2-10: A Sketch that Illustrates the GB Diffusion Model Described by Fisher [50]. 41

2-11: Schematic Illustrations of Type A, B and C Boundary Diffusion in a Polycrystalline Material [50]. 42

2-12: The Concentration Profile with (a) Low Diffusivity Contrast GBs (b) High Diffusivity Contrast GBs under a Fixed Concentration Gradient.................................... 45

2-13: Normalized Effective Diffusivity Change with High Diffusivity GB Fraction (p) for Different Diffusivity Contrast. 46

Figure Page

2-14: Early Stage of Porosity Formed by Fission Gas Formation at a UO_2 Fracture Surface Taken by SEM. The Size Difference Between Pores at TJs and GBs Can Be Differentiated. The Circled Areas Are Quadruple Points Where Three TJs Meet. [45]. . 49

2-15: (a) Three GBs Intersecting at a Triple Junction Reveals Three Dihedral Angles (b) The Possible Combinations of GBs That Satisfy Crystallographic Constraints at a TJ Defined in [68]. 50

2-16: General GB Network in Irregular Lattice (a) A Randomly Generated GB Network (b) a GB Network with Crystallographic Constraints [70]. 51

2-17: Relative Partial Free Energies of Oxygen, ΔG_{O2}, of UO_{2+x}, as a Function of -log(x). The Variable *n* Denotes the Exponent in the $pO_2^{1/n}$ [39]. 52

2-18: An Illustration of Booth’s Model for Fission Gas Release. [74]............................ 54

2-19: Examples of Meso-scale Models (a) FG bubble Evolution at a GB [79] (b) Bubble Enhanced Thermal Resistance at GBs [80]. 56

2-20: (a) Diffusion Flux from the Simulation Result in a 2-D Microstructure with Diffusivity Ratio of 10^6, 10^7 (From Left to Right) [81] (b) 2-D GB Networks Used to Study the Percolation of Saturated GBs... 58

2-21: Effective Diffusivity under as a Function of Diffusivity Contrast for the Simulation in 2-D Microstructure [81]... 59

4-1: SEM and EBSD Image for a Porous UO_2 Sample Showing the Crystallography Orientation and the Types of Special GBs... 63

Figure Page

4-2: An Illustration of the OIM Technique [85]. 66

4-3: Examples of the Images Obtained from SEM and EBSD (a) SEM Image of a Sample Undergoing Serial Section Along the Vertical Direction. A Fiducial Mark Was Made in the Lower Right Corner. (b) Image Quality Map from EBSD. (c) Orientation Map from EBSD [84].. 66

4-4: Measuring GB Normals by Making Tangential Cut Planes Along the GBs Using AVIZO^{TM}. 68

4-5: Distribution of Grain Size of the Samples with Different O/M Values from 2-D Data [83]. 70

4-6: Grain Boundary Misorientation Angle Distribution (a) $UO_{2.00}$ (b) $UO_{2.06}$ (c) $UO_{2.14}$ [84]. 71

4-7: Coincident Site Lattice Distribution for Both $UO_{2.00}$ and $UO_{2.06}$ Samples [84]. 72

4-8: Serial Sectioned Microstructure of $UO_{2.14}$ Sample [84]. 73

4-9: 3-D Microstructure Reconstructions for Different Samples: (a) $UO_{2.00}$ (b) $UO_{2.06}$ (c) $UO_{2.14}$. 74

4-10: 3-D Grain Size Distribution for (a) $UO_{2.00}$ (b) $UO_{2.06}$ (c) $UO_{2.14}$............................ 75

4-11: Selected Slices from FIB Serial Sectioning Set of Sample $UO_{2.00}$ for Calculating Grain Size across Thickness 76

Figure Page

4-12: (a) A Triple Junction Surround by 3 Grains, g_A, g_B, g_C and 3 GBs, $b_{1,}$ b_2 and b_3. X Represents the Dihedral to the Corresponding GB [89] (b) Dihedral Angle Measurement from a 2-D EBSD Data 78

4-13: The Distribution of Dihedral Angles at Triple Junctions for a 95% Density UO_2 Sample.. 79

4-14: A Histogram for 3-D Dihedral Angle Pairs: X-axis Is a Dihedral Angle Measured at a TJ, and Y-axis Is the Corresponding Dihedral Angle at the Same TJ. 80

4-15: (a) Percolation Paths in Different 2-D GB Networks (b) The Resulting Concentration Distribution from the Percolation Paths [81]. 81

4-16: Examples of the GB Networks for ChomP Analysis (a) A Fully Connected Network Including All GBs (b) A Network with Only High Diffusivity GBs................ 82

4-17: The Flux Profiles from Figure 4-15 after Threshold to Show Only High Flux GBs. The Figures Are Listed in the Same Order as Figure 4-15. 83

5-1: Examples of the Process for 3-D Microstructure Reconstruction: (a) Stacking Two Identical EBSD Maps (b) Labeling Grains in AVIZO^{TM} (c) GB Network Obtained from the Labels (d) 3-D Microstructure. 86

5-2: Meshed Geometry for the 2-D Simulation [81]. 87

5-3: A GB Network Meshed with 2-D Elements. 88

5-4: Meshed Model for the Three Samples (a) $UO_{2.00}$ (b) $UO_{2.06}$ (c) $UO_{2.14}$.................... 89

Figure Page

5-5: Grain Size Distributions for the Three Reconstructed and Meshed Models. The x-axis Has a Unit in μm.. 92

5-6: Fission Gas Diffusivities from Different Researchers (log D vs T)........................ 100

5-7: Stoichiometry Effect on Xe Diffusivity Based on Equations in [25]. The Results Are Compared with the Diffusivity from Davies and Long [98].. 102

5-8: Stoichiometric Effect on Xenon Diffusivity Measured by Matzke (Plot Reproduced from [38]), Comparing with Miekeley's Work [25]... 103

5-9: Fission Gas Diffusivity in the bulk (Davies and Long only) and in Grain Boundaries. Plots Based on the Equations Derived in [34, 102, 104]... 105

5-10: Grain Boundary Properties and Their Relationship to Misorientation Angles [105]. 106

5-11: Temperature Profile across the Radius of a Fuel Pellet. 110

5-12: Spherical Sink in a Fuel Pellet for Calculating the Concentration Profile [6]. 111

5-13: Concentration Profile close to a Spherical Sink.. 112

5-14: Xenon Concentration across the Radius of a UO_2 Fuel Pellet that Was Irradiated to about 2% Burnup [107]... 113

5-15: (a) A Finite Element Model that Simulates a Section of a Cylindrical Fuel Pellet Sandwiched between Two Radial Cracks; *C*: Concentration, *T*:Ttemperature (K), *q*: Heat Flux. (b) The Obtained Radial Concentration Profile.. 114

Figure Page

5-16: Schematic of Boundary Conditions Set-up. *T*: Temperature, *C*: Concentration, *j*: Mass Flux, *q*: Heat Flux, *H*: Heat Generation rate, *F*: FG Generation Rate.................. 115

5-17: (a) A Fractograph Showing FG Bubbles at GB for a UO_2 Sample Irradiated to 1.3% Followed by a Heat Treatment [108] (b) Schematic to Illustrate the Relationship between Bubble Size and Bubble Density [102]... 116

5-18: Square and Hexagonal Bubble Distribution in a 10 μm by 10 μm Area GB for Effective GB Diffusivity Calculation. 117

5-19: Effective GB Diffusivity for Both (a) Square and (b) Hexagonal Bubble Distribution as Different Bubble Radius... 119

6-1: Bicrystal Models with GB Meshed with (a) 2-D Elements (b) 3-D Elements. 122

6-2: The Concentration Profile for Bicrystal Model with a GB Treated as (a) 2-D (b) 3-D (c) Concentration Profiles across the GBs for both models... 123

6-3: Modeling Diffusion along TJs using 1-D edge Elements. 124

6-4: (a) Boundary Conditions of the Bicrystal Model Used to Verify the Effect of Kapitza Resistance. *C*: Concentration, *T*: Temperature, *q*: Heat Flux. (b) Resulting Temperature Profiles Close to the Top Boundary (High Concentration region) and Bottom Boundary (Low Concentration Region) 125

6-5: 3-D Finite Element Simulation Showing the Effect of High Diffusivity Grain Boundaries on the Diffusion of Fission Products (a) $UO_{2.0}$ (b) $UO_{2.06}$ (c) $UO_{2.14}$.......... 128

6-6: Vertical Concentration Profiles along a Cut Line across the Three Models. 130

Figure Page

6-7: Magnitude of Concentration Gradient in Two Perpendicular Cut Planes Containing the $UO_{2.00}$ Concentration Line Plotted in Figure 6-6, as Marked by the Red Lines....... 131

6-8: The Concentration Profile along the Black Line in Figure 6-7 Showing Different Slopes Due to Differences in Microstructure.. 132

6-9: Triple Junctions in the $UO_{2.14}$ Microstructure Labeled with Blue Lines................ 134

6-10: The Concentration Profiles along a Vertical Line with and without TJ Diffusion in the (a) $UO_{2.14}$ and (b) $UO_{2.00}$ Microstructure. 136

6-11: (a) Concentration Profile of a Vertical Cut Line across the $UO_{2.00}$ Model, Comparing between the Two Simulations using the Bulk Diffusivity from Miekeley and Davies and Long (Baseline Model). (b) Concentration Profile in a Horizontal Plane 5 μm Away from the Bottom Surface from the Simulation Using Miekeley's Diffusivity..... 138

6-12: Ratio Between Grain Boundary Diffusivity and Bulk Diffusivity. The Values Are Based on Davies and Long (Bulk) and Calculation from Olander (GB)........................ 140

6-13: (a) The Two Vertical Lines Indicating the Locations the Line Profiles Are Plotted with Line1 on the Left and Line2 on the Right. (b) The Vertical Concentration Profiles along the Two Vertical Lines in (a) Comparing the Effect of the Temperature Gradient with the Base Simulation in the $UO_{2.00}$ Microstructure. 141

6-14: The Linear Concentration Profiles under the Effect of a Constant Temperature, a Forward Temperature Gradient and a Reverse Temperature Gradient........................... 143

Figure Page

6-15: The Concentration Profiles under the Influence of High Temperature (1600 K – 1570 K) and Low Temperature (830 K – 800 K). The Reference Line Is a Straight Line Representing a Perfectively Uniform Concentration Gradient. 144

6-16: The Distribution of GBs Assigned with a High Diffusivity Value and the Resulting Surface Concentration Profiles for Sample (a) $UO_{2.00}$ (b) $UO_{2.06}$, (c) $UO_{2.14}$. 145

6-17: The Cross Sectional Concentration Profiles Showing the Changes in Relative Concentration through the Thickness of the $UO_{2.06}$ Model. Each Slice is 1 μm Apart. . 147

6-18: The Cross Sectional Concentration Profiles Showing the Change in Relative Concentration through the Thickness of the $UO_{2.14}$ Model. Each Slice Is 1 μm Apart. . 148

6-19: A Highly Concentrated Grain and Its Neighboring Grain Structure in 3-D with High Diffusivity GB Labeled (a) in $UO_{2.06}$ Model (b) $UO_{2.14}$ Model. The Red Circles Indicate the Discontinuity in High Diffusivity GBs. 149

6-20: The Concentration Profiles under the Effect of (a) Correlated GBs (b) Random GBs with the Low Diffusivity GB Labeled. 151

6-21: The Effect of TJ Diffusion in the Heterogeneous GB Properties Model in the $UO_{2.14}$ Microstructure. 152

6-22: Concentration Profile of a Cut Plane 15 Micron Away from the Top Surface from a Mass Generation Simulation for the $UO_{2.14}$ Microstructure 153

Figure Page

6-23: (a) The Concentration Profile across the Black Line in Figure 6-22 (b) Experimentally Measured Xenon Concentration across a Grain at a Normalized Radial Position of 0.6 [107]. 154

6-24: A Section of the Temperature Profile in the $UO_{2.14}$ Model Showing the Temperature Drops under the Effect of the Kaptiza Resistance.................................... 155

6-25: The Temperature Profile (K) on the Right Surface of the Model under the Effect of GB Resistance.. 156

6-26: (a) The Concentration Profile of the $UO_{2.06}$ Model under Mid-Radius Conditions (b) A Horizontal Cross-Sectional Slice of the Concentration Profile............................ 160

6-27: (a) The Concentration Profile of the $UO_{2.14}$ Model under Center Pellet Conditions (b) A Horizontal Cross-Sectional Slice of the Concentration Profile............................ 160

6-28: (a) The Concentration Profile for the Multiphysics Simulation of the $UO_{2.00}$ Model under Edge Conditions (b) Vertical Slices of the Concentration Profile with the Outline of the Microstructure.. 162

6-29: The Cross-Sectional Concentration Profile for a $UO_{2.14}$ Multiphysics Simulation with a 10 nm GB Thickness.. 165

6-30: The Effective Diffusivity of the $UO_{2.00}$ Model with Respect to GB Thickness.... 166

6-31: The Effective Diffusivity of $UO_{2.14}$ Model with Respect to the GB Thickness.... 167

6-32: The Concentration Profile Plotted Based on the Four Cases Described in Table 6-5 for Sensitivity Analysis.. 168

LIST OF TABLES

Table Page

1-1: Genealogy of Large Nuclear Reactors [2] 8

1-2: Fraction of Elemental Fission Product Yield in a Fast Neutron Spectrum. Table Reproduced from [6] 18

2-1: Experimentally Determined Equations for Diffusivity of FG in UO_2. 32

4-1: Serial Sectioning Information for $UO_{2.00}$ $UO_{2.06}$ and $UO_{2.14}$ 67

4-2: Average Grain Size Obtained using Different Approaches for the Three Stoichiometric Samples 77

4-3: Homology Parameters for the Geometries in Figure 4-17 83

5-1: Microstructural Data in 3-D for the Three Reconstructed and Meshed Stoichiometric Samples 91

5-2: Stoichiometry Effect on Xenon Diffusivity. Table Reproduced from [25] 101

6-1: The Calculated D_{eff} from the Base Simulations 133

6-2: The Change in Effective Thermal Conductivity in the Three Different Microstructures. 157

6-3: Parameters for Multiphysics Simulations. 159

6-4: The Effective Diffusivities Calculated from the Multiphysics Simulations. 162

6-5: Applied Diffusivity Combinations for Sensitivity Analysis. 164

1. INTRODUCTION

The study of nuclear fuel is key to conceptualize and design new nuclear power plants capable of more efficient power generation. This chapter will provide a general background on the development and the current status of nuclear power industry. Some basic theories, issues and development of nuclear fuel elements are also covered to pave the ground for further discussion of the current research on oxide fuels, which will be the topic of the next chapter.

1.1 Nuclear Power Overview

With the fast increase in human population and modernized cities, the demand for power has increased dramatically over the past century. Globally, the major sources of power still rely heavily on fossil fuels, including coal, petroleum and natural gas. The issues with these traditional power generation methods mainly lie with air pollution and greenhouse gas release, both of which are believed to be the cause of global warming and climate change. New ways of power generation have been developed over the years aiming at resolving these issues. These include but are not limited to water, geothermal, wind, solar and nuclear energy. Among all types of energy mentioned above, nuclear technology gained an edge in the development and became mature enough for massive and steady power generation since the 1950s. Even today, nuclear power is still the only power generating method that can compete with fossil fuels in terms of cost and base load while emitting only water vapor and heat during operation. Many countries worldwide, including the United States, generate a significant portion of their power from nuclear reactors. The overview presented here looks into the history, development and challenges in the use of nuclear power.

1.1.1 History and Application

Nuclear power is generated from the atomic fission of fissile materials such as the isotopes of Uranium (U), Plutonium (Pu) and Thorium (Th). A great amount of energy, usually between one to two hundred MeV per fission event, is released during the process. Other than the energy produced, neutrons are generally produced as well. With sufficient kinetic energy, the neutrons can hit other atoms and initiate more fission events. A chain reaction can be sustained in such manner until running short of the fissile or fissionable materials. Over the years, people have learned to harvest this energy for different purposes.

Nuclear power was firstly applied in World War II as a weapon of mass destruction, soon after Enrico Fermi achieved the first self-sustaining chain reaction at the University of Chicago. It was later on applied as a mean of power generation that had the potential to replace or reduce the dependence on traditional fossil fuels. Experimental Breeder Reactor 1 (EBR1) harvested nuclear generated electricity for the first time in 1951 and marked a key milestone for nuclear power. Nuclear reactors were later on used to power ships, submarines and space shuttles. The advantages of nuclear power over fossil fuels include near zero carbon emissions and cheaper operation costs than all major source of fossil fuels, including coal, natural gas and petroleum. Over the years, nuclear energy has developed into a major power generation source in many countries including

France (75%), South Korea (30%) and the United States (20%). Figure 1-1 shows the increasing electricity generation from nuclear power plants over the years.

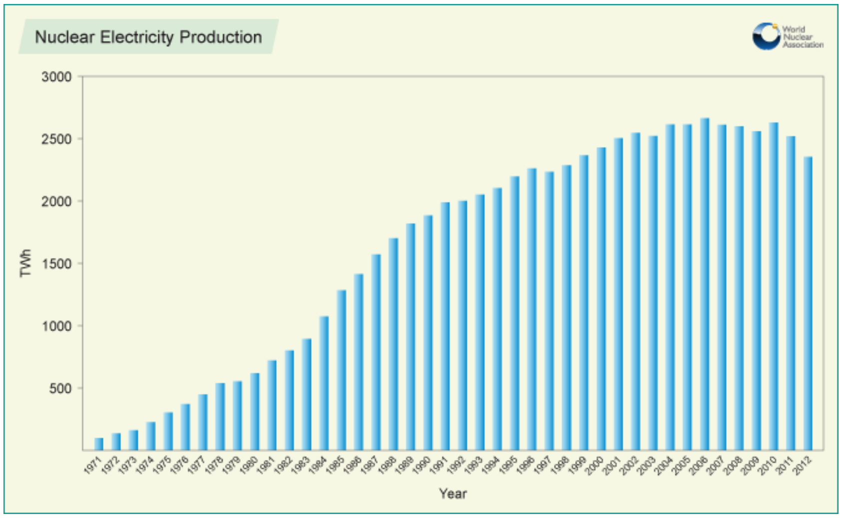

Figure 1-1: Nuclear Electricity Production over the Years [1]

The trend had slowed down recently after the outbreaks of several nuclear power plant failures over the years. It is worth noting here that coal powered electricity has made up for a majority of the increasing power demand worldwide, as other forms of renewable energy are not ready for power generation at a large scale. Overall, nuclear power generates 13% of the world electricity. It also accounts for 6% of total world energy use, the fourth largest after oil, coal and gas. In 2012, only eight countries were known to have nuclear weapon capability while thirty countries operated over 434 commercial nuclear power plants, which shows the increasing dependency on nuclear power [1]

About a decade ago, the increasing demand in energy consumption along with the rising cost of petroleum boosted multinational collaborations to develop the next generation of nuclear power plants. In the United States, there was a "renaissance" of nuclear power with new investment going into research and over 20 applications for construction and operation of new generation nuclear power plants [2]. However, a major part of the effort was stopped or indefinitely postponed after the disaster of the Fukushima nuclear power plant that took place in Japan in March 2011.

Today, very few nuclear power plants are being built in the U.S.; however, most of the plants are still filing for license renewal to extend their lives for another 20 to 30 years in order to meet current and future power demands. Research efforts have also continued and have shifted their focus toward operational safety as well as advanced fuels and structural material designs that will enhance the efficiency and safety of nuclear power plants.

1.1.2 Issues

Despite the great benefits of nuclear power, it also comes with some potential issues that can lead to serious consequences, and have thus led to many opposing viewpoints. The issues with nuclear power involve proliferation threats, nuclear waste storage and material failure. Each of these issues has played a role in deterring the development and growth of the use of nuclear power. These issues are briefly discussed in this section, including strategies under development to tackle them.

Proliferation is a term used to describe the spread of materials that can be used in nuclear weapons. In general, the concerns are placed on better regulations and controls to limit the access to the materials, such as ^{239}Pu and ^{235}U, which can be used to create nuclear weapons. From the nuclear power industry side, the spent fuel of a Light Water

Reactor (LWR) contains ^{239}Pu, which is a concern in terms of nuclear proliferation. It is desired to reduce the production of this isotope to the minimum. A new type of fuel that burns both UO_2 and PuO_2, termed mixed oxide fuel (MOX), was developed to serve this purpose. It consumes plutonium oxide, which can be reprocessed from the spent fuel, and thus reduces the proliferation threat and the amount of nuclear waste. Other methods include mixing gamma emitter nuclides into plutonium, burning plutonium in an inert matrix fuel form to trap plutonium, or by increasing the fraction of ^{240}Pu (12%) to deter proliferation activity [3, 4].

One major concern of nuclear power plants is the management of waste materials. The spent fuel assemblies, which contain fission products (FPs) and unburned fuels, remain toxic for thousands of years. Most commercial nuclear reactors today store spent fuel on site in a pool, which consumes power for cooling and is not ideal for safety purposes. The Yucca Mountain nuclear waste repository was proposed for the purpose of dry storing these spent fuels in a safer, remote environment. However, the site lost its funding in 2010 due to the opposition of environmentalists and political concerns. The construction and management of a long-term storage site for the toxic waste remains a big challenge. Other approaches to reduce the nuclear waste include fuel recycling and nuclear waste transmutation. The recycled fuels can be reprocessed to make MOX fuels as mentioned above. The transmutation of Pu and long lived FPs is another approach to reduce radiotoxicity of nuclear wastes to make them more manageable. Transmutation is usually achieved by converting the highly radioactive elements into others using the excess neutrons in the reactors [5]. The development of advanced fuel elements that can stand higher burnup will also help reducing the amount of waste produced.

Another challenge in running a nuclear power plant is the harsh environment in a reactor that can quickly degrade the materials for fuel elements, claddings and pressure vessels. The high temperature environment along with irradiation damage enhance creep rate, brittle failure, swelling of fuel elements, corrosion and fatigue [6]. These failure mechanisms limit the lifetime of the reactors. Research has focused on understanding and predicting these failures as well as developing new materials that can sustain these damage mechanisms for a longer period of time.

1.1.3 Current Status: new power plant (gen III and IV)

The first power generating reactor was the Experimental Breeder Reactor I (EBR-I), which successfully harvested atomic power for the first time on December 20th, 1951. Since then, many different reactors have been designed and built throughout the world. The more common types include the LWR, the Canada Deuterium (CANDU) reactor, the Liquid Metal Fast Breeder Reactor (LMFBR), the Advanced Gas Cooled Reactor (AGR) and the the High Temperature Gas-Cooled Reactor (HTGR). Among these designs, LWR is the most common type of reactor used for power plants in the U.S.

Light Water Reactors can be categorized into two types, Boiling Water Reactor (BWR) and Pressurized Water Reactors (PWR). Both reactors use water as coolant and steam to drive turbines. The main difference between the two designs is the pressure maintained in the reactor core. The BWR has a lower pressure and boils water directly in the core while the PWR functions at a higher pressure to keep the water in the liquid form before the water is passed to a secondary vessel for steam generation. One advantage of the PWR is that it allows more fuel rods in one fuel assembly and thus requires less number of assemblies [7].

Table 1-1 provides a list for the evolution of nuclear power plants over the years. The early fleets of LWRs in the U.S. were mostly built in the 60s and belong to a generation II design. They are all water cooled and use UO_2 as fuel. Generation II+ upgrades upon the existing LWRs so that they can burn on MOX fuels. These designs are mostly seen in Japan and France. New generation of LWRs, categorized as Generation III, are designed for safer and more effective operation. There are a few plants in construction in China, and two licenses have been approved in the U.S. for construction. The latest research focuses on Generation IV, which employs a completely different design. It is developed to operate at a higher temperature and uses different coolants as well as fuel elements, aiming to generate hydrogen as a byproduct of electricity and to contain all FPs within the newly developed tri-isotropic layered (TRISO) fuel particles. Research from all aspects of Generation IV is still ongoing.

Table 1-1: Genealogy of Large Nuclear Reactors [2]

Generation I	First nuclear electricity: EBR-I, Shippingport (US), Magnox (UK),.....1950s–1960
Generation II	Current fleet of LWRs – pressurized water (PWR) or boiling-water (BWR) (US); VVER (Russia); CANDU (a heavy-water cooled reactor) (Canada).........1970–1980
Generation II+	Current LWRs with new fuel; MOX, hydride fuel; liquid–metal bond
Generation III	LWRs of completely new design – passive safety, fewer valves, shorter piping: ABWR (GE-Toshiba), AP1000 (Westinghouse-AREVA); EPR (Europe) 1990 – present
Generation IV	Completely new designs or resuscitation of old reactor types – sodium fast reactor; (SFR); very-high-temperature reactor (VHTR)...2025 –??

1.2 Nuclear Physics Basics

In order to understand the operation of nuclear power plants, it is important to understand the basic concepts and terminologies of nuclear physics. This section briefly covers this aspect to introduce the basic equations and to define the terminologies that will aid the discussions in the later chapters.

1.2.1 Nuclear Physics Basics

Two of the most common nuclear reactions are fission and fusion (Figure 1-2), both of which are capable of generating a large amount of energy. The fission reaction consists on the separation of a nucleus into two fragments upon the absorption of a neutron that renders the nucleus unstable. It is most commonly observed in heavy elements such as uranium (U), plutonium (Pu) and thorium (Th). Take U-235 for example, under the fission reaction shown in Equation 1-1, it adsorbs a neutron and forms an excited U-236. The unstable U-236 eventually breaks into two FPs noted as FP1 and FP2 and emits neutrons and energy (E). The energy generated from the process can be obtained by calculating the difference in mass between both sides of the equation and apply the famous energy-mass equivalence equation: $E=mc^2$. The calculated fission energy for U-235 is approximately 200 MeV per fission event [4].

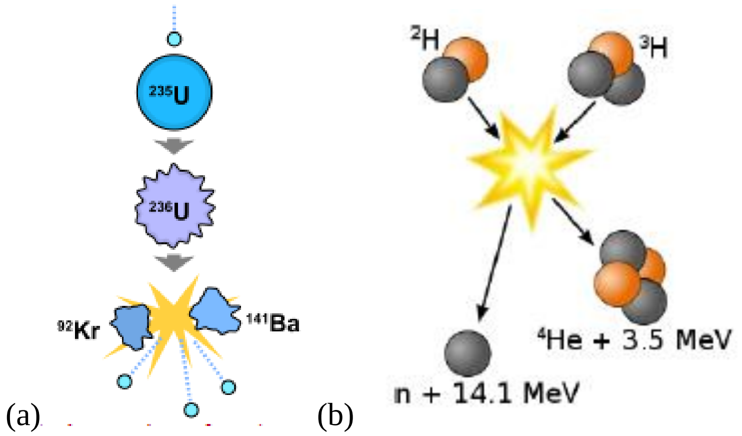

Figure 1-2: Illustrations of (a) Fission Reaction (b) Fusion Reaction

$$^{235}_{92}U+^{1}_{0}n \rightarrow ^{A_1}_{Z_1}FP1+^{A_2}_{Z_2}FP2+ x^{1}_{0}n+E \qquad \text{Equation 1-1}$$

The fusion reaction, on the other hand, occurs when two light elements, most commonly deuterium and tritium, combine into a larger element. Similar to the fission reaction, neutrons and energy can be released from the reaction as shown in Equation 1-2. The loss in total mass can also be calculated to find the energy released. The average energy yield for deuterium ($^{2}_{1}\mathrm{H}$) fuel is about 6MeV. One example of a fusion reactor is the Sun in our solar system. In terms of power generation, there exist many benefits to harvest fusion energy instead of fission energy, including higher energy per unit mass, more abundant fuel sources and less hazardous nuclear waste. However, the mechanisms and reactor designs for fusion reactors are a lot different from fission reactors, and challenges remain with the ability to sustain a chain fusion reaction. Breakthrough researches from many aspects are still needed to build a practical fusion power plant. The technology of fusion energy will not be addressed in this work.

$$^{2}_{1}\mathrm{H} + {}^{3}_{1}\mathrm{H} \rightarrow {}^{4}_{2}\mathrm{He} + {}^{1}_{0}\mathrm{n} + 17.6\mathrm{MeV} \qquad \text{Equation 1-2}$$

In fission nuclear fuels, the term “burnup” is used to measure the usage of a fuel element. Burnup is defined as the percentage of initial heavy metal that has undergone fission. The fractional burnup (β) can be calculated using Equation 1-3 below. Burnup can also be expressed as the number of megawatt days of thermal energy released by fuel containing 1 metric ton of heavy metal atoms (MWd/MTU). As a general rule of thumb, one percent burnup is approximately equal to 10^{4} MWd/MTU. These units are used interchangeably in different reports and papers.

$$\beta = \frac{\text{number of fissions}}{\text{initial number of heavy metal atoms}} \qquad \text{Equation 1-3}$$

1.2.2 Irradiation damage

After being able to sustain a nuclear reaction, the first challenge in reactor design is to take into account the radiation damage caused by the energetic particles generated from fission events. Materials need to remain functional under heavy radiation in order to be used in the reactors. To briefly describe the process of radiation damage, when an energetic particle, i.e., a neutron released from a fission event, hits a material, it has a finite probably to collide with a lattice atom. This probability differs between different atoms and isotopes and is described as the “neutron cross section”. The higher the neutron cross section is the higher the probability of having a collision event. The first atom that is struck by the particle is called “primary knock-on atom” or PKA. One way of describing the level of radiation damage in a material is by counting the number of displacements per atom, known as “dpa”. Upon collision, the PKA carries a “recoil energy” transferred from the particle and starts moving. The PKA would travel a distance in the lattice and forces a small displacement in other atoms until it reaches a stop in either a pre-existing vacancy site or a interstitial site. The path it traveled is called a “displacement cascade”. The results of many of these collisions are the formation of many point defects, or more likely, clusters of point defects such as dislocation loops and voids. These changes in microstructure often degrade material properties and cause many phenomena in fuel elements and structural materials that will be addressed later [8].

The irradiation damage is one of the most important factors to be considered when working with nuclear power generation, given that the damage caused by the highly energized particles produced during fission events is inevitable. Moreover, the atomic scale damage can quickly accumulate to impose a big impact on the microstructure and the material properties of fuel elements as well as structural materials.

1.3 Nuclear Fuels

Many different types of fuels materials exist for different types of reactors. They can be generally categorized into metallic fuels and ceramics fuels. This section will go over the basic mechanisms of nuclear physics in order to understand the desired properties in a fuel element. Different types of fuel will be mentioned, but the review will stress on oxide ceramic fuels as they are the most common type of fuel for nuclear power plants.

1.3.1 Nuclear Fuels Overview

There are fissile and fertile materials when it comes to nuclear fuels. The fissile material can have fission reaction by itself while the fertile material requires the capture of a neutron for the fission event to take place. The most commonly used element for nuclear fuel is uranium. In nature, there is over 99% of ^{238}U, which is fertile, and less than 1% of ^{235}U, which is fissile. A refining process is usually required to make fuels with more ^{235}U content, typically 3-5% for most reactors. Plutonium (Pu) is also commonly used in fuel elements by mixing it with uranium to make MOX fuels. The Pu can be extracted from pellets of spent uranium fuel. Using Pu serves the purpose of reducing the amount of nuclear waste as well as reducing the proliferation threats. In addition to uranium and plutonium, thorium (Th) is also a naturally occurring radioactive element that has a potential of generating nuclear power. Thorium is three times more abundant than uranium and has a different decay chain. It does not require enrichment, and it produces nuclear waste with less proliferation threat and a lot shorter half-life and thus has a potential to replace uranium as a cleaner fuel for nuclear power. However, thorium based fuels require a different reactor design, which is still being developed [9].

The radioactive elements can be processed to produce fuels of different types, including metallic fuels and ceramic fuels, in the form of nitride, carbide or oxide fuels. The most common type of fuel, as abovementioned, is uranium oxide, which is a ceramic type fuel. It is used in almost all LWRs in the U.S. It has the advantages of a very stable atomic structure and a higher melting temperature, which is better for power generation purposes. UO_2 has a fluorite crystal structure, as shown in Figure 1-3a, with the uranium atoms forming a face centered cubic (FCC) structure with oxygen atoms occupying the tetrahedral sites. It is usually made into cylindrical shape pellets with a diameter of about 1cm (Figure 1-3b). Other types of fuels, such as uranium nitride (UN) and uranium carbide (UC) are also commonly seen in reactors for different purposes, such as research and transportation. Different shapes also exist among these fuels, such as plate type fuel and spherical type, i.e., tri-structural isotropic fuel (TRISO) [10].

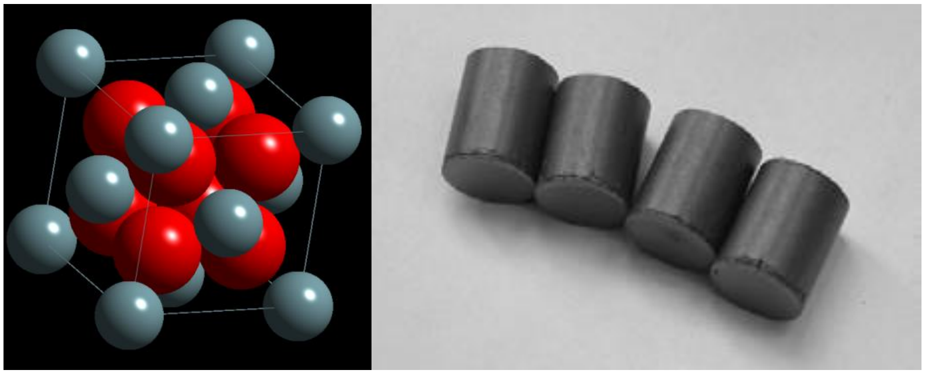

Figure 1-3: (a) Fluorite Crystal Structure (b) UO_2 Fuel Pellet with a Diameter of about 1cm [11]

TRISO fuel is one of the latest designs of nuclear fuels, which is meant to be used in generation IV VHTRs. The idea is to have a more enclosed design to contain the FPs. The smaller size also enhances heat transfer and allows the coolant to see higher temperature. The basic idea is shown in Figure 1-4. The fuel elements, usually UO_2 or UC_2, are made into spherical kernels and then covered with a carbon buffer, inner pyro-carbon, silicon carbide and then another layer of pyro-carbon. The final particles are dispersed in a graphite inclusion with a shape of a cylinder or a spherical pebble. Because of the introduction of carbon, the fuel chemistry becomes more involved. The layered structure also complicates the heat transfer model. Research work is focusing on both manufacturing process and the performance of the fuels as some prototype reactors are being built [10].

Figure 1-4: Tri-Structural Isotropic (TRISO) Fuel for VHTR

1.3.2 Uranium Oxide Fuel Performance

In LWRs, UO_2 is generally used in fuel pellets, which are stacked in a fuel rod as shown in Figure 1-5a. The material for the cladding is usually zircaloy, a zirconium based alloy, for better resistance to radiation damage. The fuel-cladding gap is kept to account for fuel swelling, and the space is filled with helium gas to enhance the thermal conductivity. Many fuel rods are assembled into a bundle secured by several square grids as shown in Figure 1-5b. The purpose of the grids is to provide support for fuel rods and prevent excessive vibration; however, they are also the spots in the fuel rods that are under higher risk of failure due to stress induced by small vibration and thermal expansion, a phenomenon known as fretting.

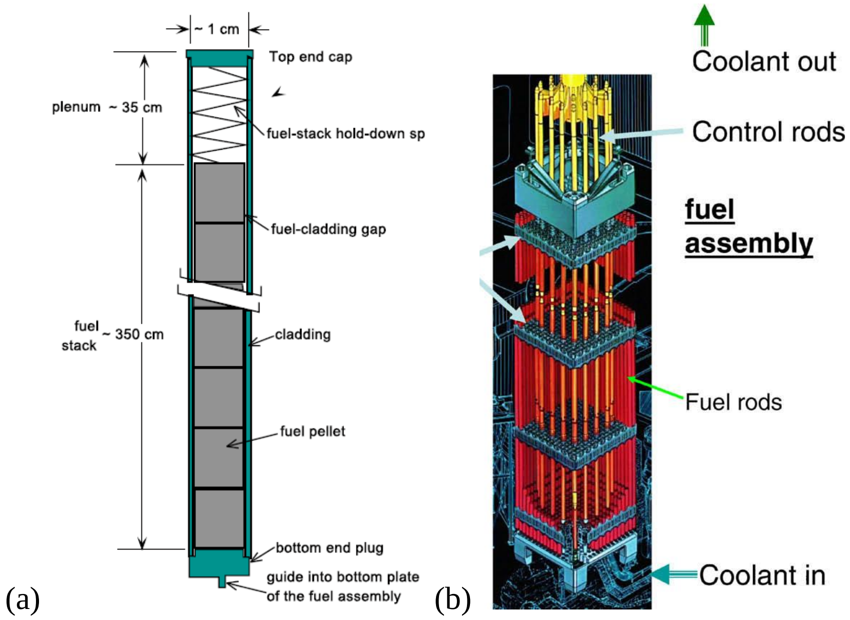

Figure 1-5: Fuel Assembly Illustration (a) the Layout of an Individual Fuel Rod (b) Pressurized Water Reactor Fuel Assembly [2]

One advantage of uranium dioxide, as mentioned above, is its stability at high temperature. Uranium dioxide has a melting point as high as 2800 °C. However, it has a lower heavy metal density, which means less burnable fuels. It is generally operating in a very high temperature environment while only cooled by the light water coolant. In addition to high temperature, the fuel elements in a reactor also experience a very high temperature gradient, which can be as high as 10^4 °C/cm [6], due to the low thermal conductivity, which is around 7.5 W/mK at room temperature. The thermal conductivity value is even lower at higher temperatures. Because of the high temperature and temperature gradient, many physical phenomena that are not usually observed at low temperature, including FP transport, pore migration and microstructure reconstruction, can take place and make a difference on material properties and fuel performance. To predict the changes in material properties has become a very important topic as it is the key to design fuels that allow higher burnup.

1.3.3 Fission Products

As the fuels are going through the fission process to produce heat for power generation, FPs are generated as a byproduct. The study of FPs is important for many reasons. First of all, some long lived FPs are highly radioactive and become a major concern for spent fuel treatment. Some nuclear research [5] focuses on the transmutation process to reduce the radioactivity and the half-life of these highly radiotoxic FPs. On the other hand, FPs can change the fuel chemistry significantly and thus the fuel properties. They also result in fission gas release (FGR), fuel swelling, and the resulting fuel-pellet interaction, which can cause the failure of fuel rods. It is thus important to have a thorough understanding of the formation of these FPs, their chemistry and the way they behave in the fuel elements.

Some FPs have a short half-life that is less than a day and are thus ignored for most studies. The majority of long-lived FPs are in either the solid or the gaseous phase, depending on the elements and the temperature. Regarding the solid isotopes, they can either form metallic inclusions, react with oxygen and form oxide compounds that reside in the fuel matrix or form its own oxide cluster for the ones with low solubility [6]. Fission gases (FGs) and volatile FPs, such as Xe, Kr, I, Cs, Rb, Te, Ba, Sr [12] account for a large fraction of fission yield (see Table 1-2) and thus can change the composition, microstructure and properties of the fuels significantly. They are also the cause of some common failure mechanisms, such as stress corrosion cracking (SCC) and fuel poisoning [10]. Furthermore, some FPs, such as ^{135}Xe and ^{149}Sm, have large thermal neutron absorption cross sections and are “poisonous” to fission reactions. These FPs absorb neutrons from the chain reaction and thus can significantly affect the chain reaction of the fuel element. Many considerations need to be taken for these FPs.

Table 1-2: Fraction of Elemental Fission Product Yield in a Fast Neutron Spectrum. Table Reproduced from [6]

Chemical Group	Elemental yield		
	^{235}U	^{239}Pu	0.15 ^{239}Pu + 0.85 ^{238}U
Zr + Nb	0.298	0.204	0.219
Y + rare earths	0.534	0.471	0.493
Ba + Sr	0.149	0.096	0.109
Mo	0.240	0.203	0.206
Ru + Tc+ Rh + Pd	0.263	0.516	0.456
Cs + Rb	0.226	0.189	0.209
I + Te	0.012	0.070	
Xe + Kr	0.251	0.248	

As outlined in the review above, FPs affect many aspects of the operation of a nuclear power plant. It is thus very important to understand their behaviors from the production to their kinetics and chemistry within fuel elements.

1.3.4 Fuel Swelling and Microstructure Reconstruction

As fuel burnup increases, the volume of the fuel elements must increase to incorporate the generation of FPs and voids formed by irradiation damage. The increase in volume along with FG bubble formation result in the phenomenon known as fuel swelling. Figure 1-6 provides a quick illustration of fuel swelling. It is shown that the expansion in volume can easily cover the gap between the fuel pellets and fuel rods and induce stress in the cladding. The interaction, known as pellet-cladding interaction (PCI) is one common cause of the failure in fuel rods. Eventually, the fuel pellets turn into an hourglass shape as a consequence of thermal and FP induced stress. Some species of FPs, in particular the nobles gases and volatile FPs, have very low solubility in the fuel matrix and thus exist in gaseous phase. The gas pressure builds up over time and causes cracks to form in the fuels. The transport of these FGs and the high temperature gradient in the fuel elements are responsible for the changes in microstructure within the fuel elements.

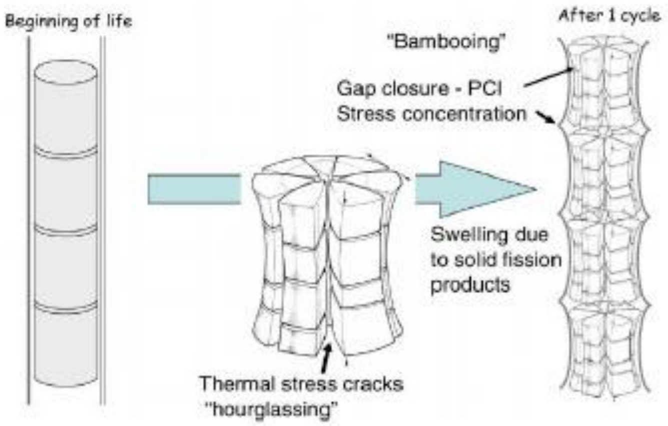

Figure 1-6: The evolution of fuel elements that lead to pellet- cladding interaction [2]

Under irradiation effects and high temperature, the fuel microstructure changes significantly. The changes can affect the fuel performance and sometimes cause failure. Material microstructure behaves differently at different radial positions as shown in Figure 1-7. In the center of the fuel pellet where the temperature is the highest, a void can form due to pore migration and the evaporation and condensation of UO_2. It is mainly observed in fast reactors, of which the fission chain is sustained by fast neutrons (higher kinetic energy) instead of thermal neutrons. The grains close to the center void evolve into a columnar shape along the radial direction as a consequence of rapid FP migration in the high temperature. The columnar grains are followed by equiaxed grains that are larger than those in the original polycrystalline microstructure due to grain growth. The perimeter of the pellets remains similar to the initial microstructure since the temperature is lower in that region [6]. It can take as little as 24 hours for the restructuring process to take place [10]. This change in structure makes a difference on fuel performance as well as FGR behaviors between low and high burnup.

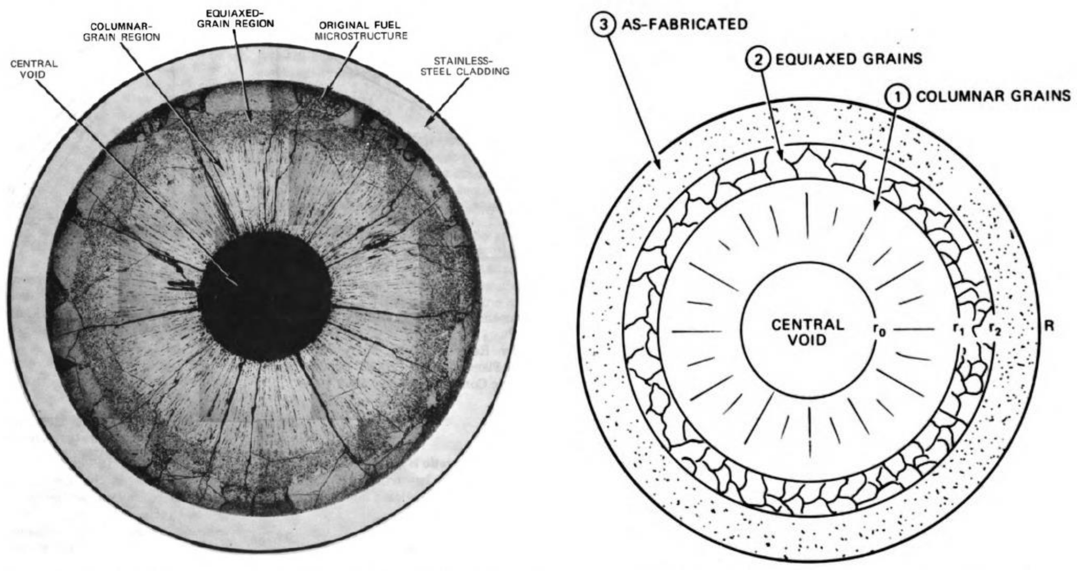

Figure 1-7: An Illustration of a Reconstructed Microstructure of a Fuel Rod Cross Section Irradiated in a Fast Reactor [6]

1.3.5 Release of Fission Gases

The management of FGR is an optimization problem. Fission gases tend to have very low solubility in the fuel matrix and form bubbles. The pressure of fission gases gets larger with the increase of burnup, and there are two possible outcomes for these gases. They are either retained inside the fuel pellet or released to the gap between pellet and cladding. If the gases are released to the gap, the pressure will increase and induce stress in the cladding, which can cause stress corrosion and other failure mechanisms fatal to fuel rods. They also have lower thermal conductivity than helium; therefore, they can reduce the rate of heat transfer and thus decrease the efficiency of power generation. The gases released from the pellets also have higher possibility of being released to the environment and cause radiation hazards [6]. On the other hand, if the gases are kept within the fuel pellets, they tend to form bubbles within the microstructure of the pellets. The bubbles usually form in the grains and then diffuse or segregate to grain boundaries (GBs) where they coalesce into larger bubbles as illustrated in Figure 1-8. The gas bubbles contribute to fuel swelling. If the gas bubbles link at GBs, they can also cause the intergranular cracking that is commonly observed at high burnup [6, 13]. The behavior and the release mechanisms of these FGs have thus become a critical factor for fuel performance.

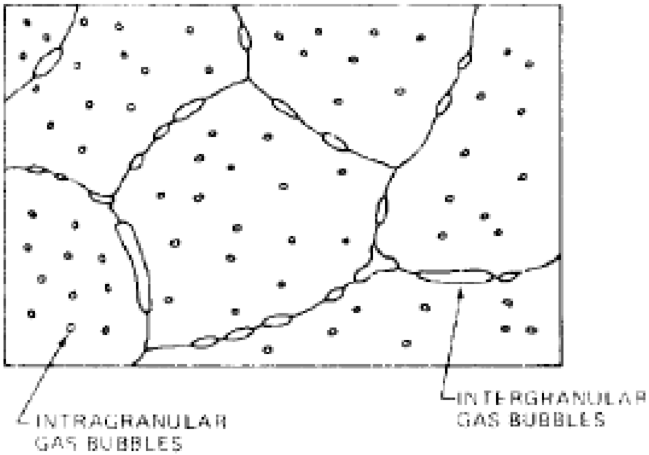

Figure 1-8: Fission Gas Bubbles Forming in the Grains and Coalesce in GBs [6]

The study of FGR was generally performed by measuring the quantity of released gas and fitting the results with a lattice diffusion model based on spherical grains. The model was later improved by including other mechanisms such as GB diffusion, bubble trapping and resolution [14-16]. Although the model has been successfully applied to predict the general trend of FGR, it does not predict the variation in the release profile caused by transient states and nor does it explain the observed local variation in bubble concentration [17, 18]. It has been seen from both experiments and reactor operation that the release of FGs is not linear. A phenomenon known as FG burst release has been observed from both operational and experimental data [19, 20]. Figure 1-9 shows an experimental data of the release of ^{88}Kr with respect to irradiation time. A rapid increase in the release to birth ratio is observed between week 15 to week 21. From the FG release experiments along with the sample characterization, it is believed that the burst of FG is a consequence of FG bubble inter-linkage. The FG atoms, as they are generated in the grain bulk tend to migrate to GBs or pores to form gas bubbles. When a GB is saturated with

FG, the GB opens up and forms an open path. If many open GBs are inter-connected to the pellet surface, a large amount of FG gets released in a short period of time. Figure 1-8 shows a diagram to illustrate the FG formation in the grain bulk and the coalescence in the GBs.

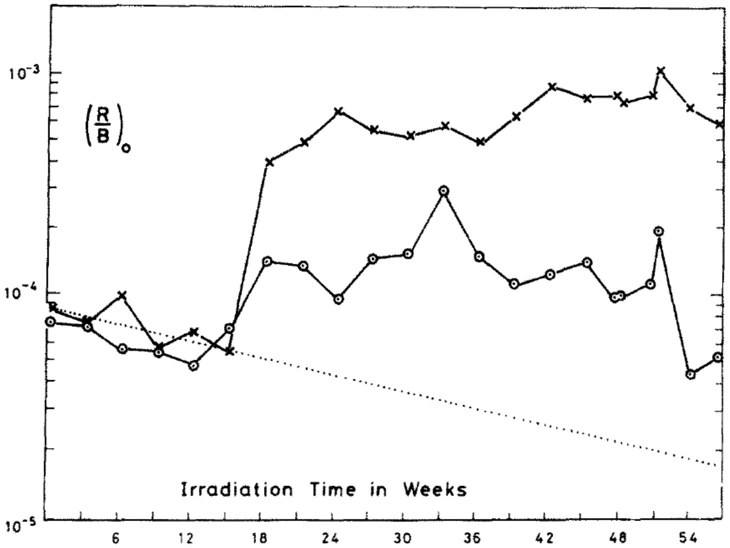

Figure 1-9: Fission Gas (^{88}Kr) Release to Birth Ratio (R/B) with Respect to Irradiation Time in Week in x: Small Grains and o: Large Grains [20]

Although the basic idea of FGR burst can be explained with the bubble linkage mechanism, the whole FGR process involves many different physical phenomena, including solid state diffusion, interface diffusion, percolation behavior, bubble-UO_2 equilibrium and irradiation induced diffusion. All these physics are happening in a high temperature and high thermal gradient environment. In addition, resolution of FGs can also happen due to irradiation effects. A thorough understanding in each of these physics and their coupling effects is needed in order to design advanced fuels with better performance. Many models and experiments have been conducted addressing these effects and will be introduced in more details in Chapter 2.

1.3.6 Experimental Techniques

The study of FGR involves both simulation and experiments. From the experimental perspective, there are two commonly used techniques to measure FGR: in-pile measurements and post irradiation heat treatment. The basic ideas of the two techniques are illustrated in Figure 1-10. Both techniques employ a sweeping gas system through the environment followed by a fission gas trapping analysis system. In general, in-pile experiments are more representative of the environment inside a reactor; however, the cost of building the experimental instruments around it is very high. The conditions, although more realistic, are more complex and harder for post analysis since there are more variables to be considered. For example, the rating for burnup and the temperature vary with time and the radial location. Post irradiation heat treatment, on the other hand, allows better control over the burnup and temperature and is thus more commonly used by researchers to study FGR and to calculate FG diffusivities [6, 10].

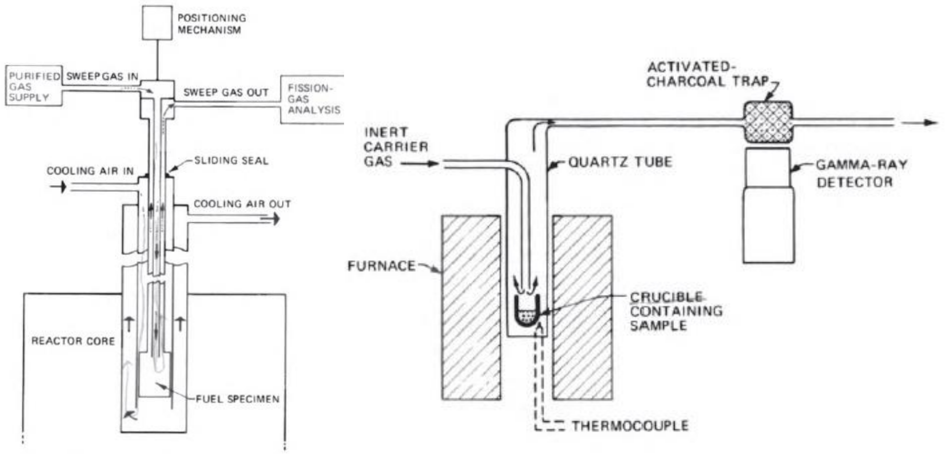

Figure 1-10: Diagrams to Illustrate (a) In-pile Experiment and (b) Post Irradiation Heat Treatment [6]

1.4 Motivation

The main purpose of the project funding this work is to develop advanced nuclear fuels for a more sustainable fuel cycle. Fuels of different types are being developed and studied to enhance accident tolerance and to achieve higher burnup. Research results are taken from several different aspects with a focus on simulation of fuel behavior due to the cost and difficulties involved with irradiation testing. For UO_2, even though the bulk behavior has been studied over many years, some phenomena such as FP transport and its effect on fuel properties are still not well understood. A more thorough understanding of the FP behavior is needed. It has been shown for many materials that the microstructural features play important roles in their transport behavior. However, not much modeling work in the microstructure level has been done for UO_2 in the past even though the importance of such work has been suggested from many characterization and theoretical works. Before the next generation fuel can be designed and manufactured, there is an urgent need to have a microstructurally explicit model that can reflect the micro-scale features of the material. Such model can be used to verify the performance of the developed fuels, which can help refining the manufacturing processes.

2. LITERATURE REVIEW

This chapter covers past research related to the transport of fission products (FPs) in UO_2, with a focus on the diffusion of xenon. The first part of the chapter goes over the material properties needed for this study. The second part of the chapter discusses the importance of the microstructure on material properties, and how it can affect the transport mechanisms. The last section of the chapter introduces some existing models to address the phenomenon of fission gas release (FGR).

2.1 UO_2 Properties

Uranium dioxide (UO_2), also known as uranium oxide or urania, is a black, radioactive crystalline material that occurs naturally in uraninite mineral, which is composed of 99.3% fertile U-238 and 0.7% of fissile U-235. It has a fluorite structure (CaF_2) with U^{4+} ions forming an FCC sub-lattice and with O^{2-} ions occupying the tetragonal sites. One of the major advantages of UO_2 as a nuclear fuel, as mentioned in Chapter 1, is the stability of its fluorite structure, which gives a high melting temperature of about 2865^{o}C. The oxygen ions in UO_2 do not fission and have no nuclear purpose.

A thorough understanding of the material properties is essential to the study of nuclear fuel, either for experimental or modeling work. Most intrinsic properties of UO_2 are well established through studies and measurements by many different scientists over the years [21, 22]. However, when applied in a nuclear reactor, UO_2 has properties that evolve with time. The changes in properties depend on many factors, including initial composition, oxygen content, thermal environment, irradiation history, microstructures, etc. Also, there are certain properties that are not as well established as the abovementioned such as grain boundary (GB) properties. This section covers a comprehensive literature review on the work done studying these properties with a focus on the effect of oxygen content, microstructure and burnup.

2.1.1 Thermal Properties

The thermal performance of fuel elements is critical to the operation of a nuclear power plant as it directly affects the efficiency of fuel elements. Many experimental data have been obtained over the years to study the thermophysical properties of UO_2. To study the thermal performance of the fuel elements, it is important to know the thermal conductivity, density and heat capacity. Fink [22] made a thorough review of the thermophysical properties of UO_2 in both solid and liquid form. The data, presented in Equation 2-1 through Equation 2-5 below, represent the initial properties of solid UO_2 fuel elements, where t=T/1000 and L_T is the material length at the temperature T, which is a way to present thermal expansion data. The equations were obtained by fitting the data obtained by many researchers as summarized in [22].

Thermal Conductivity:

$$k = \frac{100}{7.5408 + 17.692t + 3.6142t^2} + \frac{6400}{t^{5/2}} exp(\frac{-16.35}{t}) \qquad \text{Equation 2-1}$$

Density:

$$\rho(T) = \rho(273)\left(\frac{L_{273}}{L_T}\right) \text{ kg/m}^3 \qquad \text{Equation 2-2}$$

$$\mathrm{L_T} = \mathrm{L_{273}}(9.973 \times 10^{-1} + 9.082 \times 10^{-6}\mathrm{T} - 2.705 \times 10^{-10}\mathrm{T}^2 + 4.391 \times 10^{-13}\mathrm{T}^3 \text{ for } 273\mathrm{K} \leq \mathrm{T} \leq 923\mathrm{K} \qquad \text{Equation 2-3}$$

$$L_T = L_{273}(9.9672 \times 10^{-1} + 1.179 \times 10^{-5}T - 2.429 \times 10^{-9}T^2 + 1.219 \times 10^{-12}T^3 \text{ for} 923K \leq T \leq 3120K$$ Equation 2-4

L_T: the length at temperature (K)

$\rho(273)$: 10.963 Mg/m^3

Heat Capacity:

$$C_p=52.1743+87.951t-84.2411t^2+31.542t^3-2.6334t^4-0.71391t^{-2} \ \frac{J}{kgK}$$ Equation 2-5

The temperature dependence of thermal conductivity, for example, is illustrated in Figure 2-1. The thermal conductivity is about four times lower at 1800K as compared with the value at room temperature. This difference is significant and affects the fuel behavior as a large temperature gradient is usually present in the fuel pellets. Note that these functions are only temperature dependent and do not take into account the effects of irradiation and microstructure.

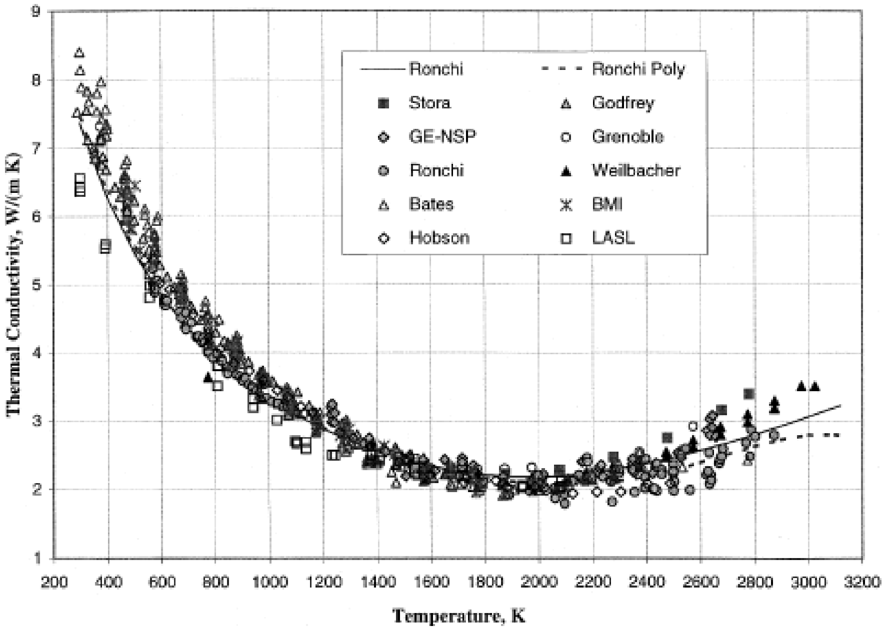

Figure 2-1: Experimental Data for Thermal Conductivity of UO_2 [22].

2.1.2 Fission Product Diffusivities

Transport properties of FPs, especially FGs, are not well established. For the course of this work, the diffusivity of xenon in UO_2 will be investigated due to its large quantity; however, it is important to keep in mind that other gases and volatile FPs, such as Kr, Cs, I and Rb can all behave similarly with some variations in each case. For the diffusivity of Xe in UO_2, D_{Xe}, there exists many experimental data measured by different techniques and in different environments [23-25]. However, the measured values spread over several orders of magnitudes. It is commonly believed that the spread is due to the defect density controlled by the fuel stoichiometry [23]. For ceramic nuclear fuels, the diffusion of FPs has three major mechanisms categorized by Turnbull [26-28]: intrinsic diffusion (D_1), irradiation enhanced uranium vacancy contribution (D_2) and irradiation enhanced self-diffusion (D_3) as shown in Equation 2-6, where T is fuel temperature and $\dot{F}$ is fission rate. The effective diffusivity is usually expressed as the sum of the three components. The detail of the explanation for each term can be found in [29].

$$D=D_1(T) + D_2(T,\dot{F}) + D_3(\dot{F}) \qquad \text{Equation 2-6}$$

The experimental intrinsic diffusivity data are usually measured by post-irradiation heat treatment, in which the fractional FG release data can be measured. The diffusivity of the fission gas can then be calculated based on Booth's model [30]. The measured diffusivity values are generally expressed in an Arrhenius equation in the form $D=D_0\exp(\frac{-Q}{RT})$, where D_0 is pre-exponential diffusion coefficient, Q is the activation energy and R is gas constant.

Table 2-1 shows a list of intrinsic xenon diffusivity values obtained from experiments, except for Equation 2-10, which includes the three diffusion mechanisms listed in Equation 2-6.

Table 2-1: Experimentally Determined Equations for Diffusivity of FG in UO_2.

Diffusivity Equation	Source	
$D_{Xe}=2.1\times10^{-4}\exp\left[\frac{\text{-380 kJ/mole}}{\text{RT}}\right]\text{cm}^2/s$	Cornel[31]	Equation 2-7
$D_{Xe}=7.6\times10^{-6}\exp\left[\frac{\text{-293kJ/mol}}{\text{RT}}\right]\text{cm}^2/\text{s}$	Davies and Long[32]	Equation 2-8
$D_{Xe}=1.1\times10^{-4}\exp\left[\frac{\text{-289kJ/mol}}{\text{RT}}\right]\text{cm}^2/\text{s}$	Matzke, Olander[33, 34]	Equation 2-9
$D_{FG}=1.09\times10^{-13}\exp(-6614/T)\ \text{cm}^2/\text{s}$ $for\ T > 1650K$ $D_{FG}=2.14\times10^{-9}\exp(-22884/T)\ \text{cm}^2/\text{s}$ $for\ 1381 < T < 1650K$ $D_{FG}=1.51\times10^{-13}\exp(--9508/T)\ \text{cm}^2/\text{s}$ $for\ T < 1381K$	Forsberg and Massih [28, 35] FG: Xe, Kr, I, Cs	Equation 2-10
$D_{Xe}=(0.05\ to\ 5)\times\exp(-3.9\text{eV/kT})\ \text{cm}^2/\text{s}$	Miekeley and Felix [25]	Equation 2-11
$D_{Xe} = 2.9\times10^{-8}\exp\left(\frac{-276.5\ \text{kJ/mol}}{\text{RT}}\right)\text{cm}^2/\text{s}$	Kaimal [36]	Equation 2-12
$D_{Xe} = 1.7\times10^{-8}\exp\left(\frac{-235\ \text{kJ/mol}}{\text{RT}}\right)\text{cm}^2/\text{s}$	Kashibe [37]	Equation 2-13

It is not difficult to see that a large discrepancy exists for both the pre-exponential term and the activation energy. There are many possible reasons for the spread in diffusivity measurements including sample conditions, experimental approach, environment and the irradiation profile [23]. The samples being investigated come from different manufacturers and have different density and microstructures, i.e., porosity and grain sizes. During the experiments, the researchers used different gases such as Ar, H_2, etc., and that can result in variations in sample stoichiometry, and it is believed that the deviation in stoichiometry has the biggest impact on the diffusivity measurements [23]. The irradiation history also plays an important role in the study because the defects generated can greatly impact the irradiation-enhanced diffusivity. Research work has also shown difference in Xe diffusivity at different concentration levels while the opposite effect was observed for Cs, I and Rb [33]. It is important to keep in mind the high level of discrepancy in FP diffusivity and each of these possible contributing factors when applying them in the study of FGR.

2.1.3 Stoichiometry Effect on Material Properties

Stoichiometry of UO_2 determines the defect structure and thus can affect the transport properties significantly. Fresh fuel pellets are usually made to be stoichiometric or close to stoichiometry with an oxygen to uranium metal ratio (O/M) of 2:1. As the burnup increases, uranium atoms are consumed by fission reactions, and the M/O is reduced. This issue, again, is not determined by a single factor; the distribution of oxygen in a fuel pin is also affected by the high temperature gradient and the formation of FPs that can form oxide compounds. Under the high temperature gradient, oxygen is transported by a CO/CO_2 mechanism in the opposite direction of the thermal gradient. It also forms oxide with many metallic FPs that are transported by vaporization and condensation mechanisms. In addition, the oxygen partial pressure in the gap needs to maintain equilibrium with both the fuel pins and the cladding materials such as zircaloys. As a consequence, the fuel stoichiometry would vary with burnup and radial position as shown in Figure 2-2.

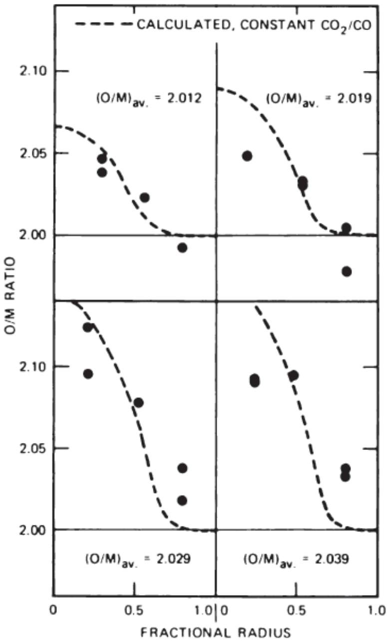

Figure 2-2: Oxygen Redistribution Results from Both Calculation and Experiments for $(U,Pu)O_{2+x}$ [6].

The difference in stoichiometry, as abovementioned, results in different material properties, especially the transport properties such as thermal conductivity and FP diffusivities. For thermal conductivity, it is known that the value decreases when the material stoichiometry deviates from 2.0 as shown in Figure 2-3. Physically, it is expected as the excess (or insufficient) oxygen produces point defects, which interfere with the phonon transport in the lattice structure. The change in thermal conductivity is most significant at low temperatures. The stoichiometry effect on thermal conductivity becomes less pronounced with increasing temperature and O/M ratio.

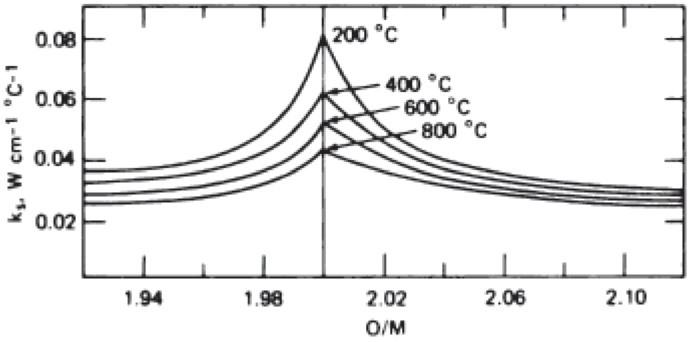

Figure 2-3: The Change in Thermal Conductivity with O/M Ratio and Temperature for $U_{0.8}Pu_{0.2}O_{2\pm x}$ [6].

As mentioned in section 0, the measured FG diffusivity value varies by several orders of magnitude, and it was proposed that the main factor contributing to this scatter was the stoichiometry of the samples. To address this problem, Miekeley and Felix [25] investigated the stoichiometry effect with post irradiation annealing experiments on three samples of different stoichiometry: hypo-stoichiometric (UO_{2-x}), hyper-stoichiometric (UO_{2+x}) and stoichiometric (UO_2). It was found that the hyper-stoichiometric sample has the highest diffusivity followed by stoichiometric sample at 1400 K as shown in Figure 2-4. It was also reported that no difference in diffusivity values was observed based on many experimental data. However, a different observation was published by Matzke [38] that showed a variation in D_{Xe} with the magnitude of x as shown in Figure 2-5. Theoretically, it makes more sense to see changes in diffusivity with respect to the x

value due to the changes in defect structure [39]. Overall, these experimental works provided insights to the defect structures of UO_{2+x}, which is important to many atomistic diffusion models that will be discussed later.

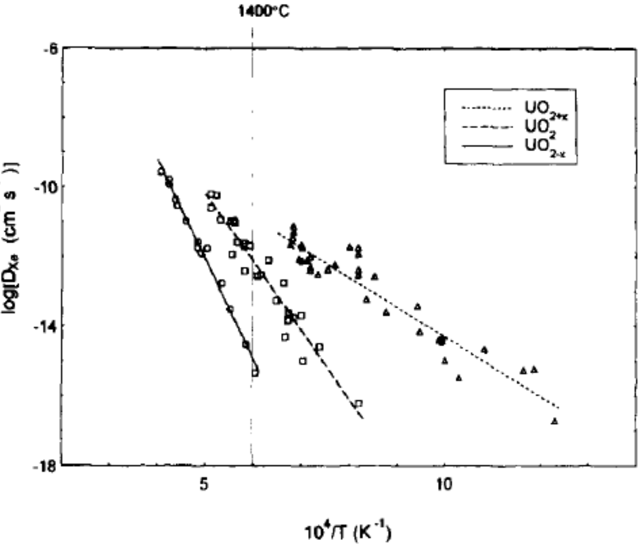

Figure 2-4: Variation of D_{Xe} with Stoichiometry in UO_2 Powders [25].

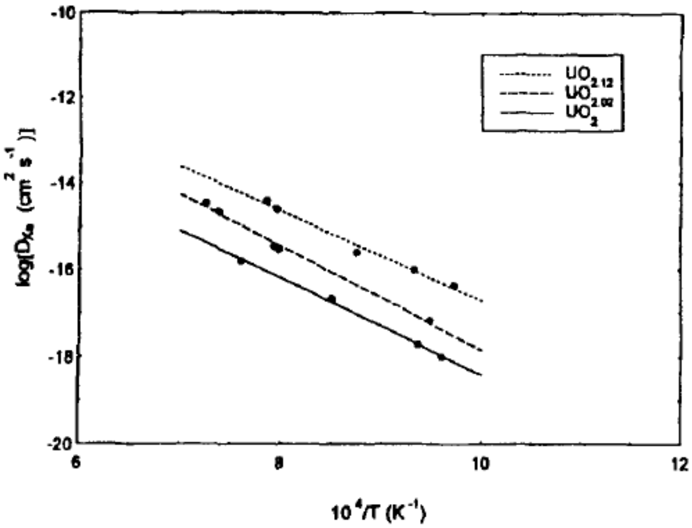

Figure 2-5: Variation of D_{Xe} with Sample Stoichiometry in UO_2 Powder [38].

2.2 Effects of Microstructure

It is known that the microstructure plays an important role in material properties. For polycrystalline materials, both metals and ceramics, microstructural features include porosity, grain bulks, GB and triple junction (TJ). Any variation in properties from these microstructural features can result in a large variation in bulk behaviors. This section will discuss the important aspects of microstructural effects on the transport of FPs in UO_2.

2.2.1 Grain Boundary and Coincident Site Lattice

Grain boundaries (GBs) play an important role in polycrystalline materials. The material properties at GBs are different from the bulk lattice because of disordered structure and higher interfacial energy at GBs. They are usually the preferred sites for corrosion, cracking as well as mass diffusion [40]. It has been found that GBs are the high diffusivity paths in some materials, both metals and ceramics [41]. For UO_2, it is generally believed that GBs play an important role in the release of FGs [34]. As the grain size gets smaller, the coverage of GBs per unit volume increases, and the effect of GBs on material properties can increase significantly. Much work has been done trying to understand GBs for metals. However, the work is still lacking for ceramic materials, in general, and UO_2, in particular. Before getting into the detail of the present work, it is necessary to understand some basic concepts of GBs and how it can affect the FP transport.

Grain boundaries have imperfect crystal structure in the presence between two grains of different orientations. The difference in angles between two neighboring grains orientation axes is called the disorientation or misorientation angle. Based on the rotation axis between two grains, as defined by their Euler angle [40], GBs can be categorized as tilt GBs and twist GBs. A tilt boundary has a rotation axis that is parallel to the boundary plane while the twist boundary has the axis perpendicular to the boundary plane. Grain boundaries can also be classified as low and high angle GBs according to the angles of misorientation, and it has been found that low and high angle GBs can have different properties as shown in Figure 2-6. Usually when the angle exceeds 10° to 15°, it is categorized as high angle GBs. In a low angle GB, atoms are better aligned with each other while in high angle GBs, they tend to be more distorted and thus have higher GB energy [42].

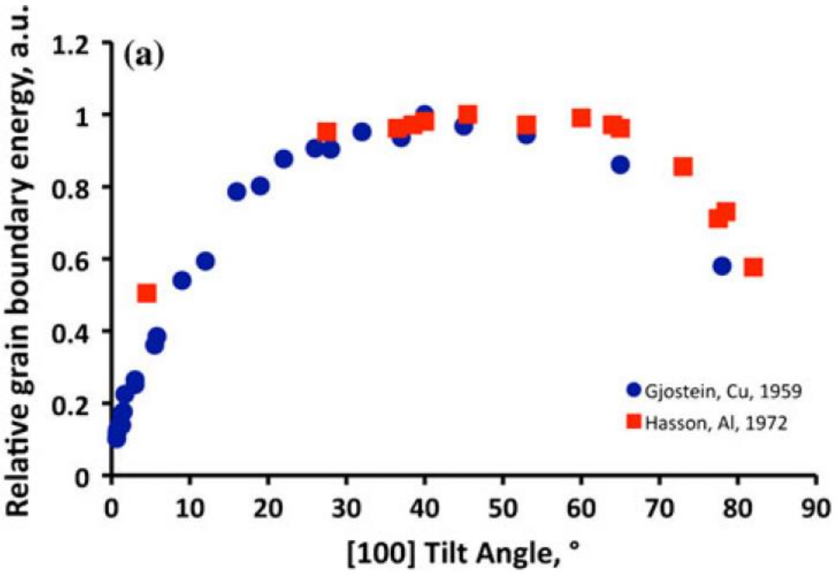

Figure 2-6: Relative GB Energy Data for Al and Cu for a Symmetric [100] Tilt Boundary That Shows the Increase in Energy with Misorientation Angle [43].

It was also discovered that certain high angle GBs with certain specific planes and misorientation angles have lattice sites that coincide between two grains, and these "special GBs" are expected to have a more aligned structure than a general GB. According to coincident site lattice (CSL) theory, these GBs can be categorized by their degree of fit (Σ), which is defined as the reciprocal of the ratio of coincidence sites to total number of sites at boundaries [40]. Figure 2-7 shows an example of the structure of a Σ5 tilt (310)/ [001] GB [44]. The effect of CSL on GB energy has been experimentally proven for many materials (Figure 2-8). These differences in GB energy often lead to variation in their behaviors such as resistance to corrosion and GB diffusivities.

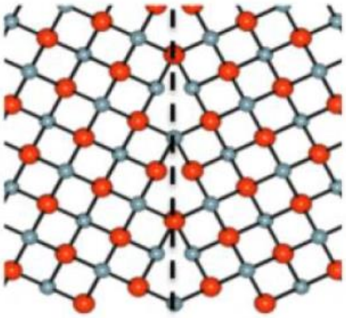

Figure 2-7: Structure of Σ5 Tilt Boundary at (310) Plane in [001] Direction [44].

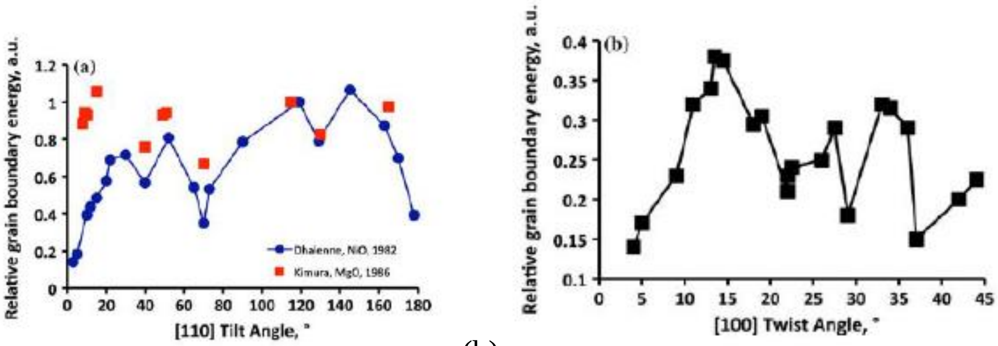

(a) (b)

Figure 2-8: The GB Energy at Different Misorientation Angles for a Ceramic (a) [110] Tilt (b) [100] Twist [43].

Possible evidence of the effect of heterogeneous GB properties have on the FG bubble distribution in UO_2 fuels has been observed. Figure 2-9 shows a fractograph of UO_2 grains with bubbles on their GBs. The bubble shape and connectivity vary between different GBs with some isolated and some connected. The bubbles in the connected GBs appear to have grown and coalesced sooner than bubbles in other GBs. It seems like the crystallography effect is a more reasonable explanation as these neighboring GBs are all under similar environment and irradiation history. However, no study, to the best of author's knowledge, has been conducted regarding this phenomenon.

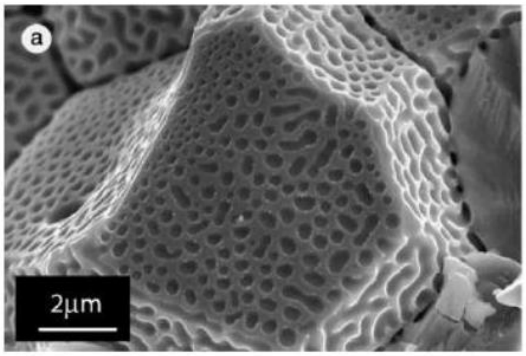

Figure 2-9: A Micrograph of a UO_2 Grain Showing Different Pore Shapes at Different GBs [45].

2.2.2 Grain Boundary Diffusion

The phenomenon of GB diffusion was established as early as 1950s when Fisher [46] set up the problem by placing a thin layer of high diffusivity material between two grains with low diffusivity while a constant flux was applied from the top surface as shown in Figure 2-10. By solving a mass balance equation using Fick's law of diffusion, the GB concentration can be expressed with a partial differential equation as shown in

Equation 2-14, and similarly for bulk concentration, which is shown in Equation 2-15, where the C_b is the concentration at the GB, D_b is the diffusivity of the GB, D_l is the lattice diffusivity, C_l is the concentration of the bulk lattice and δ is the GB thickness. Whipple [47] was the first one to solve for the exact solution to this problem as shown in Equation 2-16. It was shown that the GB diffusivity D_b is in a product with δ, which means that one can only determine the value of δD_b but not D_b alone. It puts an emphasis on the fact that the GB thickness plays an important role in the study of GB diffusion. However, the value for δ is not well defined and can depend of the type of GB, the porosity and many other factors. Values ranging from 0.5 nm to 100 nm have been used in different models [48, 49].

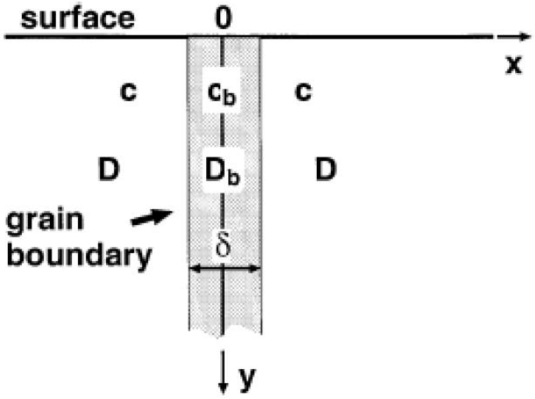

Figure 2-10: A Sketch that Illustrates the GB Diffusion Model Described by Fisher [50].

$$\frac{\partial C_b}{\partial t} = D_b \frac{\partial C_b}{\partial y} + \frac{2D_l}{\delta} \frac{\partial C_l}{\partial x}$$ Equation 2-14

$$\frac{\partial C}{\partial t} = D\nabla^2 C$$ Equation 2-15

$$\left[\mathrm{dln}(\overline{c})/\mathrm{d}(y^{6/5})\right]^{5/3} = 0.66(D_l/t)^{0.5}(1/\delta D_b)$$ Equation 2-16

For polycrystalline materials, the GB diffusion mechanism was classified into three types by Harrison [50]. Figure 2-11 shows a schematic of the three GB diffusion types. Type A describes a case with long diffusion time, small grain size and a high bulk diffusivity that is comparable to GB diffusivity. Under these conditions, no significant difference in concentration can be observed. Type B is the most common type of diffusion mechanism that is observed from experiments [51]. It has a deep penetration depth along GBs with a simultaneous diffusion from the GB to the bulk. If the bulk diffusivity is negligibly small, the diffusion mechanism is a type C, which has no observable concentration gradient in the bulk.

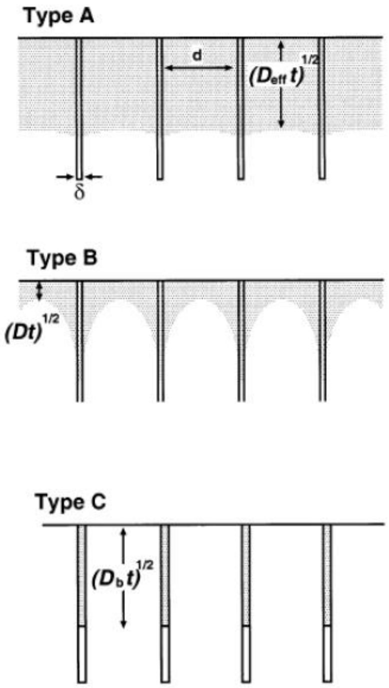

Figure 2-11: Schematic Illustrations of Type A, B and C Boundary Diffusion in a Polycrystalline Material [50].

Experiments, as well as simulations, have been done on ceramic materials with the fluorite structure, such as yttria–stabilized zirconia (YSZ) [52] and UO_2 [49], and illustrate the effects of GBs on mass transports. It was found that for both metal and oxide ceramics, the D_b/D_l could be as high as 10^7 [49]. Grain boundary diffusion has been known to be the reason for many observed phenomena such as grain growth, recrystallization and Coble creep. It also plays an important role in the models for FGR, which will be discussed in more details later.

For nuclear fuels, uranium oxide to be specific, it is generally believed that the release of fission gases occurs mainly by the interconnections of gas bubbles at GBs. Grain boundary diffusion was simply ignored in most studies. However, an analysis done by Olander [34] found that the simple grain bulk diffusion model does not fit the fractional release data he obtained at low burnup. The analysis showed that FGR through interconnected bubbles is only the case at medium and high burnup (> 20MWd/kg) when the gas atoms are trapped after migrating a distance equal or less to the size of a grain. At low burnup, GB diffusivity is still contributing to the release of fission gases with little or no effects from trapping by the bubbles.

2.2.3 Percolation Theory and Grain Boundary Networks

Because of the high diffusivities and the heterogeneity that GBs possess, percolation theory has been applied to study how they affect transport in a GB network. Percolation theory is a study of the connectivity in a network. It describes the geometrical transition between disconnected and connected phases with respect to the increase of concentration of occupied sites [53, 54]. It deals with the number and properties of clusters, which is defined as a group of neighboring occupied sites. The percolation threshold (p_c) is the concentration at which the cluster starts to expand from one side of the system to the other. The value is dependent on the lattice geometry as well as the size of the network and can be solved mathematically. For an infinite network, the 2-D honeycomb lattice has a percolation threshold of 0.65271. The values for 3-D networks are generally smaller due to the larger number of neighboring sites, and the p_c for a simple cubic network has a value of 0.2488 [53]. Percolation theory has been applied in the study of many physical properties of disordered systems such as mechanical properties of gels and conductivity of metal insulator composites. It has also been applied to study the diffusion mechanism in a GB network.

The effect of heterogeneous GB diffusivity on mass transport in a GB network and the conditions that lead to percolation are studied by Chen et al. [55] using a computational model. The model is set up as an ideal, 2-D honeycomb lattice network with two diffusivity values randomly assigned to each GB. The high diffusivity (D_2) and low diffusivity (D_1) were assigned to GBs at random with a prescribed probability. The probability, which controled the fraction of high diffusivity GBs (p), was varied arbitrarily in this simulated network. The effective diffusivity was calculated using Effective Mean Theory [55]. In Figure 2-12a and b, the normalized concentration profile with p=0.7 is plotted at two different diffusivity contrasts, and the difference is obvious with the diffusivity ratio set at 10 and 10^8. The concentration distribution became nonlinear in Figure 2-12b, which has the high diffusivity contrast. The distribution of the concentration shows how the low diffusivity GBs can hinder the mass flow on certain sites while increasing the mass flow on others. The normalized effective diffusivity with respect to p at different D_2/D_1 ratio is plotted in Figure 2-13. Two major findings from the result include the critical high diffusivity GB fraction p_c and the continuity of the curves for different D_2/D_1 ratio. At a fraction of about 0.65, there is an abrupt change in normalized D_{eff}, indicating the onset of percolation, which matches closely to the theoretical value for a honeycomb lattice [53]. At this critical value, the curves have a sharp increase in magnitude; moreover the increase in magnitude become discontinuous for high diffusivity contrast cases ($D_2/D_1 > 10^4$). These observations indicate that percolation behavior can only be observed for GB networks with high diffusivity contrast, and the critical value of percolation threshold obtained in this simulation was about 0.65.

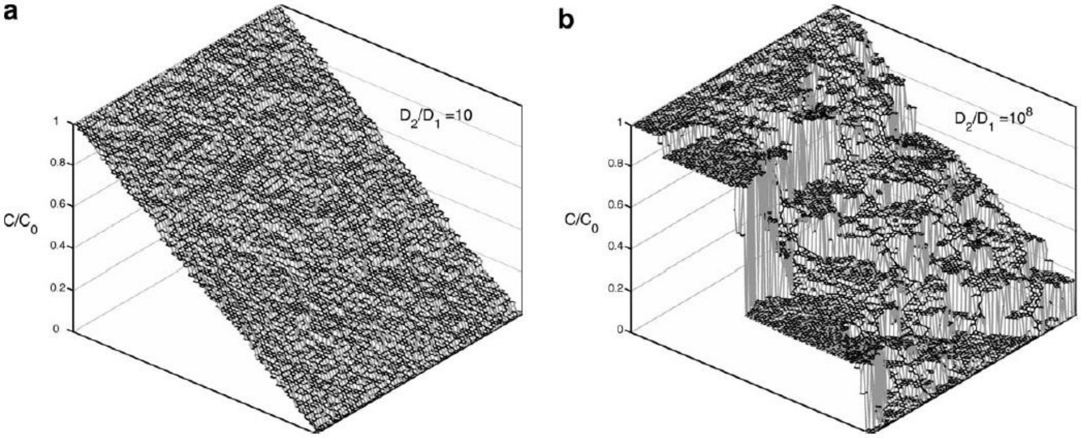

Figure 2-12: The Concentration Profile with (a) Low Diffusivity Contrast GBs (b) High Diffusivity Contrast GBs under a Fixed Concentration Gradient.

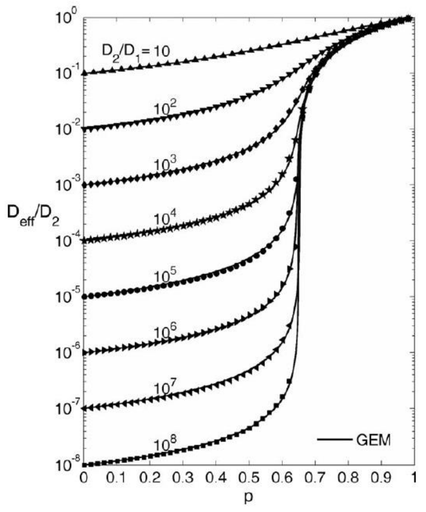

Figure 2-13: Normalized Effective Diffusivity Change with High Diffusivity GB Fraction (p) for Different Diffusivity Contrast.

Another important aspect of applying percolation theory in engineering studies is related to scaling laws. In principle, percolation theory tries to describe a system in an infinite network to understand the general behavior. However, an infinite network does not exist in reality and the percolation behavior can vary with the size of the network. Scaling laws have been developed to address this issue. Work done by Frary and Schuh [56] examined the scaling effect in a GB network using four properties: average radius of gyration of GB clusters (R_s), the number of clusters of a given mass per lattice site (n_s), the connectivity length (n), and the strength of the infinite or lattice spanning cluster (P). The GB networks for special GBs as well as general GBs with and without crystallographic relationships were studied. It was found that all the finite size GB networks studied follow the scaling law. Deviations, caused by local correlation, became significant when the cluster size decreased to three grain diameters or smaller.

2.2.4 Grain Boundary Thermal Resistance

Microstructure can also make an impact on the thermal performance of fuel elements, and it is very important to have a thorough understanding of their thermal performance as it directly affects the efficiency of the power plants. Many simulation works at different scales [57] have been conducted in the past trying to predict the thermal conductivity of UO_2 inside a reactor. It is an evolving property that depends not only on temperature but also on the evolution of the microstructure, which makes it a complex process. Lucuta et al. [58] summarized and expressed thermal conductivity as:

$$\lambda=\kappa_1(\beta)\kappa_2(p)\kappa_3(x)\kappa_4(r)\lambda(T) \text{ (W/mK)} \qquad \text{Equation 2-17}$$

where κ_1 is the burnup (β) dependence factor, κ_2 is the porosity/bubble contribution (p), κ_3 is the effect of O/M ratio and κ_4 is the radiation damage (r) factor. Each of these factors plays a different role at different stages of the fuel cycle, and interacting effects may exist between these factors to further complicate the problem. Typically, these factors are studied individually to provide inputs to fuel performance. In a microstructurally explicit model, the effects of GBs can be taken into account in the study thermal conductivity.

Grain boundaries have a disordered atomic structure and can impede phonon scattering, which is the mechanism for heat conduction, and thus reduce the overall thermal conductivity. The phenomenon is known as GB thermal resistance, or Kapitza resistance as it was firstly observed in the 1940s by Kapitza [59] to describe the resistance to heat flow at material interfaces. Polycrystalline materials have many GBs that act as thermally resistive layers and can significantly reduce the overall thermal conduction of the materials [6]. When FGs accumulate in the GBs, the low conductivity inert gas bubbles can further increase the thermal resistance in these boundaries [55, 60, 61]. The effect of the GB Kapitza resistance has been studied for silicon and oxide ceramics, including YSZ and UO_2 [62-64]. The analytical solution derived by Yang [62], as shown in Equation 2-18, is generally used to solve for Kapitza resistance.

$$k = \frac{k_0}{1+\frac{k_0 R_k}{d}} \qquad \text{Equation 2-18}$$

where k is the effective thermal conductivity, k_0 is the bulk thermal conductivity, R_k is the Kapitza resistance and d is the grain size. Phase field models created by Chockalingam, Millet and Tonks modified Equation 2-18 and showed the changes in effective thermal conductivity of UO_2 as a function of pore sizes and GB bubble coverage [48, 65]. The models take into account the bubble shape factors, bubble coverage fraction and grain size in a 2-D hexagonal grain structure and derived effective Kapitza resistance for GBs with FG bubbles.

2.2.5 Effect of Triple Junctions

A TJ, a line in 3-D where three GBs meet, is also an important microstructural feature that needs to be considered when studying microstructural effects on fuel elements. Similar to GBs, TJs can also be fast diffusion paths due to their structure. The diffusion mechanisms for TJs, however, are not as well established as GB diffusion. Some studies do exist as Chen et al. [66] has pointed out that TJ diffusion can be a possible mechanism for the “anomalous diffusion” that was observed in nano-crystalline materials. Experimental work presented in [67] has also shown that diffusion of zinc along aluminum TJs is about three orders of magnitude higher than GBs. If that is also the case for UO_2 as nuclear fuel, it can have a significant impact on the studies of fission gas release at low burnups. Figure 2-14 shows a SEM picture of bubbles located in GBs as well as TJs. It can clearly be seen that TJs have larger bubbles compared with its neighboring GBs, which is evidence that TJs have different properties from GBs and grain bulks in the study of FGR. Moreover, if TJs are the first microstructural feature to be filled with FG bubbles, their connectivity can be a more important network that dominates the FG venting. However, research work in TJs in general and its application to FGR is still lacking.

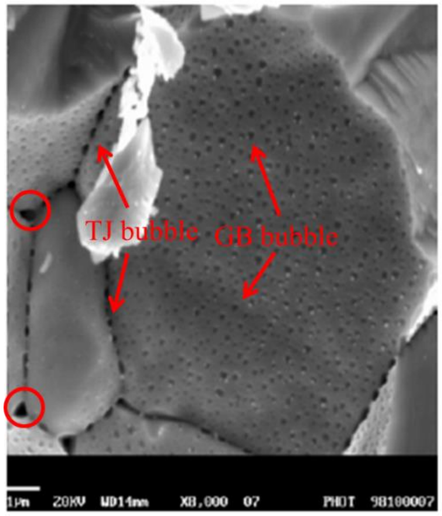

Figure 2-14: Early Stage of Porosity Formed by Fission Gas Formation at a UO_2 Fracture Surface Taken by SEM. The Size Difference Between Pores at TJs and GBs Can Be Differentiated. The Circled Areas Are Quadruple Points Where Three TJs Meet. [45].

From the crystallographic point of view, TJs are also important as the dihedral angles, which can be measured at TJs (Figure 2-15), reveal GB tensions and, in turn, GB energy [42]. The information helps predict the movement of grains and GBs as they try to achieve equilibrium when all three dihedral angles are equal to 120°. Other than dihedral angles, Schuh [68, 69] also showed that there existed a correlation at TJs where the type of GB was determined by the other two GBs due to crystallographic constraints (Figure 2-15b). The work in [68] also concluded that it required 50-70% more special GBs to break the connectivity of high angle GBs. This illustrated that a randomly generated GB network did not fully characterize an actual GB network. Figure 2-16 shows an example by comparing a general GB network created at random (a) and a network created following crystallographic constraints (b). It is evident that Figure 2-16b has a more connected GB network as compared with Equation 2-16a.

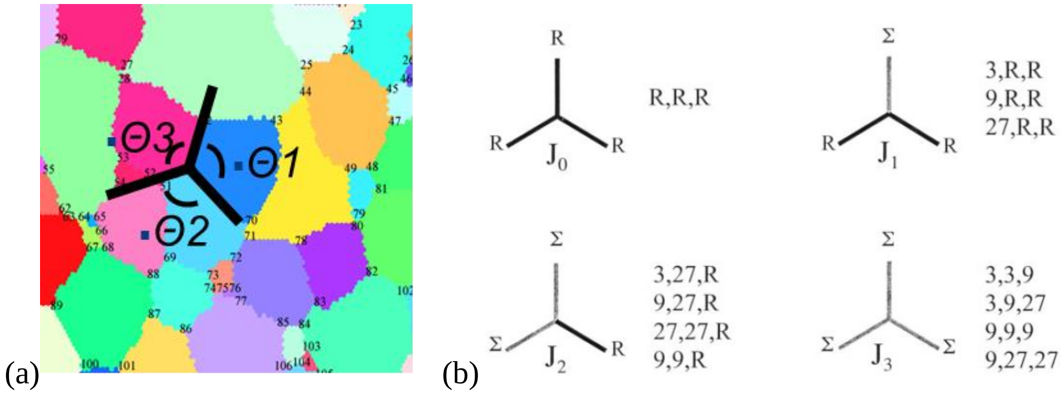

Figure 2-15: (a) Three GBs Intersecting at a Triple Junction Reveals Three Dihedral Angles (b) The Possible Combinations of GBs That Satisfy Crystallographic Constraints at a TJ Defined in [68].

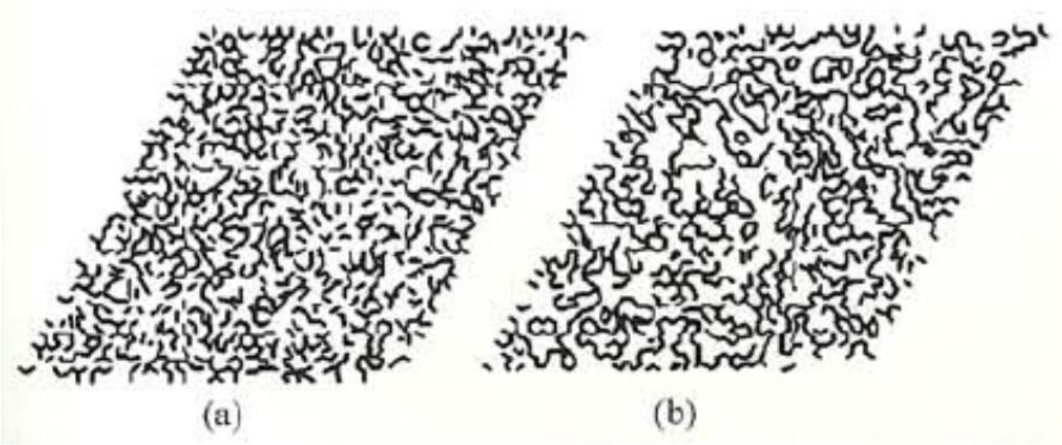

Figure 2-16: General GB Network in Irregular Lattice (a) A Randomly Generated GB Network (b) a GB Network with Crystallographic Constraints [70].

Despite the fact that TJ diffusion is not as well established as GB diffusion, it is still an important factor that affects the crystallography of the microstructure as well as the distribution of general and special GBs. The atomic structure is definitely more complicated to study than that of GBs; however, if TJs possess a diffusivity value that is orders of magnitude higher than D_{GB}, the outcome of FGR can be altered by them. It is important to keep in mind the possible effect of TJs when studying the microstructure effect on FP transport.

2.2.6 Defect Structure in Uranium Dioxide

The bulk transport of FPs in UO_2 is strongly dependent on the defect structures, which is also a strong function of the stoichiometry and atomic structure. Uranium dioxide has a fluorite structure, and as a fuel material, it is generally made to be close to stoichiometry. However, as burnup increases, uranium atoms are consumed and the pellets tend to become hyper-stoichiometric UO_{2+x}. The number of point defects increases significantly with the increase in *x*, followed by formation of voids and defect clusters. These defects strongly affect the transport properties of the fuel element [6]. It is important to have a good understanding of the defect structure in UO_2. Figure 2-17 shows the dependence of oxygen partial free energy on the deviation from stoichiometry. The *n* value corresponds to the relationship to oxygen partial pressure ($pO_2^{1/n}$), which determines the stoichiometry. The dominating defect structure varies with the *n* value [71].

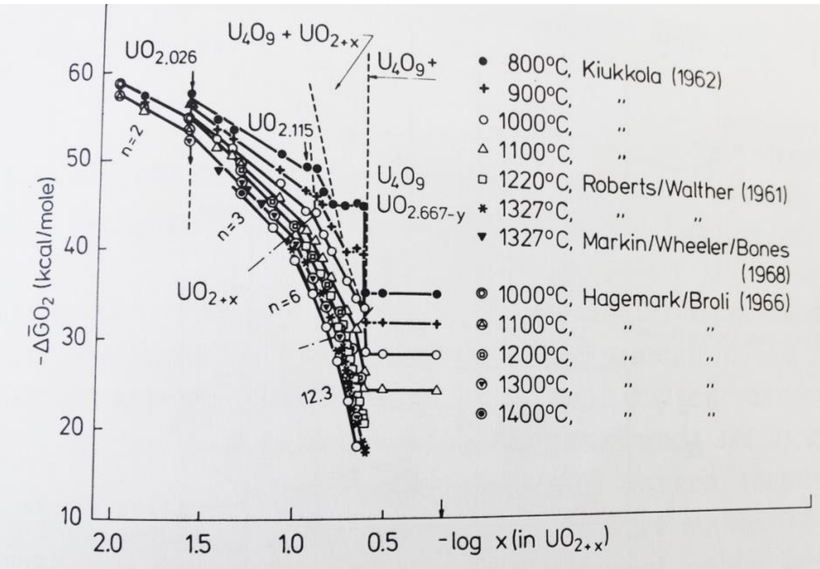

Figure 2-17: Relative Partial Free Energies of Oxygen, ΔG_{O2}, of UO_{2+x}, as a Function of -log(x). The Variable *n* Denotes the Exponent in the $pO_2^{1/n}$ [39].

Experiments have been done to understand the diffusion mechanism of Xe in UO_2 by doping with metals of different charges. It was found that the creation of either U vacancy or O vacancy does not promote diffusion of Xe in UO_2 matrix. It was concluded that the Xe diffusion must be accomplished through a complex defect structure, mostly likely through one U vacancy and two O vacancies [6]. This work later becomes the basis of many atomistic scale simulations, which will be discussed later.

2.3 Existing Fission Product Transport Models

Much simulation work is usually needed in the study of nuclear fuel due to the difficulties and costs associated with irradiation experimental work. In the study of fuel behavior, simulations have been used to interpret experimental data in order to understand the observations and to calculate and predict fuel behavior in a reactor. This section covers the earlier models, Booth's model and its variations, as well as the newer atomistic as well as meso-scale microstructure models.

2.3.1 Booth's Model

One of the earliest and most widely applied models in the study of FGR was developed by Booth [30], who assumed a spherical grain with perfect sink at the GB, as shown in Figure 2-8. The fission gas atoms were generated in the grain and migrated to GBs following the classical diffusion equation. The gas bubbles were considered released when they reached GBs. The amount of FG released could be calculated by integrating the diffusion equation over time over the GB surface. The release to birth ratio (R/B) can then be calculated using the derived relationship shown in Equation 2-19 where S/V is surface to volume ratio, D is diffusivity and λ is the decay constant. The model was also applied to deduce the diffusivity of fission gases from the experimental measurements. Booth's model was later modified to include other physics such as resolution of FG bubbles and trapping [15, 72, 73] to be incorporated in different fuel performance codes. Speight [72], for example, added a net mass flux term contributed by trapping and resolution effects, as expressed in Equation 2-20, where m is the amount of gas in the bubble, c is local concentration of gas atoms in the solution, g is the probability per second of a gas atom in the solution being trapped by a bubble, and b is the probability per second of a gas atom within a bubble being re-dissolved. These modifications generally improved upon Booth's model to make more precise predictions of gas release; however, the basic idea still followed Booth's model.

$$\frac{\mathrm{R}}{B} = (\frac{S}{V})(\frac{D}{\lambda})^{1/2} \qquad \text{Equation 2-19}$$

$$\frac{\partial \mathrm{m}}{\partial \mathrm{t}} = \mathrm{gc\text{-}bm} \qquad \text{Equation 2-20}$$

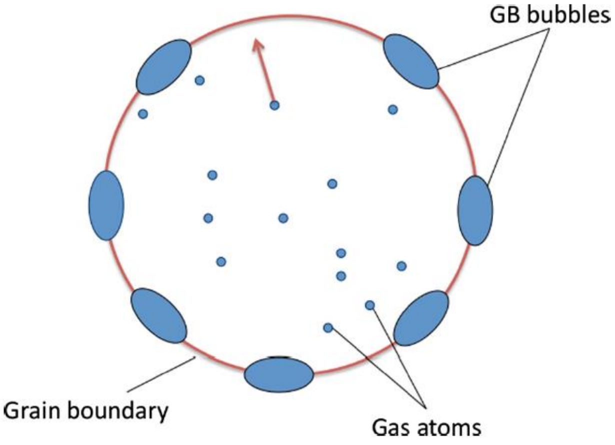

Figure 2-18: An Illustration of Booth's Model for Fission Gas Release. [74]

The issue concerned with Booth's model was mainly the over simplification of the geometry and the boundary conditions. The spherical grain model does not reflect the microstructure of UO_2, and the size considered is limited to a single grain. When applied in fuel performance codes, it did not predict the low FGR at the early stage of fuel life followed by the bursting phenomenon. However, Booth's model built the ground for the modeling work in the study of FGR, and most of the FG diffusivity values that are being used today are based on Booth's model.

2.3.2 Atomistic Simulation

In the atomic scale, the transport of FPs takes place mainly through the migration through the vacancies and interstitial sites. First principle studies to understand the intrinsic material behavior are often based on density functional theory (DFT) and molecular dynamics (MD) calculations. Molecular dynamics mainly studies the dynamic motion of atoms in a many body systems while DFT is based on quantum mechanical models that use electronic structures to study material properties. In particular, DFT has been commonly used among researchers to study the atomistic diffusion in UO_2. Liu et al. [75] demonstrated the capability of using DFT simulation to calculate different properties of nuclear fuels, including the transport behavior of Xe in UO_2. Andersson et al. [76], on the other hand, applied the method and calculated the xenon diffusivity in UO_{2-x}, UO_2 and UO_{2+x}. The results were comparable to existing experimental data. Atomistic studies were also applied to study different GBs [77, 78], and the GB energy as well as segregation energy for different GB types were calculated. Although very limited number of GB types was studied, the work found that the segregation energy for xenon to UO_2 GBs is higher at a random GB than at a CSL GB ($\Sigma 5$). The result agreed with CSL theory. The results of atomistic simulations helped provide an idea of intrinsic material behaviors as well as a reference to be compared with experimental data, especially when a large uncertainty exists in the experimental work. The atomistic studies also provided inputs to meso-scale models to study microstructural effect on nuclear fuel behavior.

2.3.3 Meso-scale Models and Percolation Theory

Meso-scale models have been developed to study microstructural effects on fuel performance. Techniques such as phase-field and finite element analysis are commonly used. They typically use the experimentally obtained material properties or first principle calculations as inputs to the partial differential equations and solve the material behavior at the microstructural level. The approach has been applied to study FG bubble evolution (Figure 2-19a), effective GB resistance (Figure 2-19b) as well as transport of FGs. Earlier meso-scale models began with 2-D models studied in a simulated network, and more complex models were later developed to study the effect in 3-D, as it is known that some physics, such as bubble morphology and percolation effect, have different behaviors in 3-D.

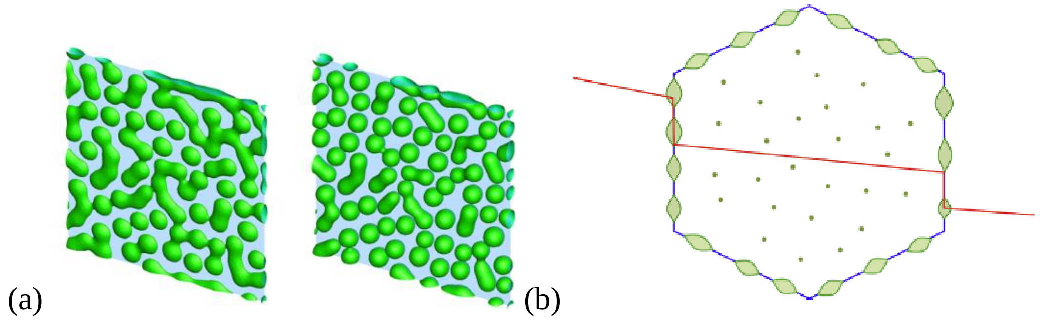

Figure 2-19: Examples of Meso-scale Models (a) FG bubble Evolution at a GB [79] (b) Bubble Enhanced Thermal Resistance at GBs [80].

The percolation theory has been applied in some meso-scale models to study the FGR mechanisms. The study conducted by Rudman et al. [81], built on the GB percolation analysis described in section 2.2.2 and conducted simulations with a real microstructure of UO_2, which contains 68% fraction of high diffusivity (D_2) GBs. The study set up a normalized concentration profile and observed the percolation paths at different diffusivity ratios, and the results are shown in Figure 2-20a. The percolation paths started to show at a D_2 to low GB diffusivity (D_1) ratio of 10^5 or higher, which is in a good agreement with Chen's work [55]. The effective diffusivity was also calculated and plotted versus log (D_2/D_1), and it is shown that the normalized diffusivity (D_{eff}/D_2) reached a constant value as the D_2/D_1 ratio increased above 10^4 (Figure 2-21). A similar study was also conducted in a larger scale by Millett [60] using a simulated network with no crystallographic information (Figure 2-20b). The work included lattice diffusion of FGs and conducted a percolation study on FG saturated GBs. The obtained percolation threshold in 2-D was about 0.65, a close match with other studies. Although the percolation results seemed to match in different studies, it was believed that the complex grain microstructure in 3-D can make a difference. These simulations were also very preliminary as they did not take into account other effects such as temperature and fuel stoichiometry, which are known to have a big impact on the transport behavior and subsequently, the percolation behavior.

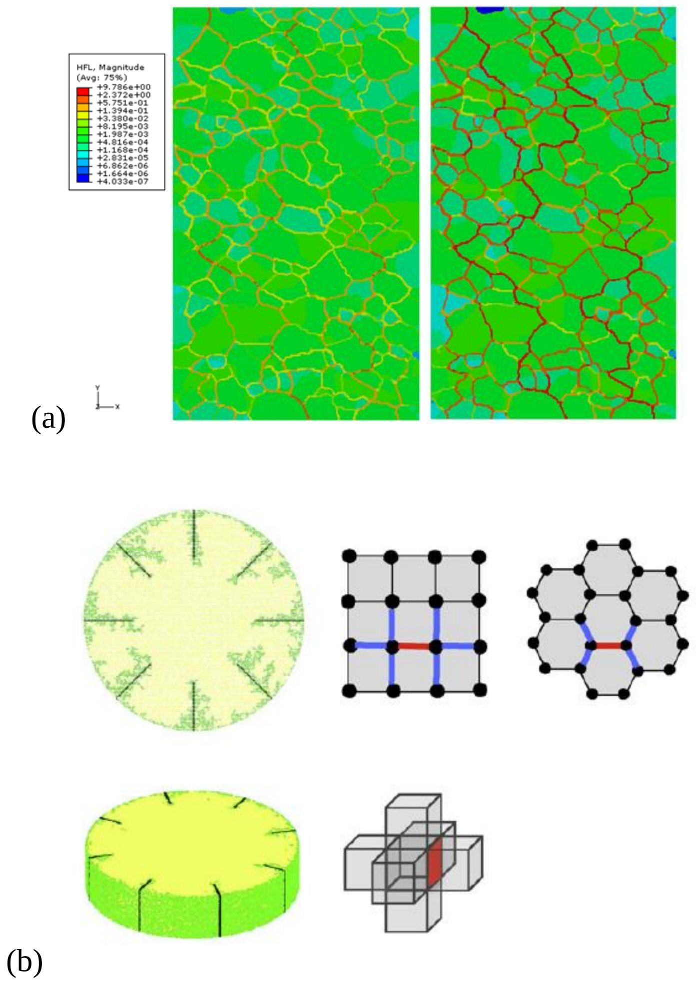

Figure 2-20: (a) Diffusion Flux from the Simulation Result in a 2-D Microstructure with Diffusivity Ratio of 10^6, 10^7 (From Left to Right) [81] (b) 2-D GB Networks Used to Study the Percolation of Saturated GBs.

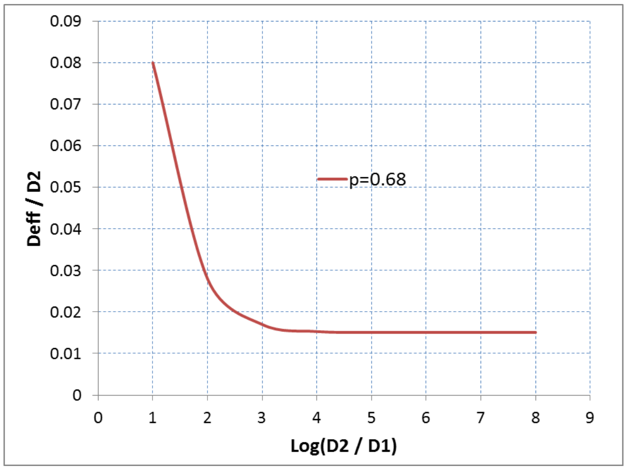

Figure 2-21: Effective Diffusivity under as a Function of Diffusivity Contrast for the Simulation in 2-D Microstructure [81].

In order to have a better understanding of FP transport and its effect on nuclear fuel elements, a more realistic model is needed. The model needs to reflect the complex geometry in 3-D as well as other effects such as temperature, stoichiometry and GBs. The effects of GBs, in particular, need more attention as they are dominating the FGR behavior. The variation in GB properties due to crystallography is rarely addressed in past studies of FGR; however, more and more evidence has shown that differences in GB properties introduced by differences in GB crystallography can certainly affect the percolation behavior studied in a microstructurally explicit model. As a result, there is a need to develop new tools that can take the abovementioned complex physics into account to tackle this problem.

3. OBJECTIVES

The objective of the work is to develop a microstructurally explicit model to study the behavior of oxide nuclear fuels. The nuclear renaissance that started about a decade ago put an emphasis on material modeling work in order to predict fuel behavior better and to develop next generation fuels with better thermal and mechanical performance. The earlier works on fuel modeling are mostly analytical and describe mainly the bulk behavior while a lot of recent work has focused on atomistic simulation. More meso-scale models are needed to bridge the gap between the bulk behavior and the atomistic models.

Very few 3-D microstructurally explicit models are available in the literature, and most of which are applied only to provide geometric information. No meso-scale model, to the best of the author's knowledge, has been developed to take into account crystallographic information, which is known to affect material behavior. The present work looks to take advantage of the advances in material characterization techniques and computational capability by developing a model that contains both the geometric and crystallographic information of UO_2 from actual microstructures obtained from characterization, to perform finite element simulations of fuel behavior.

To be more specific, the goal is to create a 3-D meso-scale model to verify and predict the evolution of fission product transport and the thermal performance of UO_2 at low burnups, taking into account the complex physics that are important for this problem: grain bulk and grain boundary (GB) diffusion, triple junction (TJ) diffusion, temperature dependent material properties, material stoichiometry and GB thermal resistance. The model needs to be in 3-D and multi-physics to account for 3-D geometric effects and coupling between temperature and mass transport given by all the temperature dependent properties in a high temperature gradient environment. The heterogeneity of material properties will be included based on the crystallography data obtained from the sample characterization. The model will be simulated using COMSOL^{TM}, a platform for multi-physics simulation using finite elements, and the complex interactions between different mechanisms can be combined and studied in one model.

The work can be broken down as follow:

- Reconstruct the microstructure of UO_2 samples in 3-D. Apply serial sectioning techniques to collect a series of orientation imaging microscopy (OIM) using electron backscattered diffraction (EBSD) and focused ion beam (FIB). Develop a procedure for 3-D reconstruction.
- Characterize and compare the samples using 2-D EBSD data and the reconstructed 3-D model. Study the results to have a good understanding of the difference between 2-D and 3-D characterization and between different samples. The GBs will be characterized based on misorientation angles and coincident site lattice theory to provide additional information for simulations.
- Study the physics of FP transport and heat conduction in nuclear fuels and derive the necessary equations to be applied to the model. Calculate the bulk fuel behavior based on reactor operating conditions to obtain parameters needed to simulate different fuel behaviors.
- Verify the analytical work using a bi-crystal model.

- Conduct simulations for each variable, including stoichiometry, GB diffusion, TJ and heat transfer, individually to study their effects on fission product transport and heat conduction. A sensitivity analysis will be conducted to check the effect of material properties with a large uncertainty.
- Conduct multi-physics simulations for different samples to study the effect of different microstructure geometry and crystallography on fission product transport.

4. EXPERIMENTAL PROCEDURES AND CHARACTERIZATION RESULTS

A microstructurally explicit model requires a thorough understanding of the microstructural features and statistics of the studied samples. This chapter is dedicated to the experimental procedures, which include sample preparation methods and characterization techniques. Figure 4-1, which is an Electron Backscattering Diffraction (EBSD) data superposing on top of a Scanning Electron Microscopy (SEM) image, shows an example of the information to be collected from the characterization work, including electron micrographs, grain orientation images and grain boundary (GB) character. The different grain orientation and GBs are labeled with different colors, and the information is used to provide statistical data and to create finite element models. This chapter provides the detailed procedures for both experimental and characterization work. The obtained characterization data in 2-D and 3-D will also be presented.

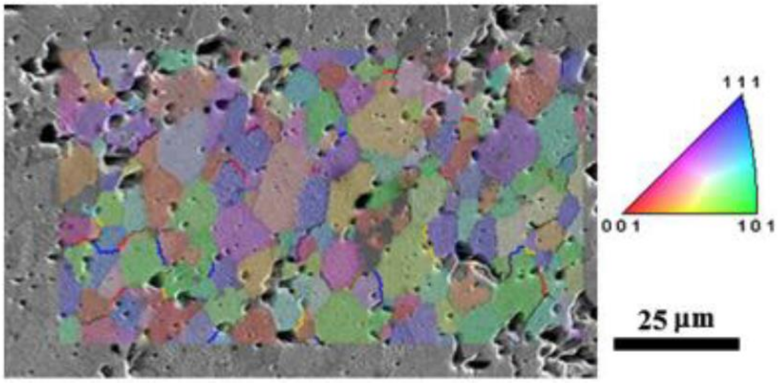

Figure 4-1: SEM and EBSD Image for a Porous UO_2 Sample Showing the Crystallography Orientation and the Types of Special GBs.

4.1 Experimental Procedures

The work began with sample preparation and data collection, which was completed in Los Alamos National Laboratory (LANL). It was followed up by sample characterization work and data analysis done by Karin Rudman et al. [82, 83].

4.1.1 Sample Preparation

Depleted uranium dioxide pellets with oxygen to uranium ratio of 2.00, 2.06 and 2.14 were fabricated and serial sectioned in LANL. The detailed fabrication process can be found in [82]. To briefly describe the process, the sample preparation started with depleted $UO_{2.16}$ powder, which was milled and passed through a mesh to ensure a uniform particle size. They were then cold pressed at 40 MPa into cylindrical pellets using a 5.7 mm diameter die. The pellets were then placed in a furnace to be sintered. All samples went through a heating ramp of 5°C/min to 1350°C when they were held at the temperature for two hours. The samples were then cooled to room temperature at a rate of 5°C/min [84]. The control of oxygen content in the UO_2 samples was achieved by controlling the oxygen partial pressure in the environment. The samples were then roughly polished with SiC papers for serial sectioning using focused ion beam (FIB) and EBSD.

4.1.2 Microstructure Characterization Techniques

The samples were characterized and serial sectioned at LANL using a FEI Helios Nano Lab 600 Dual Beam SEM and serial sectioned with a FIB along the radial direction of the pellets. At each section, an Orientation Image Map (OIM) was obtained using the

EBSD detector. An EBSD detector collected the diffraction pattern, which is also known as Kikuchi band, and reveals the grain orientation at each spot being scanned [85]. Figure 4-2 is a quick illustration of the EBSD technique. An area of approximately 30 μm by 40 μm was scanned for each slice for each sample. The FIB was used to remove from 0.33 μm to 0.5 μm of material after each scan. The ion beam energy for serial sectioning was 30 keV and 21 nA, while secondary electron images and EBSD scans were obtained with electron beams operating at 20 keV and 2.7 nA [84]. The obtained data contained different numbers of slices and spacing between slices between different samples. The density and a summary of serial sectioning information for the samples are listed in Table 4-1. The depth resolution is limited by the slice spacing, and the lateral resolution depends on the beam size, which is about 0.2 μm. The total depth of the depth of the data collected varies between 30 to 50 μm. Fiducial marks, as shown in Figure 4-3a, were made on the samples as references for alignment during the serial sectioning process to provide information of the amount of material removed. Figure 4-3b and c provided examples of the information collected during each serial sectioning scan, which contains both SEM and EBSD images.

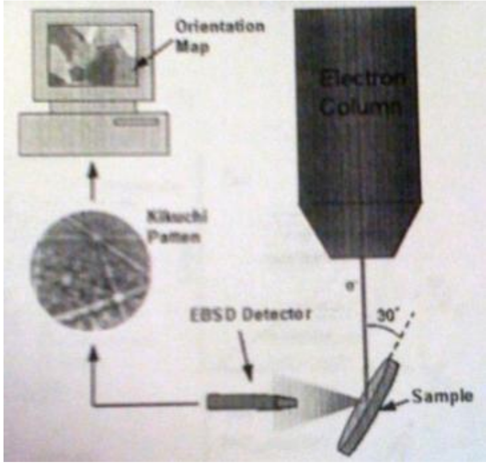

Figure 4-2: An Illustration of the OIM Technique [85].

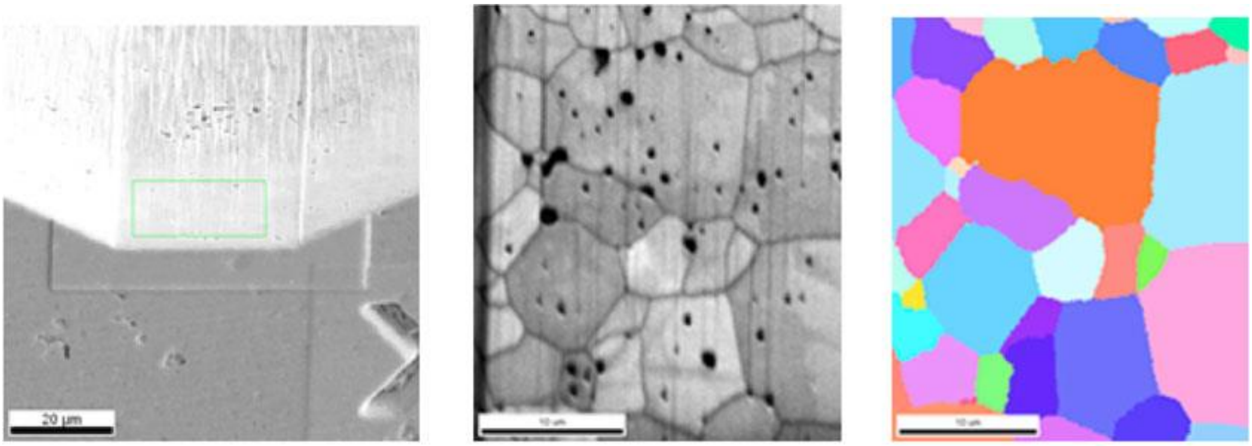

(a) (b) (c)

Figure 4-3: Examples of the Images Obtained from SEM and EBSD (a) SEM Image of a Sample Undergoing Serial Section Along the Vertical Direction. A Fiducial Mark Was Made in the Lower Right Corner. (b) Image Quality Map from EBSD. (c) Orientation Map from EBSD [84].

Table 4-1: Serial Sectioning Information for $UO_{2.00}$ $UO_{2.06}$ and $UO_{2.14}$

Sample	$UO_{2.00}$	$UO_{2.06}$	$UO_{2.14}$
Theoretical Density (TD)	91%	94%	92%
Slice spacing (μm)	0.33	0.33	0.5
Number of slices	160	105	87

4.1.3 Three Dimensional Characterization Technique

The serial sectioning data will be used to create 3-D models, and the procedures of which will be discussed in detail in the next chapter, which addresses the model development for finite element simulation. In addition to the simulation purposes, the 3-D models are also very important from the characterization perspective. First of all, they reveal the grain shapes in 3-D which can vary significantly from 2-D data if any texture is present. It is also known that in order to fully characterize a GB, one needs three variables to specify the misorientation angles and two to specify the GB normals [86, 87]. A 2-D OIM image cannot fully characterize the five parameters of a GB. In addition to the grain orientations (Euler angle), the GB normals in 3-D are also needed. The GB lines in 2-D images are only projections of the GB planes to the scanned surfaces which do not reflect the GB orientation in the 3-D space.

To fully characterize a GB, a technique was developed to measure the GB normal in 3-D using the reconstructed 3-D microstructure. The top left figure in Figure 4-4 shows a reconstructed triple junction (TJ) surround by three grains and three GBs. In AVIZO^{TM}, GB planes can be represented by making cut planes tangential to the GB in the 3-D space. The GB normal can then be obtained knowing the normal to the cut plane. Note that the collected data represent only the GB normal at the studied layer near a TJ and cannot reveal the curvature that may exist in a GB; however, the information is still valid for the layer studied. The information collected can also be applied to calculate the dihedral angle at a TJ in 3-D.

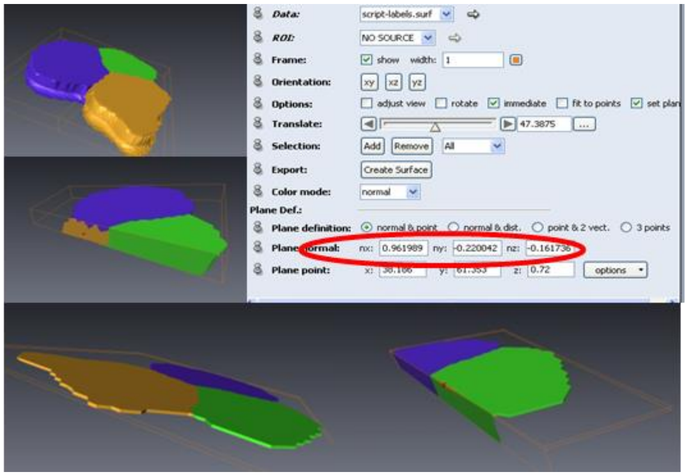

Data: script-labels.surf
ROI: NO SOURCE
Frame: ☑ show width: 1
Orientation: xy xz yz
Options: ☐ adjust view ☐ rotate ☑ immediate ☐ fit to points ☑ set plan
Translate: 47.3875
Selection: All
Color mode: normal
Plane Def.:
Plane definition: ● normal & point ○ normal & dist. ○ point & 2 vect. ○ 3 points
Plane normal: nx: 0.961989 ny: -0.220042 nz: -0.161736
Plane point: x: 38.166 y: 61.353 z: 0.72

Figure 4-4: Measuring GB Normals by Making Tangential Cut Planes Along the GBs Using AVIZO^{TM}.

4.2 Characterization Results

The three stoichiometric samples were characterized in both 2-D and 3-D by Rudman et al. [83, 84]. The characterization results are very important to the development of finite element models as they will be used to determine the applied material properties. The data will be shown for the three FIB samples in both 2-D and 3-D. The information such as grain sizes, GB misorientation angles and CSL of each sample will be compared.

4.2.1 Microstructure Information in 2-D

For statistical purposes, three larger scans, each with an area of 400 μm by 400 μm, were obtained from the work published in [83] for the three stoichiometric samples. The scanned areas were chosen to be the center of the pellet, the edge of the pellet and the middle between the two to catch possible variation in microstructure from the sintering. The data obtained from the large scans will be used as the representative 2-D data as they contain a lot more grains and GBs than the FIB data.

First of all, the average grain size over the three areas for each sample is 6.0 μm, 5.7 μm and 6.3 μm for O/M ratio of 2.00, 2.06 and 2.14, respectively. The distribution of the three scans for each sample is shown in Figure 4-5. The distributions vary with each sample. $UO_{2.00}$ has larger grains at the edge while $UO_{2.06}$ has smaller grains in the center, possibly a result of higher edge temperature during sintering. The $UO_{2.14}$ has the largest average grain size which can be a reflection of its higher oxygen content. The distributions for the three scans are similar for $UO_{2.14}$.

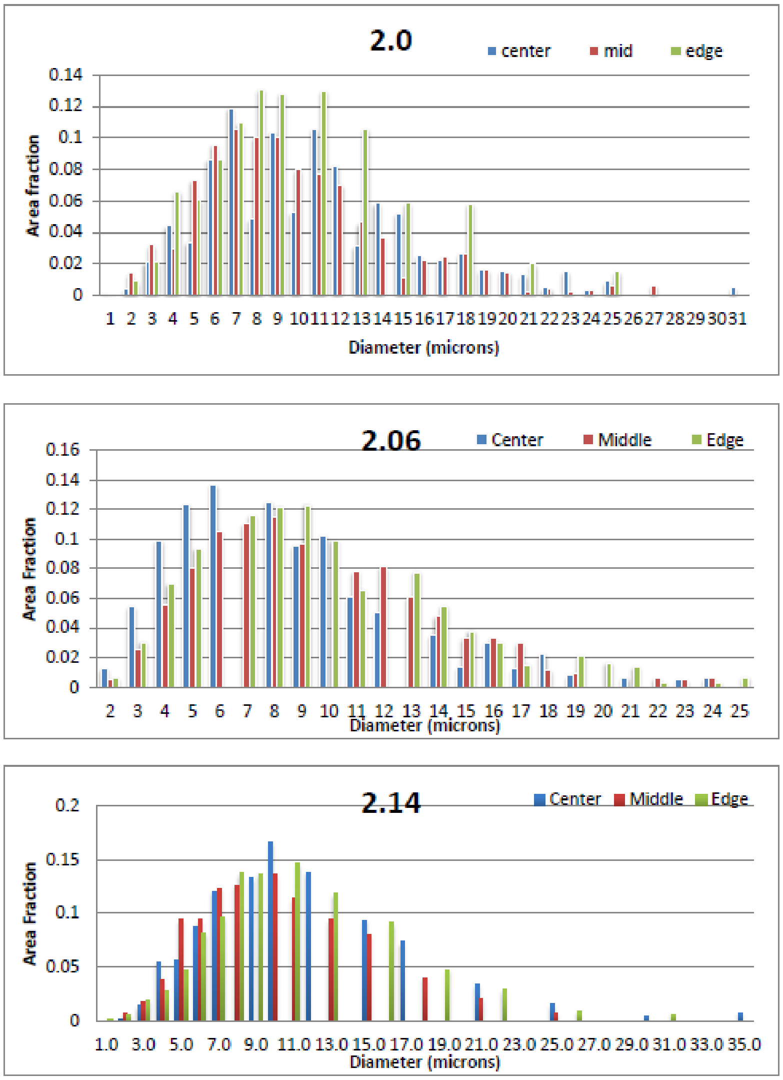

Figure 4-5: Distribution of Grain Size of the Samples with Different O/M Values from 2-D Data [83].

4.2.2 Grain Boundary Misorientation Angle Distribution

The GB misorientation angles affect the GB energy and thus the diffusivity of materials as discussed in Chapter 2. From the large 2-D scans, the distributions of GB misorientation angle distribution for the three samples were plotted in Figure 4-6, taken from [83]. The distribution is consistent for all three samples with a peak at around 45°

and a maximum angle at around 60°, as constrained by the symmetry for a cubic crystal. The GBs are mostly high angle GBs.

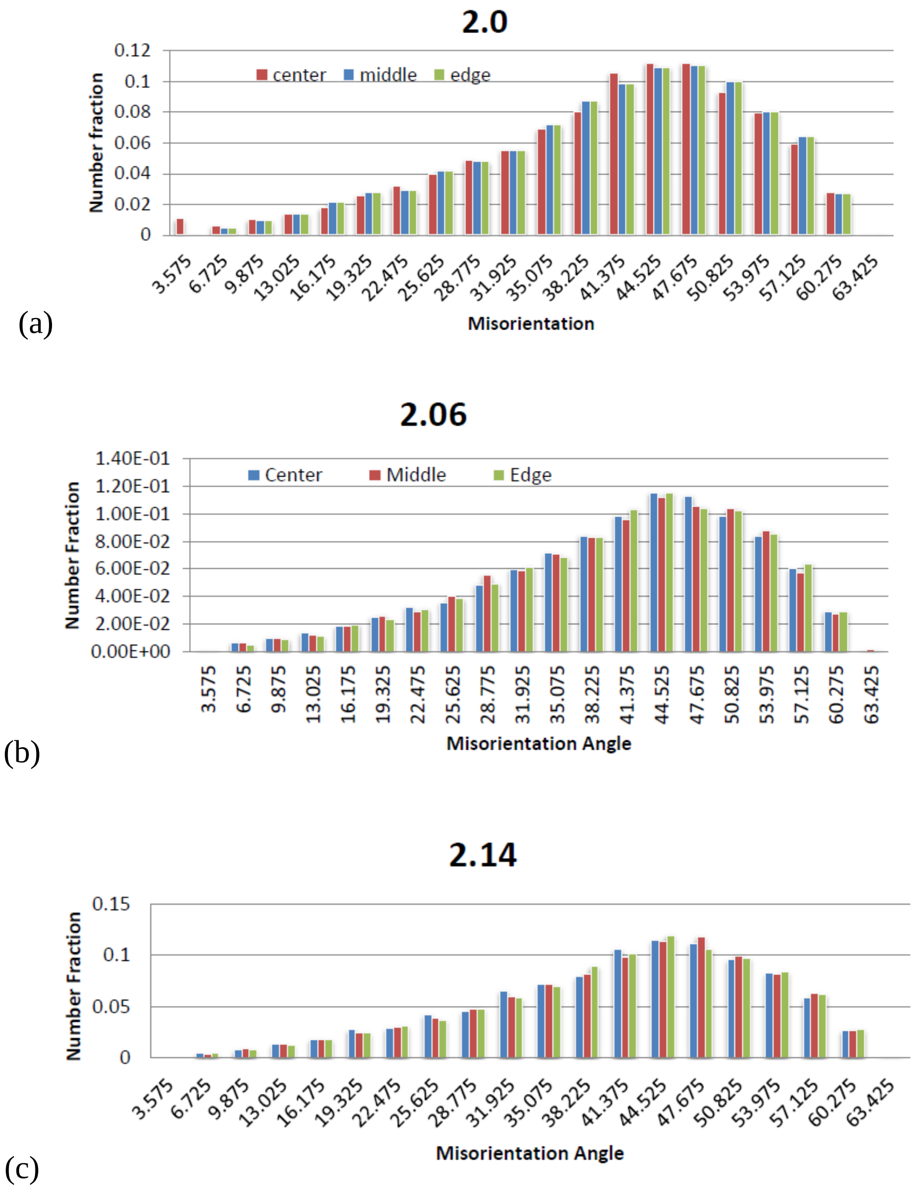

Figure 4-6: Grain Boundary Misorientation Angle Distribution (a) $UO_{2.00}$ (b) $UO_{2.06}$ (c) $UO_{2.14}$ [84].

The distributions of special GBs, known as coincident site lattice (CSL), were also collected and plotted for each sample as shown in Figure 4-7. Large variation exists between samples. It is also observed that most of CSL GBs have low Σ. For this reason along with the fact that they have more coincident sites, only the GB with Σ value of 11 or less will be considered in the simulation work. Their distribution in 3-D will be characterized in the 3-D models.

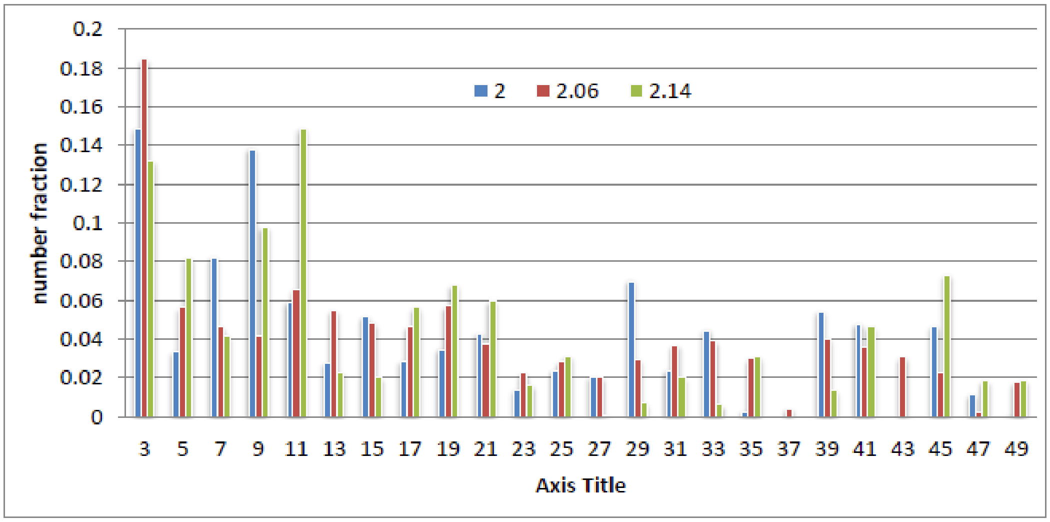

Figure 4-7: Coincident Site Lattice Distribution for Both $UO_{2.00}$ and $UO_{2.06}$ Samples [84].

4.2.3 Characterization Results from 3-D Reconstruction

The FIB data were used to reconstruct 3-D models, and the models can be used to provide statistics in 3-D. Serial sectioning slices are shown in Figure 4-8 as an example of the FIB data. The figures show the change in grain shape through the thickness. Each slice contains the same information that was obtained from the 2-D data. The reconstructed surfaces for the three sets of FIB data are shown in Figure 4-9. From the appearances of the outer surfaces, the sample $UO_{2.00}$ has several large, elongated grains along radial direction surrounded by many smaller and slighted elongated grains. The $UO_{2.06}$ sample has a more uniform distribution with the presence of many small grains. The $UO_{2.14}$ also have elongated grains but with smaller aspect ratios. The grain size also looks similar with many large grains.

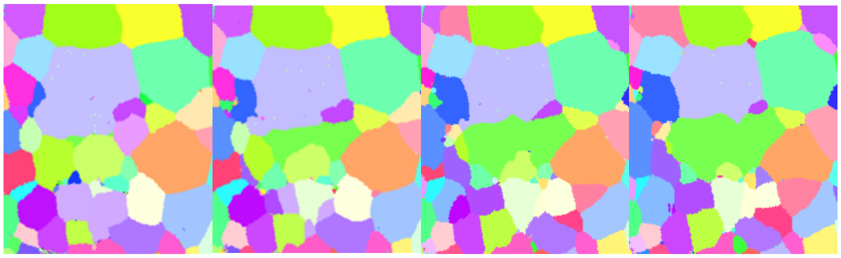

Figure 4-8: Serial Sectioned Microstructure of $UO_{2.14}$ Sample [84].

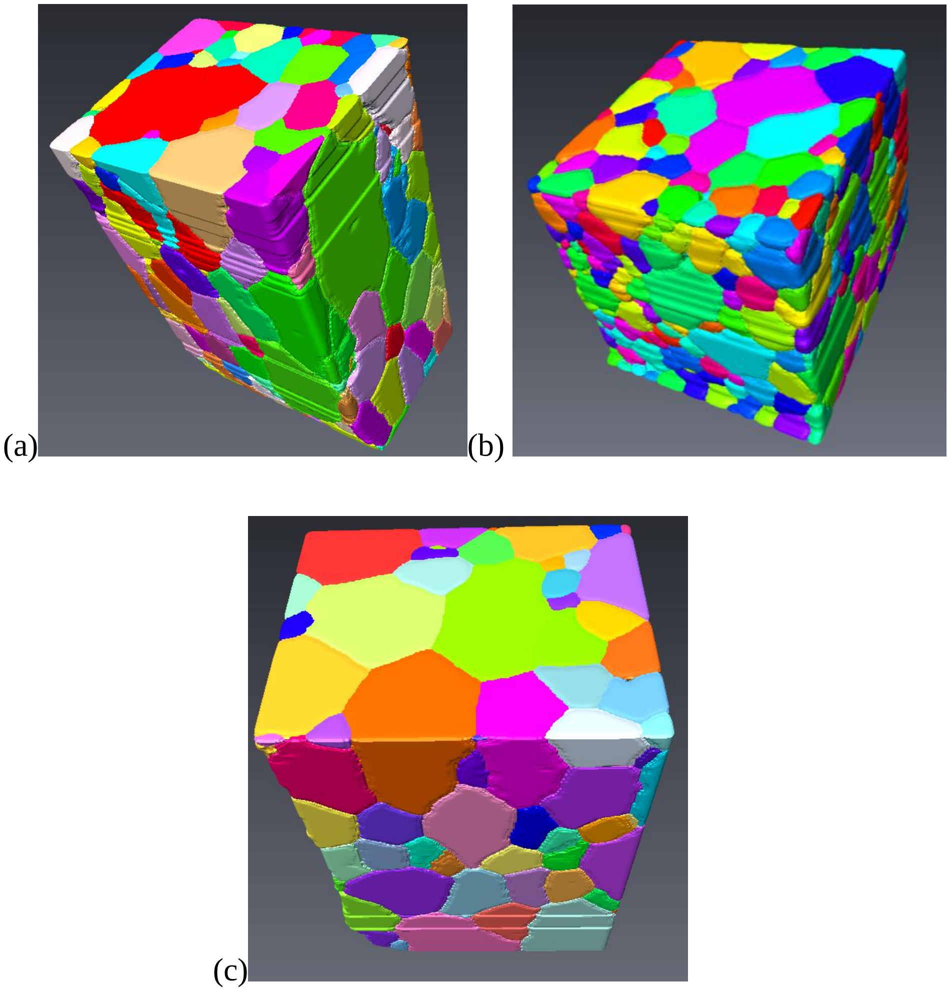

Figure 4-9: 3-D Microstructure Reconstructions for Different Samples: (a) $UO_{2.00}$ (b) $UO_{2.06}$ (c) $UO_{2.14}$.

The volume of each grain in the reconstructed models can be measured using AVIZO^{TM}, and the grain size in diameter can be calculated assuming spherical grains. Based on the calculation, the average grain sizes for the three samples are 5.3 μm, 3.9 μm and 4.3 μm for $UO_{2.00}$, $UO_{2.06}$ and $UO_{2.14}$, respectively. The grain size distributions for the three samples are shown in Figure 4-10. For $UO_{2.00}$ the majority of the grains have a grain size of 4 μm to 5 μm with the presence of a few very large grains that are over 15 μm. For $UO_{2.06}$, there are more small grains with most grains below 10 μm. The $UO_{2.14}$ has a grain size distribution peak at 4.5 μm with most grains below 12 μm. The measurements agree qualitatively with visual inspection.

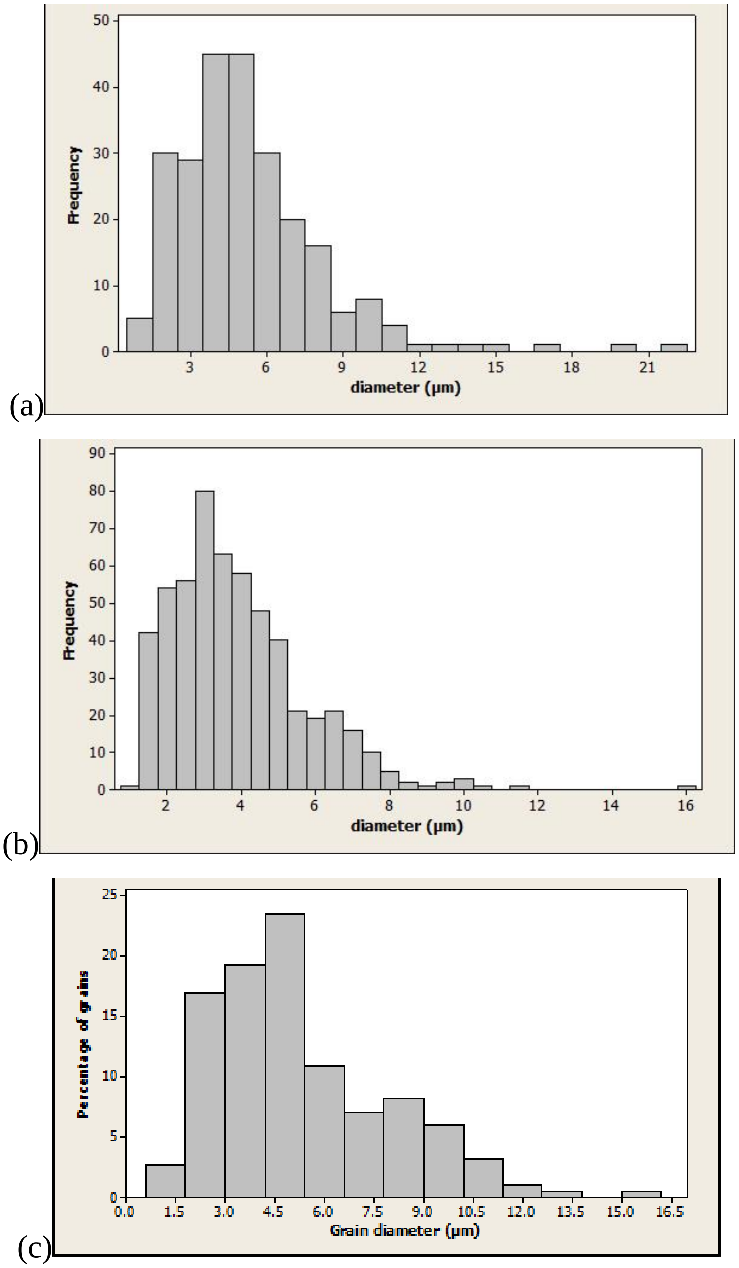

Figure 4-10: 3-D Grain Size Distribution for (a) $UO_{2.00}$ (b) $UO_{2.06}$ (c) $UO_{2.14}$

Another approach, which was used in [83] to collect grain size statistics, is to combine a series of serial sectioning slices into one image (Figure 4-11). The information such as distribution of grain size and GB misorientation angle can then be obtained fairly easily without the reconstruction process. However, it is hard to determine the spacing between selected slices and double counting or under estimation can happen, especially for samples with a large spread in grain size. The average grain size obtained from this approach is 3.6 μm, 3.4 μm and 3.6 μm for $UO_{2.00}$, $UO_{2.06}$ and $UO_{2.14}$, respectively.

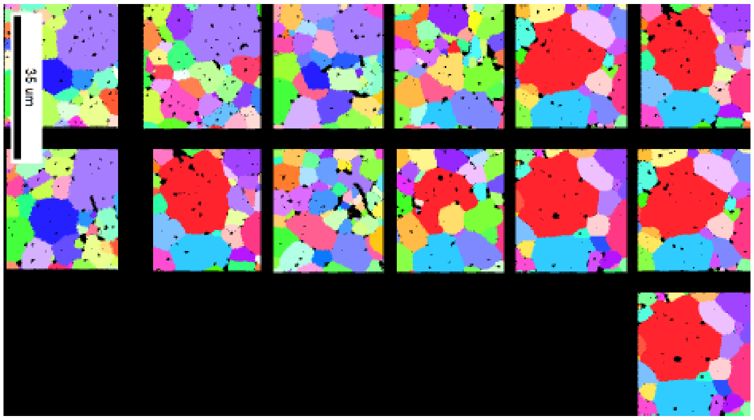

Figure 4-11: Selected Slices from FIB Serial Sectioning Set of Sample $UO_{2.00}$ for Calculating Grain Size across Thickness

Table 4-2 provides a summary of grain size obtained from different approaches. The 2-D data is the most reliable as it contains a much larger data set, if no texture is present. The values obtained from FIB data are smaller in general. The FIB slices in 2-D approach underestimated the 2-D results the most. The reason can be a combination of higher fraction of grains cut off by the boundaries and local variation. From the perspective of fission gas transport, it is expected to have faster transport rate in the $UO_{2.06}$ sample, which has the smallest grains in the three models, when the GBs are the high diffusivity paths. However, the actual behavior will also depend on the distribution of these grains and the heterogeneous GB properties.

Table 4-2: Average Grain Size Obtained using Different Approaches for the Three Stoichiometric Samples

	Average grain size (μm)		
O/M	2-D	FIB Slices in 2-D	3-D Reconstruction
2.00	6	3.6	5.3
2.06	5.7	3.4	3.9
2.14	6.3	3.6	4.7

4.3 Triple Junction Study and Grain Boundary Connectivity

In addition to the stoichiometric samples, a UO_2 sample with 95% density was studied to obtain statistical information of the dihedral angle distribution. The information is valuable to the understanding of interface energy. Moreover, the connectivity of the GBs was evaluated using the homology metrics [88], which can provided a different perspective to understand the percolation behavior.

4.3.1 Dihedral Angle at Triple Junctions

A TJ, a line where three GBs meet, is an important microstructural feature that reveals the interfacial energy of the GBs [42]. Characteristics at triple junctions can be used to obtain indirect measurements of GB energies and to provide some initial insight as to the importance of GB character and topology on transport properties. It has been used to explain some observed phenomena such as grain growth and wetting [89]. The interface energy needs to be balanced at a TJ, as shown in Figure 4-12a. The resulting relationship is expressed in Equation 4-1, where X is the dihedral angle and γ is the interfacial energy. For an isotropic material, given that all GBs have the same energy, the three dihedral angles should be 120°, one of the reasons that many meso-scale models employ hexagonal grains. However, that is rarely the case due to the differences in misorientation angle resulting in different atomic structure and thus different GB energy [89, 90]. The dihedral angle at a triple junction can be measured from the 2-D EBSD data as shown in Figure 4-12b. Measurements in 3-D can also be collected using the approach discussed in section 4.1.3.

$$\frac{\gamma_1}{sinX_1} = \frac{\gamma_2}{sinX_2} = \frac{\gamma_3}{sinX_3} \qquad \text{Equation 4-1}$$

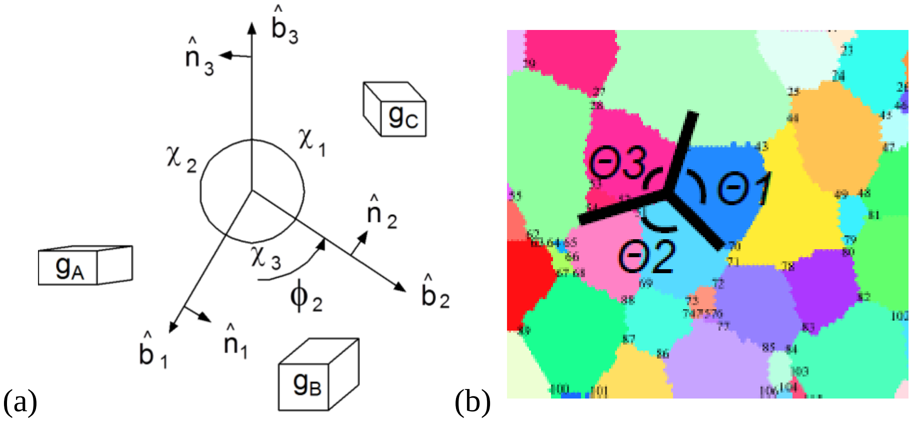

Figure 4-12: (a) A Triple Junction Surround by 3 Grains, g_A, g_B, g_C and 3 GBs, $b_{1,}$ b_2 and b_3. X Represents the Dihedral to the Corresponding GB [89] (b) Dihedral Angle Measurement from a 2-D EBSD Data

Measurements were performed on a 95% fully sintered UO_2 sample in both 2-D and 3-D to study the distribution of the dihedral angles. For 2-D measurements, two areas of 60µm x 100µm were analyzed, and a total of 503 triple points were identified. Note that only two out of three dihedral angles measured at each TJ are taken into account in the statistical analysis because the third dihedral angle is determined by the values of the first two measurements. A preliminary statistical analysis was conducted, and the distribution was plotted in Figure 4-13. It showed a normal distribution that peaked at about 120°, in agreement with literature. Three dimensional measurements were also made for over 100 TJs on the same sample. The resulting distribution curve had a peak at 140° with higher distribution at both ends of the curve, indicating the presence of some very high and low dihedral angles values. It also suggested an underestimation from the 2-D measurements. To check the correlation of the dihedral angles at a TJ, the two dihedral angles as a pair from 3-D measurements were plotted in a 3D histogram shown in Figure 4-14. It showed that most pairs have both dihedral angle between 110° and 130°, which is a closer match of the theoretical value for equilibrium interfacial energy at the TJs.

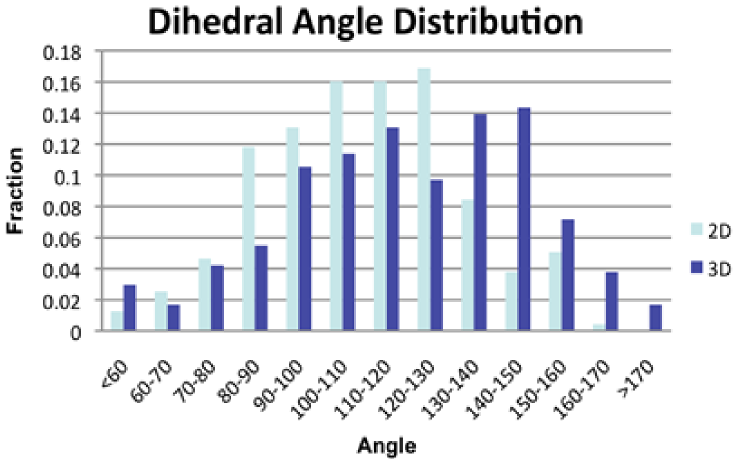

Figure 4-13: The Distribution of Dihedral Angles at Triple Junctions for a 95% Density UO_2 Sample

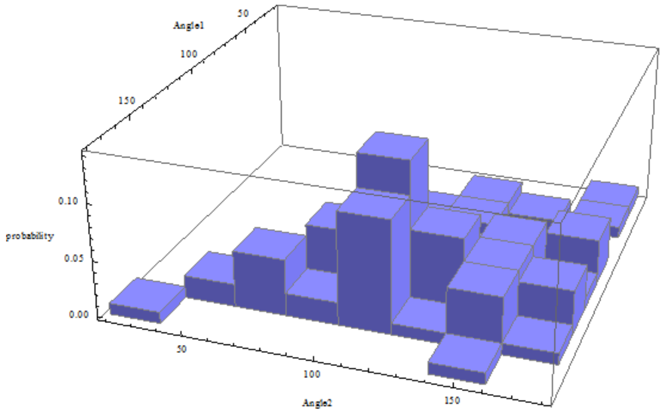

Figure 4-14: A Histogram for 3-D Dihedral Angle Pairs: X-axis Is a Dihedral Angle Measured at a TJ, and Y-axis Is the Corresponding Dihedral Angle at the Same TJ.

4.3.2 CHomP Study of Connectivity

In the study of diffusion in a GB network, the simulation work from [81] has shown that the concentration distributions are different for different networks. Figure 4-15 demonstrated that even when all three cases have percolating networks, the resulting concentration profiles still vary. The results indicate that the behavior of mass transport is affected not only by GB character but also by their distribution and connectivity. It has been shown that the connectivity of a GB network can be characterized using a parameter called homology metrics, which can be calculated using the software known as Computational Homology Project (CHomP) [88, 91]. The software reads images of GB network in .bmp format and calculates the number of independent components (β_0) and the number of holes (β_1). The value for β_0 represents the number of connected GBs. In a GB network that is fully connected, the value for β_0 should be 1 and the value for β_1 should be the number of grains. The ratio (β_{01}) of β_0 to β_1 provides an insight to the connectivity of the networks. A well connected network should have a small β_{01} value and a poorly connected network should have a large β_{01} value.

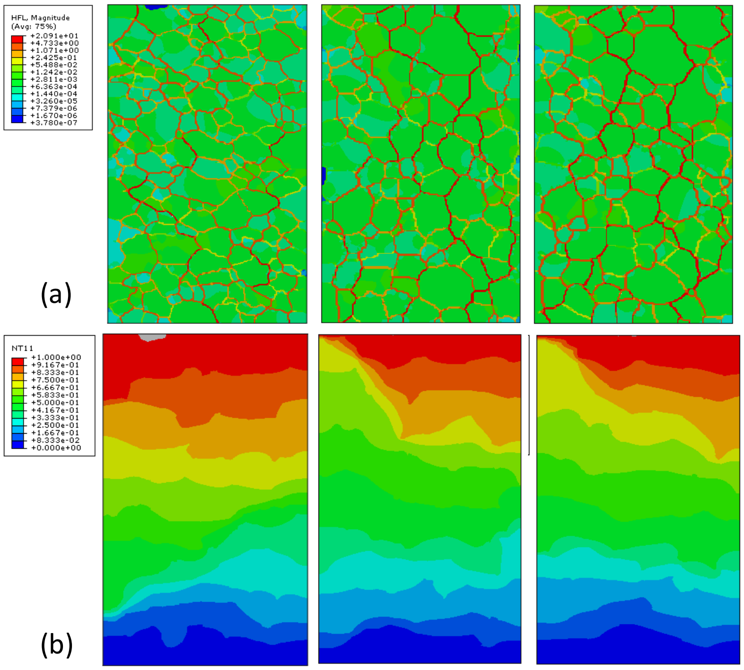

Figure 4-15: (a) Percolation Paths in Different 2-D GB Networks (b) The Resulting Concentration Distribution from the Percolation Paths [81].

Examples of GB network for the software are shown in Figure 4-16, where (a) contains all GBs while (*b*) contains only high diffusivity GB as defined in [81]. It was found, based on several different GB networks, that when including all GBs in a network, β_{01} holds a value between 0.009 and 0.02, which indicates a well-connected network. When only high diffusivity GBs are considered in the network, the β_{01} values range from 0.48 to 1, with around 68% of high diffusivity GBs. These values obtained from well-defined GB networks provide references to different types of network to be studied.

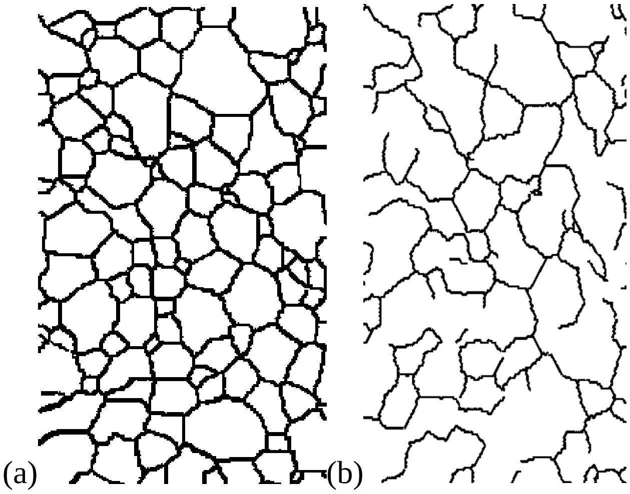

Figure 4-16: Examples of the GB Networks for ChomP Analysis (a) A Fully Connected Network Including All GBs (b) A Network with Only High Diffusivity GBs.

The variable that is the most comparable to the study of mass transport should be the mass flux because they include the relationship between the orientation of a GB and the direction of the applied concentration gradient, in addition to GB properties. To study the connectivity of GBs with high mass flux, the flux profiles in Figure 4-15 are filtered in Photoshop using the same threshold parameters to show only high mass flux value as shown in Figure 4-17 below. The homology parameters are calculated for each case and listed in Table 3. It is shown that the β_{01} value is the largest for Case (a) and the smallest for case (c). The values indicate that the network in Case (a) has a poorly connected high flux network while Case (c) is better connected by the high mass flux boundaries, resulting in a different concentration profile in Figure 4-15b. The better connected network represents a better defined percolation paths and thus resulting in a smaller fraction of high concentration area. This study sets an example of applying homology metrics to the study of mass transport and relating them to the concentration distribution.

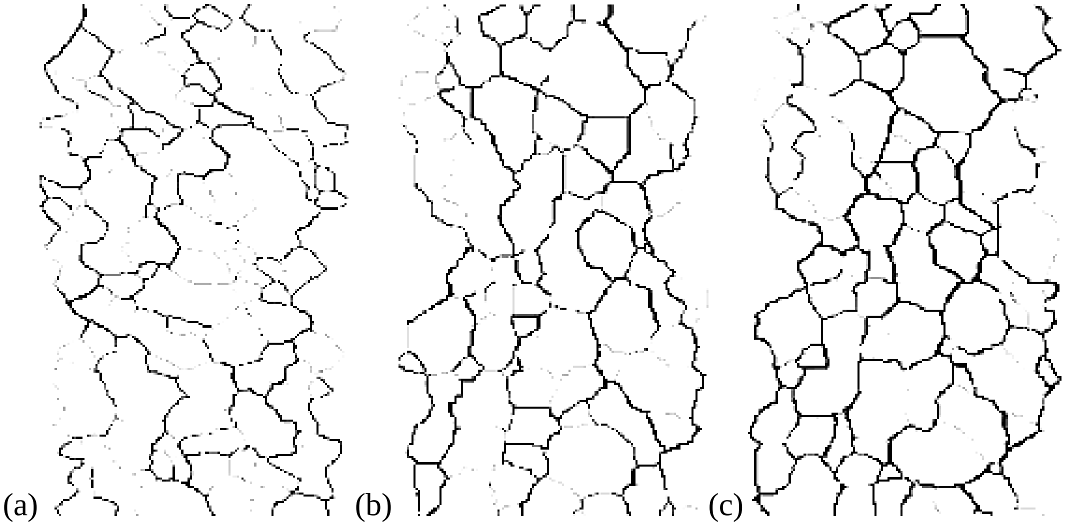

Figure 4-17: The Flux Profiles from Figure 4-15 after Threshold to Show Only High Flux GBs. The Figures Are Listed in the Same Order as Figure 4-15.

Table 4-3: Homology Parameters for the Geometries in Figure 4-17

Figure 4-17	β_0	β_1	β_{01}
(a)	180	0	Infinity
(b)	90	2	45
(c)	45	10	4.5

The GB analysis obtained from this chapter will provide inputs to the material properties to be assigned during model development process, which will be discussed next. Other information, such as grain size and GB connectivity, in both 2-D and 3-D will provide valuable information for comparing different simulation results in order to understand the transport behavior of FPs.

5. FINITE ELEMENT MODEL DEVELOPMENT AND SIMULATION PROCEDURES

In order to build the microstructurally explicit models required to achieve the goals of this work, the information collected from the characterization results needs to be translated into finite element models for simulation. This chapter discusses the procedures developed for 3-D microstructure reconstruction along with calculations used to derive the reactor environment in which the transport behavior will be studied. It also covers how different physics are coupled and applied to the model.

5.1 Model Reconstruction

The first step on the modeling procedure is the microstructure reconstruction. It is achieved by stitching serial sectioning slices into a 3-D microstructure model. The reconstruction process starts by using the segmentation tools in DREAM3D^{TM} software so that EBSD data can be used to create a 3-D model of the microstructure that contains crystallographic information. Three dimensional surfaces and 3-D mesh elements are then created using AVIZO^{TM} software. The mesh file is then passed on to COMSOL^{TM} software where multi-physics simulations are conducted.

5.1.1 Microstructure Reconstruction

It is known that many microstructural features affect material properties and performance. Most of earlier work tried to capture and understand the effects in 2-D; however, more recent work [92] has suggested that microstructures need to be studied in 3-D as actual materials can behave very differently from 2-D predictions. This particularly applies to the study of geometrical effects such as percolation, topology and connectivity of certain microstructural features.

The reconstruction of the microstructure of a UO_2 pellet is an essential first step to create a microstructurally-explicit finite element model. Many researchers have dedicated their work to improving the techniques and developing algorithms to accelerate and automate the process [92, 93]. The reconstruction process usually begins with a series of OIM images (Figure 5-1a) obtained from EBSD, and the images go through a series of pre-processing steps, such as threshold, alignment, segmentation. The threshold process basically cleans up the noise in EBSD data while the alignment makes sure all images are aligned. Confidence index (CI) and image quality (IQ) from EBSD data are the commonly used threshold parameters. The step that follows is image segmentation, which assigns each grain with a label as shown in Figure 5-1b. After each grain is assigned with a label for all the images, visualization software such as AVIZO^{TM}, can be used to interpolate the GBs into a 3-D network based on the labels assigned.

The final products can be a GB network or a 3-D volume as shown in Figure 5-1c and d. The process of reconstructing a 3-D microstructure can be tedious and time consuming, as a consequence, other tools such as DREAM3D^{TM} can be used to streamline the process. DREAM3D^{TM} reads output files directly from EBSD scans and performs alignment, data filtering and segmentation all in one step. It is useful for large dataset such as the serial sectioning data obtained using FIB coupled with EBSD.

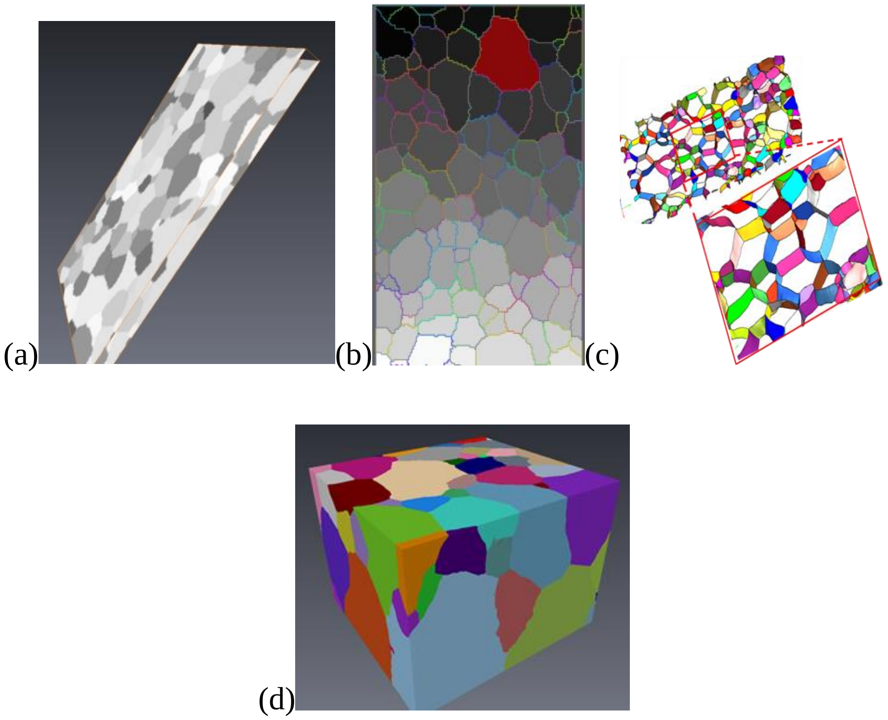

Figure 5-1: Examples of the Process for 3-D Microstructure Reconstruction: (a) Stacking Two Identical EBSD Maps (b) Labeling Grains in AVIZO^{TM} (c) GB Network Obtained from the Labels (d) 3-D Microstructure.

The reconstructed geometry files contain a surface mesh for GBs and geometry boundaries. The geometry needs to be meshed with 3-D elements using either AVIZO^{TM} or meshing software like Hypermesh^{TM} before they are exported to COMSOL^{TM} for simulations. One issue with meshing that is brought up from the 2-D simulation work published in [81], is the resolution of GBs. Grain boundary widths are very small compared to the grain size of the samples used here. Most theoretical works treat GBs as 0.5 to 1 nm thick [41], but the grains for a typical UO_2 sample are in the micrometer scale, which is three to four orders of magnitude larger than the typical GB width. This difference in size makes meshing the geometry very difficult, and as a consequence, many modeling works had to use thicker GBs or other approaches to reduce computational cost. The 2-D work in [81] used a GB thickness value of 1 μm, which deviates from the actual thickness, in order to resolve GBs using small elements. Even with the compromise, it still requires a large number of elements as shown in Figure 5-2. The large number of elements increases the computational cost significantly.

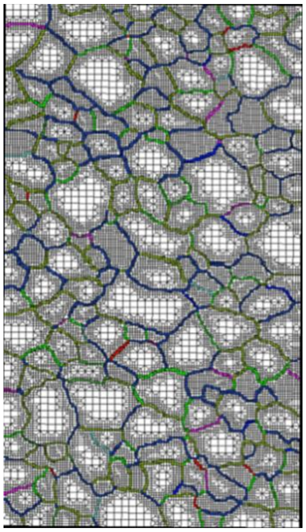

Figure 5-2: Meshed Geometry for the 2-D Simulation [81].

In 3-D, it is even harder to resolve the GBs as they often have significant 3-D curvatures and they are represented by 2-D surfaces. To avoid these issues, the GBs in the models developed here are meshed with 2-D elements that do not have a physical thickness value. The thickness term will be incorporated in the equations governing the behavior of these 2-D elements in the simulations. It is similar to the way that the analytical solution for GB diffusion uses a δD_{GB} term, as discussed in the Literature Review [51]. An example of a GB network meshed with 2-D elements is shown in Figure 5-3. This approach can significantly reduce the number of elements required to mesh the geometry and thus the computation cost. All the models created in this work are based on this approach.

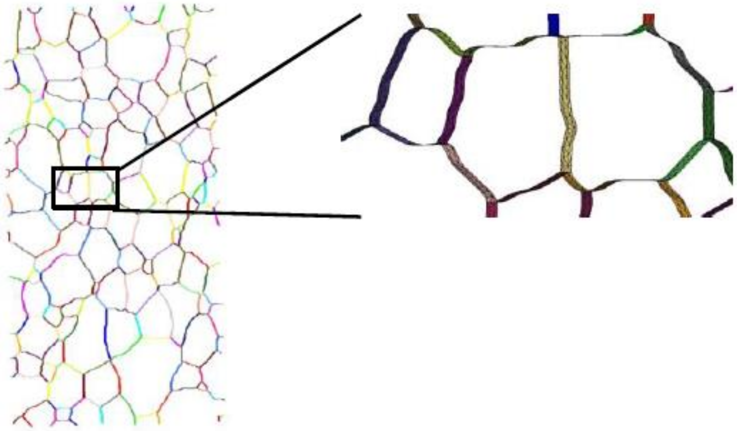

Figure 5-3: A GB Network Meshed with 2-D Elements.

5.1.2 Reconstructed 3-D Models

Many different models have been created in the past couple years from different samples. In general, the work began from the 2-D model referenced in [81] and found that heterogeneous GBs play a dominating role in the study of the percolation of fission products. The second model then constructed a GB network and conducted the simulation in 2.5-D, where the GBs are meshed with 2-D elements to solve the issue with GB thickness. For the three samples discussed in this work, the FIB and EBSD data are imported to DREAM3D^{TM} for pre-processing and segmentation. The segmented files are then exported to AVIZO^{TM} for interpolation, surface reconstruction and 3-D meshing. Each side of the reconstructed model is between 25-30 μm while the length is about 50 μm, 20 μm and 40μm for $UO_{2.0}$, $UO_{2.06}$ and $UO_{2.14}$, respectively. The actual size used for simulations is different to keep the size in all three dimensions similar in order to have a representative cubic volume.

Figure 5-4 shows the final microstructural models for $UO_{2.00}$, $UO_{2.06}$ and $UO_{2.14}$, meshed with tetrahedral elements. The mesh size is controlled to have finer elements in small grains and close to GBs, and larger elements for large grains to reduce the total number of elements required to solve the model.

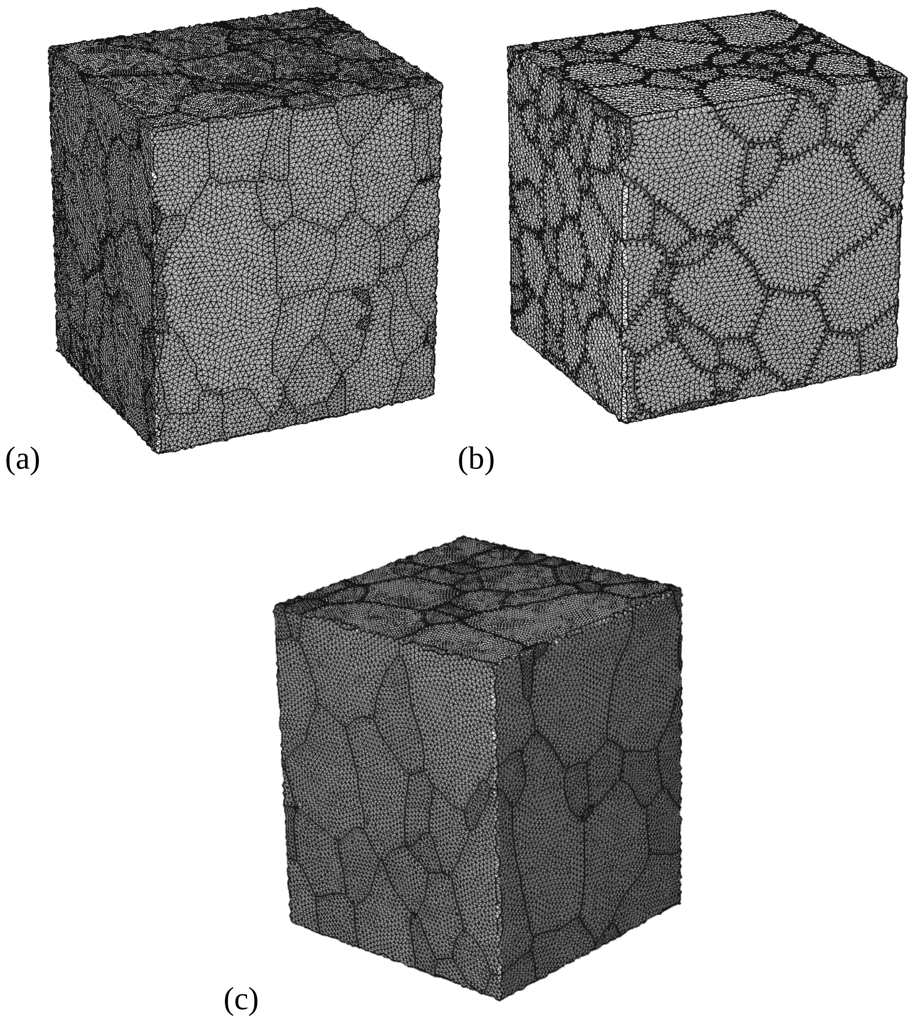
(a) (b)

(c)

Figure 5-4: Meshed Model for the Three Samples (a) $UO_{2.00}$ (b) $UO_{2.06}$ (c) $UO_{2.14}$.

The meshed models have different microstructural statistics from the whole reconstructed models as well as from the 2-D data. A summary of the statistics for the meshed models is listed in Table 5-1. The information includes average grain sizes, fraction of different GB types, dimensions of the models and the total elements required to mesh them. The GB types are defined following the work in [94], which defined low diffusivity GBs with misorientation angles below 30° and above 55°. The high angle GBs, which have misorientation angles between 30° and 55°, are assigned with a high diffusivity value. The low CSL GBs are also identified and assigned to the models as low diffusivity GBs. The EBSD slices provided information on these GBs, which are then assigned to the 3-D models by matching the reconstructed models to the 2-D data. With these GBs now represented in 3-D space, their total surface area can be measured and area fractions are calculated.

Table 5-1: Microstructural Data in 3-D for the Three Reconstructed and Meshed Stoichiometric Samples

Model	$UO_{2.0}$ (200grains)	$UO_{2.06}$ (248 grains)	$UO_{2.14}$ (196grains)
Average grain size (μm)	4.28	3.55	4.36
High angle GB fraction	0.734	0.716	0.657
Mid angle GB fraction	0.172	0.221	0.220
Low angle GB fraction	0.031	0.024	0.123
CSL GB fraction	0.063	0.039	
Dimensions (μm)	29 x 25 x 31	27 x 26 x 20	30 x 25 x 25
Number of element (million)	1.49	2.09	1.36

From the statistics of these three models, it is noticed that the average grain sizes for all three of them are smaller as compared with those from the whole reconstructed models presented in Chapter 4. The reduction in size is expected due to the fact that a larger fraction of grains are now cut off by the model boundaries. The grain size distributions for the three meshed microstructures are plotted in Figure 5-5. The $UO_{2.00}$ and $UO_{2.14}$ models have very similar distribution with a peak at 4 μm. The $UO_{2.06}$ model has smaller grains with a peak at about 3 μm. The overall model dimensions are similar with each side between 20 μm to 30 μm.

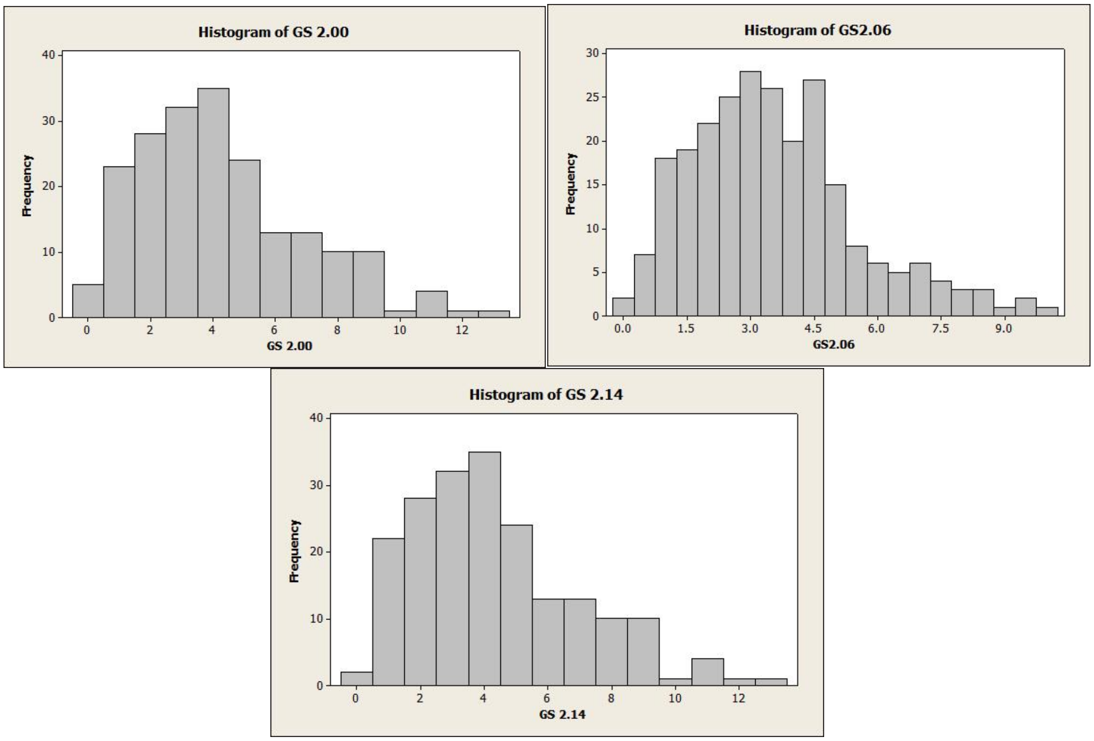

Figure 5-5: Grain Size Distributions for the Three Reconstructed and Meshed Models. The x-axis Has a Unit in μm

5.2 Analytical Approach

Once the finite element models are meshed and ready for simulation, work needs to be done to ensure the right equations are applied to the model. This section discusses the origins and the derivation of the equations applied to grain bulks, GBs and TJs to study the transport phenomena in the fuel microstructure.

5.2.1 Governing Equations

The transport mechanisms in UO_2 fuel pellets are complex because of the extreme environment, which has very high temperature gradients and irradiation damage. The dominating mechanisms change over time and thus need to be studied separately. At the beginning of fuel life, solid state diffusion is the dominating mechanism for FG transport, which is why diffusivities are obtained by measuring FGR from lightly irradiated samples [6]. The differential equation resulting from Fick's Law can be applied to study the problem. Similarly, heat transport via conduction can be studied using Fourier's Law. The resulting relationships are shown in Equation 5-1 and Equation 5-2, where *C* is concentration, *t* is time, *D* is diffusivity, *F* is FG generation rate, ρ is fuel density, C_p is heat capacity, *T* is temperature, *k* is thermal conductivity and *H* is heat generation rate. The equations may look simple enough, but the inter-connected physics can make the problem fairly complicated. First of all, the diffusion mechanism is a strong function of temperature. If there is a high temperature gradient in the model, then there will be significant changes on diffusivity across the model. The heat conduction and fission product diffusion equations are coupled one way given that the mass diffusivity is a function of temperature. It is also known that the thermal conductivity of GBs can change due to the accumulation of fission gases. The models can then be coupled both ways by including equations to capture these relationships.

$$\frac{\partial C}{\partial t} - \nabla(D\nabla C) = F \qquad \text{Equation 5-1}$$

$$\rho C_p \frac{\partial T}{\partial t} + \nabla(k\nabla T) = H \qquad \text{Equation 5-2}$$

5.2.2 Modeling Grain Boundary Diffusion

The work presented in this section shows the analytical derivation of the 2-D equations applied to GBs. As mentioned in the modeling procedures, the approach taken for the modeling work is to treat GBs with 2-D elements and triple junctions (TJs) with 1-

D elements in which the GB thickness and the TJ cross-sectional area can be incorporated in equations instead of trying to capture them with small 3-D elements. The governing relationships for different dimensionalities (1- and 2-D) can be derived from the standard 3-D diffusion equation, shown in Equation 5-1, with the FG concentration in the GBs is labeled with *C'* to differentiate from the concentration in the bulk. The equation in 2-D can be obtained by taking the average over the GB thickness. Assuming this thickness is parallel to the *z*-axis and that diffusivity is constant, one obtains Equation 5-3 below:

$$\frac{1}{\delta}\int_0^{\delta}\left(\frac{\partial C'}{\partial t} - D_{GB}\left(\frac{\partial^2 C'}{\partial x^2} + \frac{\partial^2 C'}{\partial y^2} + \frac{\partial^2 C'}{\partial z^2}\right) - F\right)dz = 0 \qquad \text{Equation 5-3}$$

where D_{entity} is the diffusivity of the entity, δ is the GB thickness and *F* is the source term for FPs, i.e., the volumetric generation rate.

Then, integrating over *z* once, the equation becomes

$$\frac{\partial \overline{C'}}{\partial t} - D_{GB}\left(\frac{\partial^2 \overline{C'}}{\partial x^2} + \frac{\partial^2 \overline{C'}}{\partial y^2}\right) - \frac{D_{GB}}{\delta}\left(\left.\frac{\partial C'}{\partial z}\right|_{z=\delta} - \left.\frac{\partial C'}{\partial z}\right|_{z=0}\right) - F = 0 \qquad \text{Equation 5-4}$$

Where

$$\overline{C'} = \frac{1}{\delta}\int_0^{\delta} C' dz \qquad \text{Equation 5-5}$$

Multiplying Equation 5-4 by the thickness δ, Equation 5-6 can be obtained below.

$$\delta\frac{\partial \overline{C'}}{\partial t} - \delta D_{GB}\left(\frac{\partial^2 \overline{C'}}{\partial x^2} + \frac{\partial^2 \overline{C'}}{\partial y^2}\right) - D_{GB}\left(\left.\frac{\partial C'}{\partial z}\right|_{z=\delta} - \left.\frac{\partial C'}{\partial z}\right|_{z=0}\right) - \delta F = 0 \qquad \text{Equation 5-6}$$

The term $D_{GB}\left(\frac{\partial C'}{\partial z}\Big|_{z=\delta} - \frac{\partial C'}{\partial z}\Big|_{z=0}\right)$ is nothing more than the net flux along the z direction between the grains and the GB. Taking advantage of the fact that fluxes perpendicular to an interface must be continuous [95], this term can be rewritten in terms of the flux from the grain bulk (j_{bulk}) as shown in Equation 5-7 below.

$$j_{bulk} = D_{GB}\left(\frac{\partial C'}{\partial z}\Big|_{z=\delta} - \frac{\partial C'}{\partial z}\Big|_{z=0}\right) = D_{bulk}\left(\frac{\partial C}{\partial z}\Big|_{z=\delta} - \frac{\partial C}{\partial z}\Big|_{z=0}\right) \qquad \text{Equation 5-7}$$

where the concentration gradients are now taken on the bulk of the grain, rather than on the GB [14]. Using this approach the flux term can be reflected in the grain bulk rather than the GB, which has no actual thickness. In addition, given that the value of D_{GB} is orders of magnitude higher than D_{bulk} and that the GB thickness δ is orders of magnitude smaller than the grain size of a typical UO_2 sample, a constant concentration is assumed across the GBs with the continuity in concentration enforced that at the bulk-GB interface, i.e., C'=C. Finally, the equation for the GB is given by:

$$\delta\frac{\partial C}{\partial t} - \delta D_{GB}\left(\frac{\partial^2 C}{\partial x^2} + \frac{\partial^2 C}{\partial y^2}\right) - j_{bulk} - \delta F = 0 \qquad \text{Equation 5-8}$$

This is quite similar to the equation used in [95], except that the net flux term has been neglected for the reasons discussed above. A similar approach can be followed for the TJ by integrating the diffusion equation for a TJ line with respect to both *y* and z direction, assuming that the cross-section of the TJ is perpendicular to *x*, to obtain Equation 5-9 below, with the flux term now representing the net flux in two directions perpendicular to the TJ from the GBs as shown in Equation 5-10

$$\delta^{2}\frac{\partial \mathrm{C}}{\partial \mathrm{t}} - \delta^{2}\mathrm{D}_{\mathrm{TJ}}\left(\frac{\partial^{2}\overline{\quad}\mathrm{C}}{\partial \mathrm{x}^{2}}\right) - \mathrm{j}_{GB} = \delta^{2}\mathrm{F} \qquad \text{Equation 5-9}$$

$$\mathrm{j}_{\mathrm{GB}} = \delta D_{GB}\left(\left.\frac{\partial \mathrm{C}'}{\partial \mathrm{z}}\right|_{\mathrm{z}=\delta} - \left.\frac{\partial \mathrm{C}'}{\partial \mathrm{z}}\right|_{\mathrm{z}=0} + \left.\frac{\partial \mathrm{C}'}{\partial \mathrm{y}}\right|_{\mathrm{z}=\delta} - \left.\frac{\partial \mathrm{C}'}{\partial \mathrm{y}}\right|_{\mathrm{z}=0}\right) \qquad \text{Equation 5-10}$$

The resulting equation is similar to what was obtained by Klinger [96] with slight differences due to the assumptions on the TJ cross-section geometry. . If the diffusivities are not constant, the equations can be written more generally for grain bulk, GB and TJ as:

$$\frac{\partial \mathrm{C}}{\partial \mathrm{t}} + \nabla(-\mathrm{D}_{\mathrm{bulk}}\nabla \mathrm{C}) = \mathrm{F} \qquad \text{Equation 5-11}$$

$$\frac{\partial C}{\partial t}\delta + \nabla(-\delta\, D_{GB}\nabla C) = \delta F + \mathrm{j}_{bulk} \qquad \text{Equation 5-12}$$

$$\frac{\partial C}{\partial t}\delta^{2} + \nabla\left(-\delta^{2} D_{TJ}\nabla C\right) = \delta^{2} F + \mathrm{j}_{GB} \qquad \text{Equation 5-13}$$

The three equations developed will be applied to study the transport behavior of FPs. It is known that the behavior of mass transport is a strong function of temperature. Moreover, the distribution of FPs can affect the heat transfer behavior. It is important to couple these equations to the temperature distribution in a fuel element, taking into account the effect of GB thermal resistance, which is affected by the FP concentration.

5.2.3 Grain Boundary Thermal Resistance

A similar approach can be taken to model the phenomenon known as GB thermal resistance, or Kapitza resistance. The basic concept of the Kapitza resistance was covered in the Literature Review. In order to model the temperature drop across a GB, a lower thermal conductivity needs to be applied to it. However, when 2-D elements are used for GBs with the thickness term incorporated in the equation, the drop in temperature also needs to be treated analytically. Similar to section 5.2.2, the heat conduction equation shown in Equation 5-2 can be integrated over GB thickness to obtain Equation 5-14. The difference in modeling the Kapitza resistance is that the $\delta k_{GB}\left(\frac{\partial^2\overline{T}}{\partial x^2}+\frac{\partial^2\overline{T}}{\partial y^2}\right)$ term can be eliminated due to the low GB thermal conductivity. At steady state with no heat generation at GBs, the only term left is $-k_{GB}\left(\left.\frac{\partial T}{\partial z}\right|_{z=\delta}-\left.\frac{\partial T}{\partial z}\right|_{z=0}\right)$, which is the GB thermal conductivity times the temperature gradient difference between top and bottom of a GB. The temperature gradient difference can be simplified as $(T_u - T_d)/\delta$, where T_u is the temperature at the upside and T_d is the temperature at the downside of a boundary, given that the GB thickness is small. Finally Equation 5-15 is obtained, and the heat flux coming from the grain bulk is translated to a temperature drop across the GB. The magnitude of the temperature drop depends only on the GB thermal conductivity and GB thickness.

$$\delta\rho C_p\frac{\partial\overline{T}}{\partial t}-\delta k_{GB}\left(\frac{\partial^2\overline{T}}{\partial x^2}+\frac{\partial^2\overline{T}}{\partial y^2}\right)-k_{GB}\left(\left.\frac{\partial T}{\partial z}\right|_{z=\delta}-\left.\frac{\partial T}{\partial z}\right|_{z=0}\right)-\delta H=0 \qquad \text{Equation 5-14}$$

$$-n\cdot(k_{bulk}\nabla T)=-\frac{k_{GB}}{\delta}(T_u-T_d) \qquad \text{Equation 5-15}$$

n: GB normal

Literature has also shown that the thermal conductivity at a GB is not a constant value. Bubbles that are mostly filled with Xe and Kr accumulate at GBs and can further reduce their thermal conductivity. Analytical derivations regarding this effect can be found in [28, 65, 80]. According to these works, the thermal conductivity of GBs can be expressed as $k_{GB}=\delta/R_k'$, where R_k' stands for the thermal resistance across a GB. The expression of R_k' follows Eq.8 from the work presented by Millet [80]. The expression for R_k', as shown in Equation 5-16, is a function of fission gas bubble radius (r_b), intrinsic GB resistance (R_k) and bubble coverage fraction (X_{GB}), which allows the resistivity value to increase with the bubble coverage. Assuming a bubble radius of 50 nm, GB resistance with a value of $1x10^{-8}$ [80], the bubble coverage fraction X_{GB}, which is a function of the number of gas atom per unit area, can be calculated using Equation 5-17 as suggested in [28, 74]. After taking into account all the relationships, the final thermal conductivity is roughly estimated to vary between 0.1 W/m/K, a GB conductivity value similar to that used in the literature [48], and 0.00552W/m/K, experimental value of Xe thermal conductivity [97], depending on the fission gas concentration in GBs. This approach couples thermal conductivity to the concentration of fission gases and allows the model to capture the variation in GB thermal conductivity caused by the difference in fission gas distribution.

$$\mathrm{R}_{\mathrm{k}}' = \mathrm{R}_{\mathrm{k}}\left[1 + \left(\mathrm{A}_3\mathrm{r}_{\mathrm{b}}^{\mathrm{A4}} + \mathrm{r}_{\mathrm{b}}\mathrm{R}_{\mathrm{k}}^{\mathrm{A2}}\right)\left(\mathrm{X}_{\mathrm{GB}}^{\mathrm{c}}\right)^{\mathrm{A1}}\right] \qquad \text{Equation 5-16}$$

$$\mathrm{X}_{\mathrm{GB}}^{\mathrm{c}} = \frac{3\mathrm{k}_{\mathrm{b}}\mathrm{T}}{4(2\gamma + \mathrm{r}_b\mathrm{P}_{\mathrm{ext}})\mathrm{f}(\theta)}\mathrm{N}_{\mathrm{GB}} \qquad \text{Equation 5-17}$$

Parameters Used:

A1=1.5; A2=-0.968; A3=9.8176; A4=0.0862, γ (surface tension) =0.626 J/m^2, P_{ext} = 10MPa; N_{GB}: number of FG atoms per GB area

$R_k=10^{-8}$ m^2K/W; r_b=50 nm

5.3 Simulation Parameters

The simulation parameters, including boundary conditions and material properties, need to be carefully defined for the simulations to reflect the actual reactor environment. The boundary conditions depend mainly on the type of study being done with the model. The applied values need to reflect the conditions of an operating fuel rod. These parameters, including concentration profile, FG generation rate and temperature profile need to be calculated based on the operating conditions of a reactor. On the other hand, the material properties for UO_2 mainly come from experimental data collected from published characterization work spanning several decades. Some material properties are well established, e.g., thermal conductivity, density and heat capacity, while some properties vary by orders of magnitude between different experiments, e.g., FG diffusivity. Other properties such as GB diffusivity and TJ diffusivity are difficult to measure and are thus scarce from the existing literature. The applied values will be based on suggestions from the open literature. As a consequence of large uncertainty in these parameters, a sensitivity analysis will be performed to quantify how much their variability affects the outcomes of the simulations. This section revisits data collected from literature review and uses them to derive and map out the simulation parameters.

5.3.1 Fission Gas Diffusivity

The diffusivities of FGs, mainly xenon, in a UO_2 matrix collected in the literature review are plotted in Figure 5-6 based on Table 2.1. The presented values account for only the intrinsic diffusion, and no irradiation effect is included. All the values follow an Arrhenius relationship, but with different diffusion coefficients and activation energies.

The upper and the lower bounds differ by 5 orders of magnitude or more. The value derived by Davies and Long [98] will be used for the simulation because it stays away from both the upper and lower extremes. Also, most of the FGR models and fuel performance codes also use the value by [98], which will allow easier comparison. A sensitivity analysis will also be conducted to examine the effect of the upper and lower bound values.

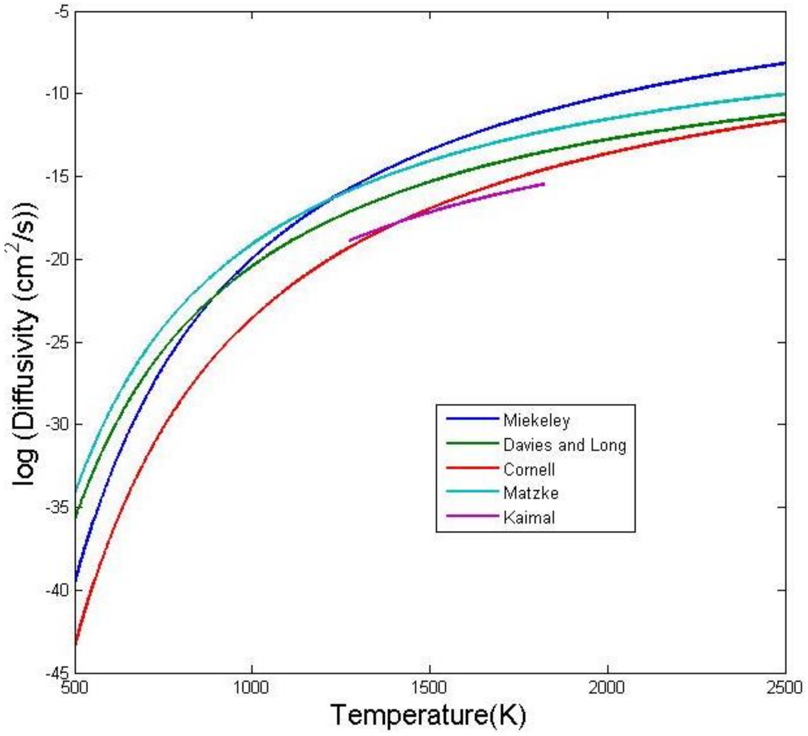

Figure 5-6: Fission Gas Diffusivities from Different Researchers (log D vs T).

It has been discussed that the stoichiometry of UO_{2+x} makes a large difference in the transport properties and needs to be considered in the analysis. It has also been proposed in many papers [6, 99] that the large deviation in FG diffusivity reported in experimental measurements is due to poor control of sample stoichiometry. However, experiments done to study the effect of stoichiometry on FG diffusion is scarce. The work done by Miekeley and Felix [25] is the most commonly referenced source that studies the effect of stoichiometry. Stoichiometric samples were fabricated under a carefully controlled annealing environment. All samples were irradiated to a burnup between 1 to 10 x 10^{15} fission/cm^3. $UO_{2\pm x}$ samples were then obtained by annealing in different environments and measuring the fractional release of xenon over time. The data were fitted with Arrhenius relationships and the results for diffusion coefficient and activation energy are listed in Table 5-2 and plotted in Figure 5-7. The deviation in diffusivity is significant at low temperature, and the effect diminishes at temperatures above 1500 K.

Table 5-2: Stoichiometry Effect on Xenon Diffusivity. Table Reproduced from [25].

Samples	Diffusion Coefficient and Activation Energy	Temperature Range
UO_{2-x}	$D_0=4x10^2$ to $1.6x10^3$ cm^2s^{-1} ; $\Delta H=6.0\pm0.1eV$	1400°C < T < 2200°C
$UO_{2.0}$	$D_0=5x10^{-2}$ to 5 cm^2s^{-1} ; $\Delta H=3.9\pm0.4eV$	950°C < T < 1700°C
UO_{2+x}	$D_0=1x10^{-8}$ to $1x10^{-4}$ cm^2s^-1; $\Delta H=1.7\pm0.4eV$	600°C < T < 1300°C

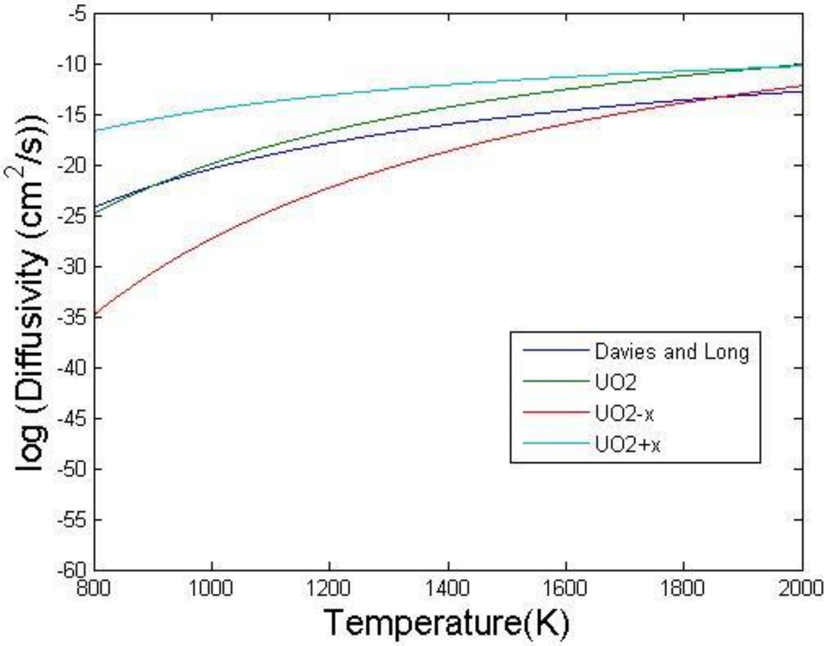

Figure 5-7: Stoichiometry Effect on Xe Diffusivity Based on Equations in [25]. The Results Are Compared with the Diffusivity from Davies and Long [98].

To address the discrepancy from literature about the stoichiometry effect on FG diffusivity, the work by [38], which showed that the diffusivity increases with the increase in *x* value in UO_{2+x}, is plotted in Figure 5-8, in comparison with Miekeley's work, which claimed that the diffusivity is fixed across a range of *x* values. The comparison shows that the work by Matzke has a closer match in the diffusivity value for $UO_{2.00}$ to the diffusivity of Davies and Long. Comparing with the $UO_{2.00}$ diffusivity derived by Matzke at 1400 K, it is an about 7 times larger for $UO_{2.02}$ and about 32 time larger for $UO_{2.12}$. The value for Miekeley's hyper-stoichiometric diffusivity is another 34 times larger than the one for $UO_{2.12}$ by Matzke. Given the fact that a more recent work [100] has also suggested the *x* dependence of the diffusivities, the three models will take the diffusivity values interpolated based Matzke's results. However, the high diffusivity value obtained by Miekeley will also be examined to observe the effect

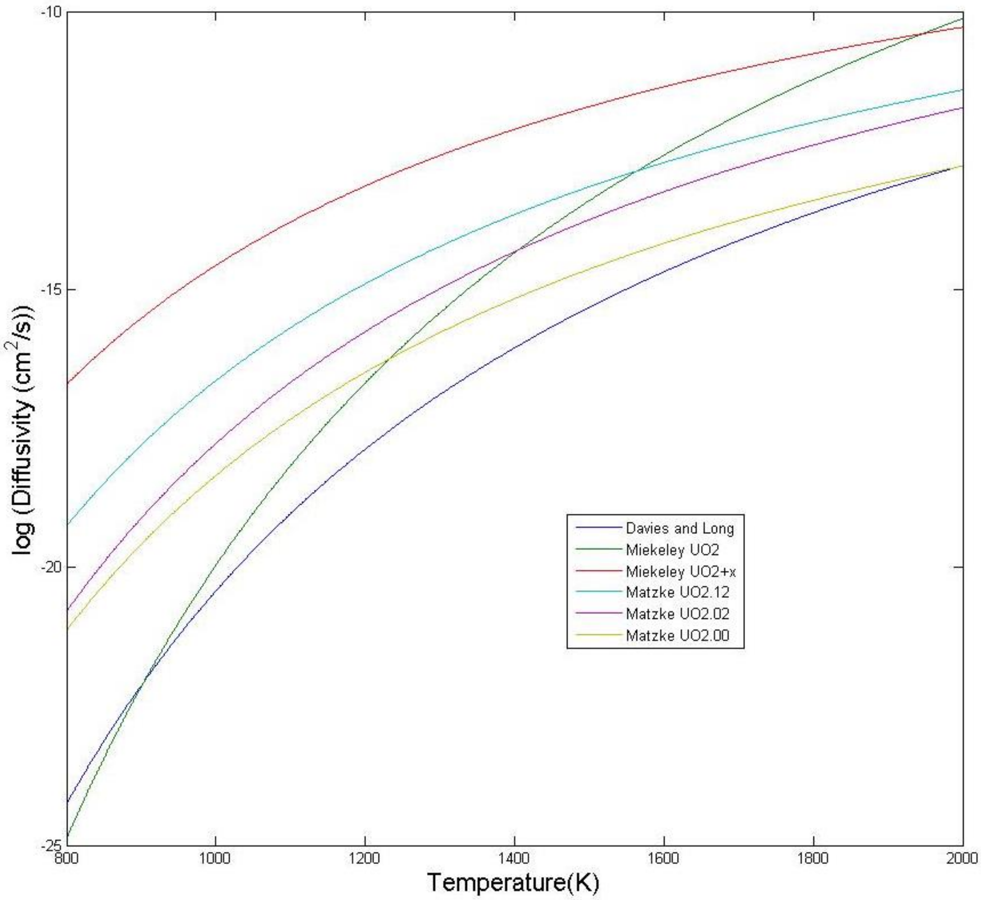

Figure 5-8: Stoichiometric Effect on Xenon Diffusivity Measured by Matzke (Plot Reproduced from [38]), Comparing with Miekeley's Work [25].

5.3.2 Grain Boundary Diffusivity and Effective Grain Boundary Diffusion

Although GBs play an important role in the study of FGR, experimental work to study GB diffusion or the effect of heterogeneous GB properties is scarce. Most of the available data of FG diffusion in UO_2 GBs are based on calculations. Olander [34] calculated two different diffusivity values by fitting 5 data point for Xe fractional release using the bulk diffusion measurements by Davies and Long [101] and Matzke [33] along with his developed model to obtain two different GB diffusivities, shown in Equation 5-18 and Equation 5-19, respectively. In addition, Kogai [102] modified the work by Reynolds [103] on uranium vacancy diffusion and applied it as gas atom diffusion in GBs in his model on FGR (Equation 5-20). Govers et al. [104] conducted molecular dynamic simulations in a polycrystalline UO_2 model and calculated the bulk and GB diffusion of oxygen, uranium and xenon. The Arrhenius parameters were obtained for each of them with the assumption that xenon diffusion is governed by uranium vacancy diffusion (Equation 5-21). The abovementioned GB diffusivities are plotted in Figure 5-9 along with the bulk diffusivity value of Davies and Long for comparison. In general, all the GB diffusivities are larger than bulk diffusivity by at least 5 orders of magnitude, and the differences become smaller as temperature increases. It seems more reasonable to apply Olander's work because the fractional release data used is based on lightly irradiated samples so that the effect of microstructure reconstruction and bubble coalescence can be ignored. When the diffusivity value from Davies and Long is used, the corresponding GB diffusivity (Olander 1) will be applied to the GB diffusivity. Again, sensitivity analysis will need to be conducted given the large discrepancy found in the literature.

Olander1: [34]

$$D_{gb1}=9\times10^{-8}\exp\left(\frac{-92\text{kJ/mol}}{RT}\right)\ \text{cm}^2/\text{s} \qquad \text{Equation 5-18}$$

Olander2: [34]

$$D_{gb2}=1.3\times10^{-3}\exp\left(\frac{-272\text{kJ/mol}}{RT}\right)\ \text{cm}^2/\text{s} \qquad \text{Equation 5-19}$$

Kogai: [102]

$$D_{gb3}=6.9\times\exp\left(\frac{-322\text{kJ/mol}}{RT}\right)\ \text{cm}^2/\text{s} \qquad \text{Equation 5-20}$$

Govers: [104] $$D_{gb4}=3.5\times10^{-5}\exp\left(\frac{-0.74\mathrm{eV}}{k_bT}\right)\ \mathrm{cm}^2/\mathrm{s} \qquad \text{Equation 5-21}$$

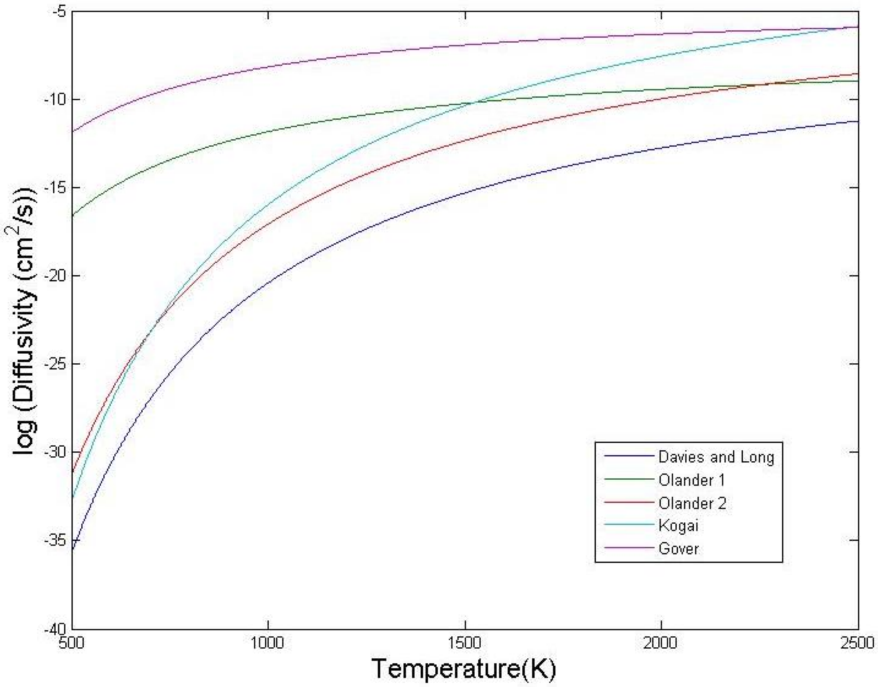

Figure 5-9: Fission Gas Diffusivity in the bulk (Davies and Long only) and in Grain Boundaries. Plots Based on the Equations Derived in [34, 102, 104].

In addition to GB diffusion, variation in GB properties based on their misorientation angle and CSL obtained from the characterization results can be applied to the model to study the effect of heterogeneous GB properties. In Figure 5-10, experimental work in metals shows that the diffusivity increases with the increase of misorientation angle and peaks at about 45° due to the symmetry of the cubic system [105]. Using the chart as a reference, GB diffusivities can be divided into three groups based on the misorientation angles: low angle GB, mid angle GB and high angle GB. The three groups of GBs can be identified in the 3-D models and assigned with three different diffusivity levels: D_{bulk}, D_{low} and D_{high}. The CSL GBs are grouped into the bulk diffusivity regime with Σ values ranging from 3 to 11 as they are the most commonly found to have lower free energy. The higher sigma values are not considered in this model because they only account for a small proportion and the differences in GB energy are not as significant as those for low Σ GBs. The combination of characterization and 3-D modeling techniques made it possible to incorporate the effect of heterogeneous GB properties in the study of FP transport.

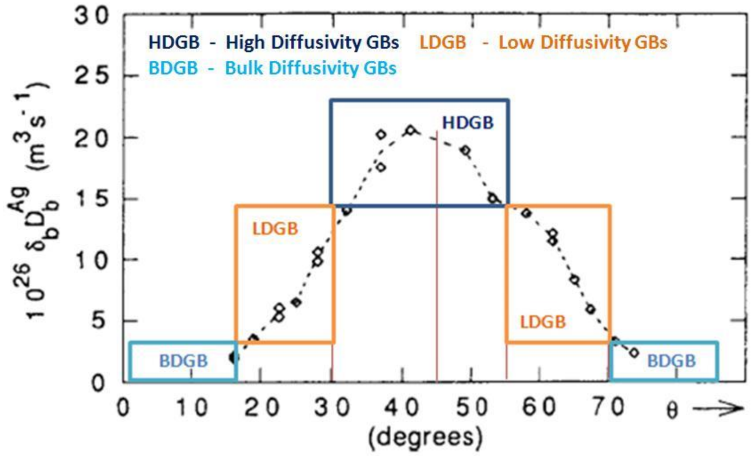

Figure 5-10: Grain Boundary Properties and Their Relationship to Misorientation Angles [105].

5.3.3 Heat and Mass Generation Rate

The generation rates of heat and FGs are important parameters that are needed to calculate the concentration and temperature profiles across the radius of a nuclear fuel pellet. Although variations in neutron flux exist at different locations in a reactor and at different radial positions in a pellet that will affect heat and mass generation rates, which are both dependent on fission rates, a simplified calculation assuming average behavior can provide a reasonable estimation [106]. From the thermal performance of the fuel, the fission gas generation rate can be calculated by finding out the number of fission events needed to sustain the heat generation, assuming all the fission energy is dissipated in the form of heat. A typical LWR can have a linear power density up to 400 W/cm under normal operating conditions [10]. The volumetric heat generation is calculated by dividing the linear heat density by the pellet cross sectional area, assuming a 1 cm diameter pellet. The fission gases generation rate can then be approximated assuming 25% of stable fission gases (Xe and Kr) are generated from fission events [6] and that each fission event generate 200 MeV of energy. The volumetric heat generation is calculated to be 509 MW/m^3. The number of fission events required to generate such power is then calculated to be 1.39x10^{13} fission/m^{3}s, and the number of stable FG is estimated to be 3.48 x 10^{12} FG generated per cubic meter per second, which is 5.78x10^{-6} mole of FG/m^{3}s.

5.3.4 Temperature Profile

Temperature profiles along the radius of the fuel pellet can also be calculated based on the volumetric heat generation calculated for the power density specified above. Plug the heat generation term into Equation 5-2, convert it into cylindrical coordinates to fit the shape of a pellet, and calculate for the steady state. The equation becomes Equation 5-22 shown below. With a little calculation, the equation can be simplified to Equation 5-23. Note that the thermal conductivity term is expressed as a function of the temperature, and as mentioned in previous chapters, the thermal conductivity vary somewhat over the large temperature range that is present in a fuel pellet. On the other hand, the temperature, which is a function of radius, is the very unknown we are trying to solve. These relationships complicate the problem.

In order to get a reasonable temperature profile, an iterative method is used. It is firstly assumed that there is a constant thermal conductivity, $\bar{k}$, which represents the average thermal conductivity across the radius. Using Equation 5-24 and the boundary conditions shown in Equation 5-25 and Equation 5-26, the temperature difference between centerline and the surface of a pellet can be calculated using Equation 5-27. The temperature difference can then be used to calculate $\bar{k}$ using Equation 5-28, knowing the relationship between thermal conductivity and temperature from the literature review (Chapter 2). The calculated $\bar{k}$ value is then plugged back into Equation 5-27 to get the new temperature difference value. The steps are repeated until the calculated temperature differences match. Finally, the temperature profile can be expressed using Equation 5-29.

$$\frac{1}{r}\frac{d}{dr}\left(rk(T)\frac{dT}{dr}\right)+H=0$$

Equation 5-22

$$k(T)\frac{dT}{dr}=-\frac{1}{2}Hr^2$$

Equation 5-23

If $k(T) = \bar{k}$

$$T(r)=-\frac{1}{4}\frac{Hr^2}{\bar{k}}$$

Equation 5-24

Boundary condition: at r=R $T\ (R) = T_s = 800K$ Equation 5-25

Boundary condition: at r=0 $T(0) = T_0$ Equation 5-26

$$T_0-T_s=\frac{1}{4}\frac{HR^2}{\bar{k}}$$

Equation 5-27

$$\bar{k}=\frac{\int_{T_s}^{T_0} k(T)dT}{T_0\text{-}T_s} \qquad \text{Equation 5-28}$$

$$T = T_s + \frac{1}{4}\frac{HR^2}{\bar{k}}(1 - \frac{r^2}{R^2}) \qquad \text{Equation 5-29}$$

The obtained temperature profile is plotted in Figure 5-11. As expected, the temperature profile has a parabolic shape with the highest temperature at the center of the pellet at around 1950 K. Note that the calculation of the temperature profile is to generate reference temperatures that can represent the thermal environment in a fuel pellet for the use of multi-physics simulations. The calculated values should be representative of an actual reactor environment, but should not be always held as completely accurate. The actual temperature profile can vary depending on many factors. For example, linear power densities of a reactor change depending on operating conditions and can directly affect the temperature. Other factors, such as the position of the pellet inside a fuel rod, the position of the fuel rod inside the reactor core, the actual power history and the coolant condition can all make a difference in the temperature profile. Moreover, material properties would change with microstructure as well as the increase of burnup and further impact the temperature of a fuel pellet. The calculated profile is for the simulation of normal operation conditions at low burnups.

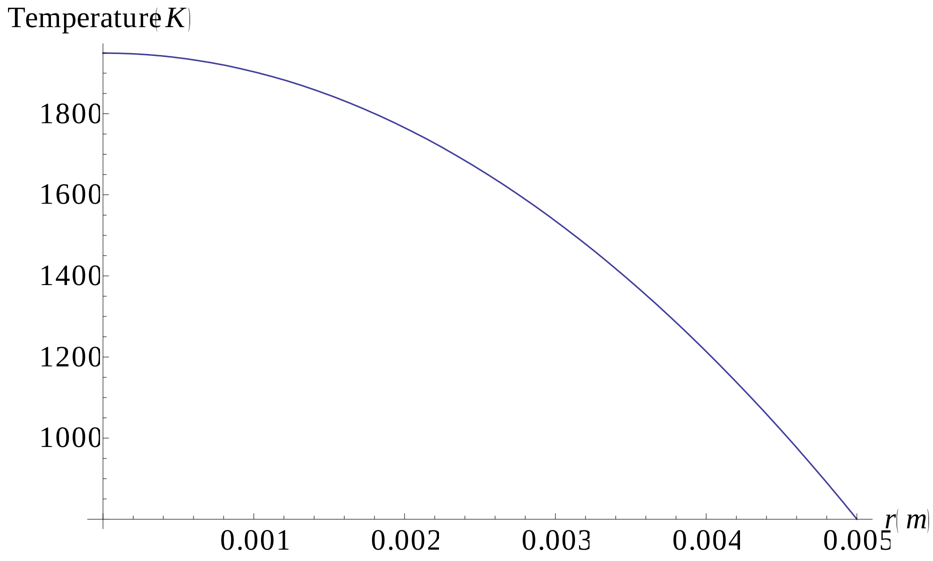

Figure 5-11: Temperature Profile across the Radius of a Fuel Pellet.

5.3.5 Concentration Profile

Theoretically the concentration profile can also be derived from Fick's first law of mass (Equation 5-1) in a similar fashion to that used to obtain the temperature profile in the last section. However, for an actual fuel pellet, other mechanisms such as microstructure reconstruction and crack formation greatly alter the FGR behavior. The simple solid state diffusion cannot depict the FG distribution along the whole radius. It can, however, be used to calculate local profile next to a spherical sink [6] as illustrated in Figure 5-12.

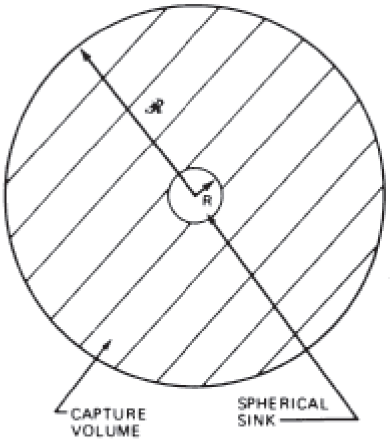

Figure 5-12: Spherical Sink in a Fuel Pellet for Calculating the Concentration Profile [6].

To calculate the concentration profile next to a sink, The FG diffusivity, as previously discussed, follows an Arrhenius temperature dependence. The partial differential equation for cylindrical geometry has the form expressed in Equation 5-30, where *F* is the volumetric fission gas generation rate. Equation 5-30 can be simplified by taking an integral over *r*. Assume no mass flux at the outer boundary, which is the effective limit of the sink, Equation 5-31 can be obtained. Integrating Equation 5-31 analytically becomes more complicated than solving the temperature profile because the diffusivity *D* is a function of temperature and thus a function of radius. Note that T is function of position given by the expression obtained in the previous section. Substituting the temperature profile obtained from Equation 5-29 into the diffusivity term, we get Equation 5-32. The last expression was solved numerically using Mathematica^{TM} with the derived heat and mass generation parameters. The final solution is plotted in Figure 5-13.

$$\frac{1}{r}\frac{d}{dr}\left(rD\frac{dC}{dr}\right)+F=0 \qquad \text{Equation 5-30}$$

$$\frac{dC}{dr}=\frac{-Fr}{2D}$$ Equation 5-31

$$\frac{dC}{dr}=\frac{-Fr}{2D_0}\exp\left\{\frac{Q}{R^*\left[T_s+\frac{1}{4}\frac{HR_0^2}{\bar{k}}\left(1-\frac{r^2}{R_0^2}\right)\right]}\right\}$$ Equation 5-32

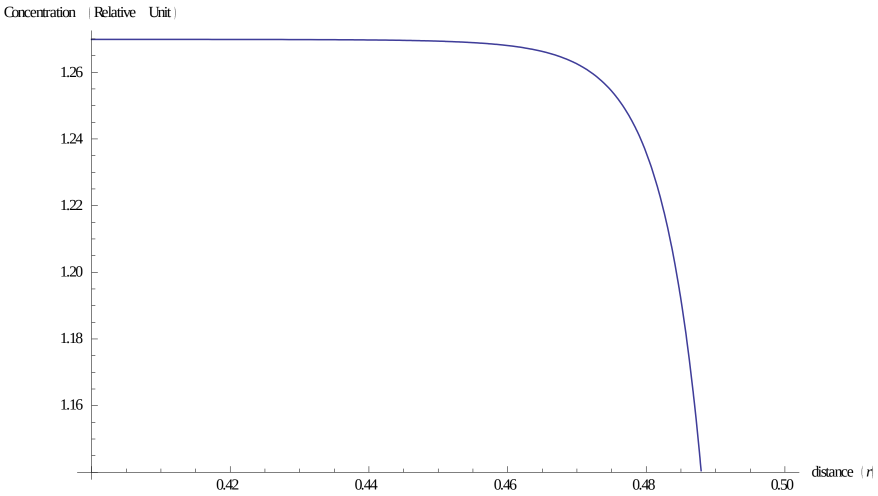

Figure 5-13: Concentration Profile close to a Spherical Sink.

As abovementioned, unlike temperature profile, the concentration profile across the radius of a fuel pellet cannot be calculated by solving the partial differential equation across the radius due to crack formation and microstructural reconstruction. Experimental work [107] has been done to measure the retained fission gases using electron probe micro analysis (EPMA). The concentration of xenon, as shown in Figure 5-14, is the lowest close to the center and increases with increase in radius. This is due to the fact that cracks open up at an early stage of fuel life, and the FG in high temperature region has a diffusivity value orders of magnitude higher than the cold region. The FGs can transport to the open space a lot faster in the hot region. The behavior can be simulated using finite element method by making a wedge to represent a section of a cylindrical pellet as shown in Figure 5-15a. It is assumed that the wedge is sandwiched between two radial cracks, which are reflected by the zero concentration boundary condition. The model is assigned with a heat generation term and a fission product generation term derived in section 5.3.3. The two sides are kept insulated for heat transfer. At steady state, the radial concentration profile is plotted in Figure 5-15b, which showed a similar trend as the experimental work. The middle flat region in Figure 5-14 that is not captured in the simulation is likely the coarse grain region that has a different microstructure from the center of the fuel.

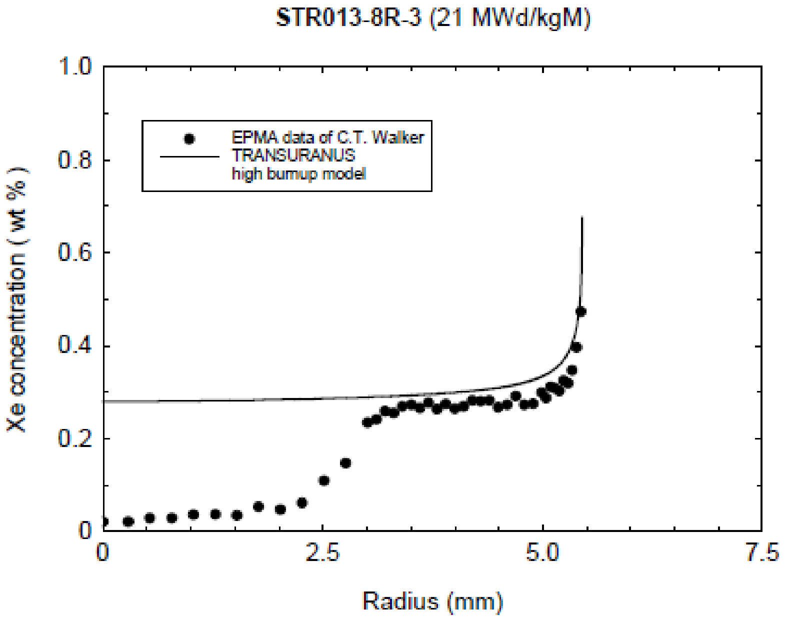

Figure 5-14: Xenon Concentration across the Radius of a UO_2 Fuel Pellet that Was Irradiated to about 2% Burnup [107].

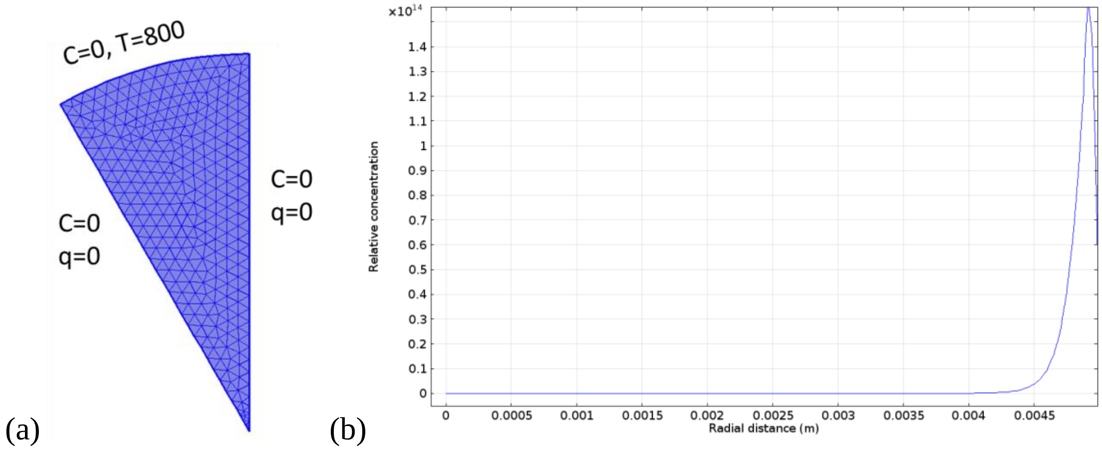

Figure 5-15: (a) A Finite Element Model that Simulates a Section of a Cylindrical Fuel Pellet Sandwiched between Two Radial Cracks; *C*: Concentration, *T*:Ttemperature (K), *q*: Heat Flux. (b) The Obtained Radial Concentration Profile.

The study has demonstrated that the concentration gradient does not necessary follow the temperature gradient, which goes along the radial direction of a pellet. The FG concentration increases with the increase in radius and thus has an opposite gradient from the temperature gradient with a highest value at the region close to the edge. However, concentration gradient can also be in the same direction as the temperature gradient when a spherical sink or pore is present. Both cases will be investigated in the simulation work.

5.3.6 Boundary Conditions

The derived temperature and concentration profiles are meant to represent a typical environment in a LWR. The values will be applied to finite element models as reference boundary conditions to mimic different environment in a fuel pellet. In the simulations to be covered in the next chapter, boundary conditions are generally set up by applying fixed concentrations and temperatures on the top and bottom boundaries of the geometry while keeping the sides insulated to make it a macroscopic 1-D problem (Figure 5-16). For some cases, a flux term will be applied to one boundary to drive the transport of heat or mass instead of applying a fixed gradient. In addition, the calculated rates of heat and FG generation can be applied directly to the bulk to capture the behavior at the beginning of fuel life.

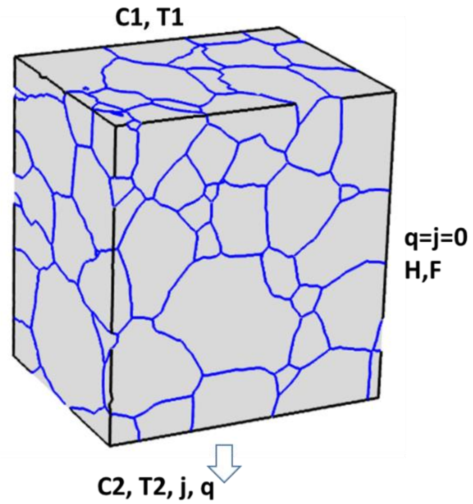

Figure 5-16: Schematic of Boundary Conditions Set-up. *T*: Temperature, *C*: Concentration, *j*: Mass Flux, *q*: Heat Flux, *H*: Heat Generation rate, *F*: FG Generation Rate

5.3.7 Effective Grain Boundary Diffusivity

Fission gas bubbles are usually larger in the GBs than in the grain bulk. Figure 5-17a shows bubbles distributing across the GBs with an area fraction of about 24%. The consensus is that FGs diffuse to GBs and accumulate in these bubbles, which grow and becomes interconnected. It is also known that the presence and the distribution of the inter-granular bubbles behave like traps and will affect the diffusion along GBs. It is desired to develop a homogenized model for GB diffusion taking into account the effects of the bubbles on transport mechanisms. The model should represent GB with bubbles before coalescence takes place.

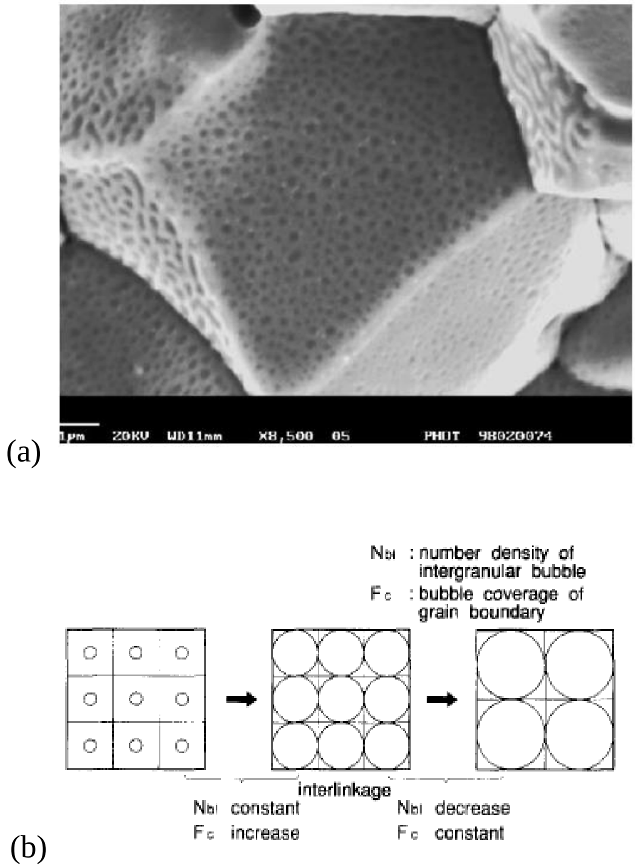

Figure 5-17: (a) A Fractograph Showing FG Bubbles at GB for a UO_2 Sample Irradiated to 1.3% Followed by a Heat Treatment [108] (b) Schematic to Illustrate the Relationship between Bubble Size and Bubble Density [102].

A simple finite element model is developed to capture the effective diffusivity at an instance of bubble growth. According to the experimental work by Kashibe and Une [109], GB bubble number density usually remains a constant until coalescence occurs as illustrated in Figure 5-17b. As a result, the work begins by using a fixed bubble density of

10^{12} bubbles/ m^2, a value typically observed at a GB [102]. A GB plane 10 μm by 10 μm, which contain 100 bubbles of 0.1 μm radius, as shown in Figure 5-18, is generated. The bubbles radius is increased by 0.1 μm until the bubbles touch at 0.5 μm, and the bubble coverage changes from 0.03 to 0.79. The analytical work about FG trapping from literatures usually includes a mass rate term as shown in Equation 5-33, which includes a trapping term and a resolution term. The equation is applied and solved for spherical grain models with the trapping probably calculated as a function of number of bubbles, diffusivity and bubble radius. The work presented here is done at a smaller scale where each bubble is treated separately. A similar approach is used by assigning the bubble surface with a trapping flux that is equal to the GB diffusional flux of the FP. The resolution effect, which depends on the reactor operating condition, is varied to cancel the trapping effect by 30 to 100%. In another word, the trapping flux is set to be 0 to 70% of the GB diffusional flux.

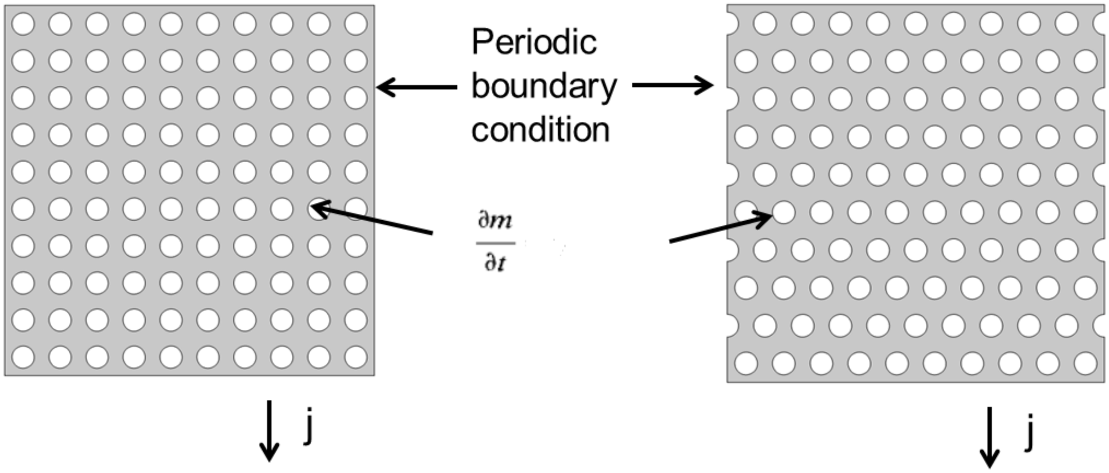

Figure 5-18: Square and Hexagonal Bubble Distribution in a 10 μm by 10 μm Area GB for Effective GB Diffusivity Calculation.

$$\frac{dm}{dt} = gc - bm \qquad \text{Equation 5-33}$$

g: trapping parameter; *b*: resolution parameter; c: number of fission gas atom in solid; *m*: number of fission gas atom in bubble.

The simulation is conducted at $T = 1400$ K. The effective diffusivities can be calculated by applying a concentration gradient and measuring the average flux at the bottom boundary. Periodic boundary conditions are applied to the side boundaries to eliminate the edge effect. A normalized concentration gradient is applied along the vertical direction. The ratio of the flux and the gradient is the effective diffusivity according to Fick's Law ($D_{eff} = -j/\nabla C$). With a series of simulations, the relationship between the effective diffusivity and bubble sizes can be obtained for different trapping conditions. Two types of bubble distributions, square and hexagonal as shown in Figure 5-18, are studied.

The obtained results are plotted in Figure 5-19. A general trend observed as expected is the decrease in effective diffusivity with the increase in bubble radius, which is basically bubble coverage. When no trapping is taking place, i.e., the trapping rate is the same as the resolution rate, the decrease in diffusivity is less than one order of magnitude. The trend is consistent until the bubble size reaches 0.50 µm, at which size the bubbles touch with their neighbors and results in a higher drop in diffusivity. Bubble coalescence usually takes place before the bubbles can reach the size [110]. The decrease in effective diffusivity starts to become very significant when the trapping effect kicks in. The trapping can reduce the GB diffusion by over 10 orders of magnitude given enough bubble size and little resolution effect. It was also found that the hexagonal bubble distribution hinders the diffusion more than square distribution, and the effect is only significant at trapping probabilities of 30% or higher. The decrease in effective diffusivity will be calculated as a function of GB bubble coverage and applied to the GB diffusivity term used in the microstructurally explicit models.

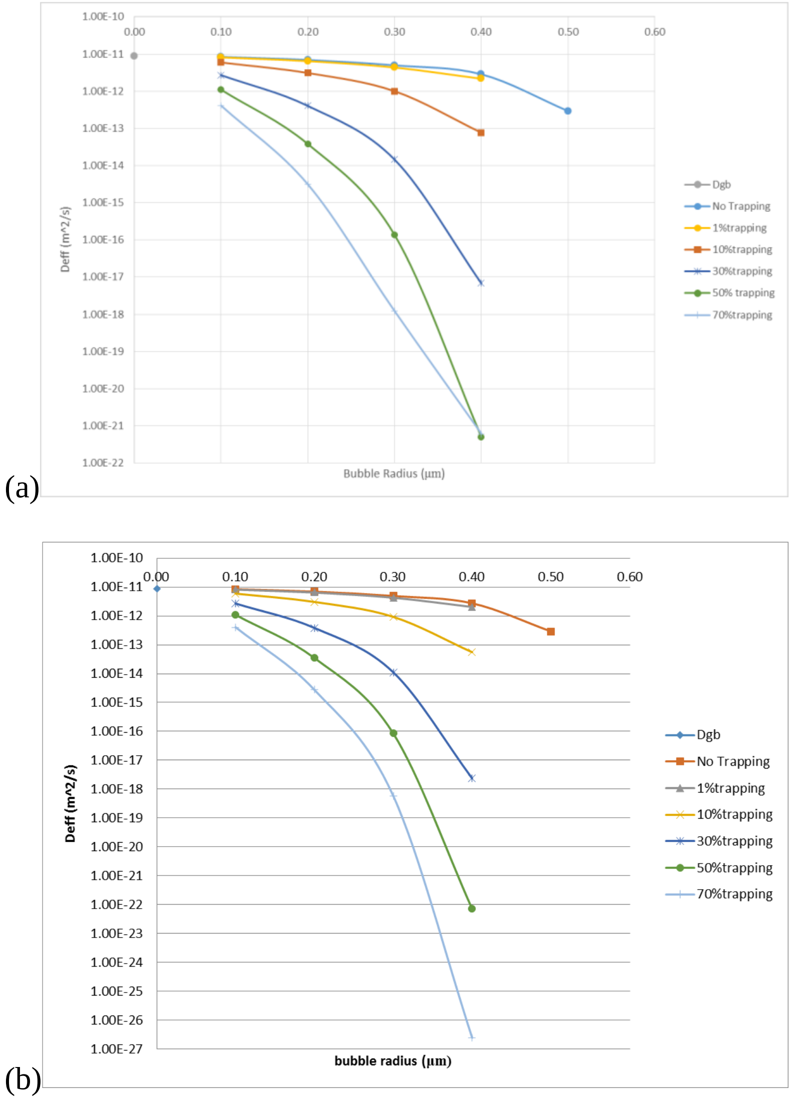

Figure 5-19: Effective GB Diffusivity for Both (a) Square and (b) Hexagonal Bubble Distribution as Different Bubble Radius.

To summarize, this chapter described the detail of the development of the microstructurally explicit model, which will be used to conduct finite element simulation of the transport mechanisms of nuclear fuels. The parameters required for such simulation are reviewed and calculated based on typical reactor conditions. The equations for different physics, such as GB diffusion, heat conduction and Kapitza resistance, are studied and derived for the simulations. The different concentration and temperature profiles obtained in this chapter will provide references to the boundary conditions applied for different scenarios in the simulations. The large spread in certain experimental parameters will also be followed up with sensitivity analysis in the next chapter.

6. SIMULATION RESULTS AND DISCUSSION

The simulations described in this chapter build up from simple models that contain two grains and one grain boundary (GB), i.e., bicrystals models, to full polycrystalline microstructures. The bicrystals models are used to verify that 2-D GB elements are appropriate to simulate GB diffusion as well as GB thermal resistance. The simulation results for reconstructed polycrystalline models allow studying the effect of different material and microstructural parameters. Finally, multiphysics simulations that take into account multiple effects are presented along with sensitivity studies to account for effects of the uncertainty on key material parameters.

6.1 Bicrystal Model Verification

Bicrystal models are used to verify the analytical derivations shown in the previous chapter that allows treating GBs with 2-D elements and triple junctions (TJs) with 1-D elements due to their small thicknesses compared to grain bulks. This section illustrates that the approach can be used to model GB diffusion, triple junction (TJ) diffusion as well as GB thermal resistance.

6.1.1 Grain Boundary Diffusion Verification

In order to verify that the equations developed in the previous chapter can be used to model GBs with 2-D elements and provide the same results as modeling them with 3-D elements, a bicrystal simulation was conducted. The geometry of the bicrystal model consists of two grains and one GB. The benefit of modeling GBs with 2-D elements is firstly illustrated with two bicrystal models, one where the GB is meshed with 3-D elements, like the grain bulk, and another where the GB is meshed with 2-D elements, while keeping 3-D elements for the bulk. The GB thickness (δ) is set to be 0.1 μm, and the meshes are generated in COMSOL$^{\text{TM}}$, which automatically decides the mesh size based on the smallest edge length. From Figure 6-1, it can be seen that the model that meshed the GB with 3-D element requires a lot more elements (63,401 elements) compared with the 2-D case (7,720 elements) due to the small δ. Note that the ratio between GB thickness and the width of the grains is only two orders of magnitude in this case. The actual number of elements needed to resolve GBs a few nanometers thick in a microstructure with a grain size of a few micrometers would be even higher.

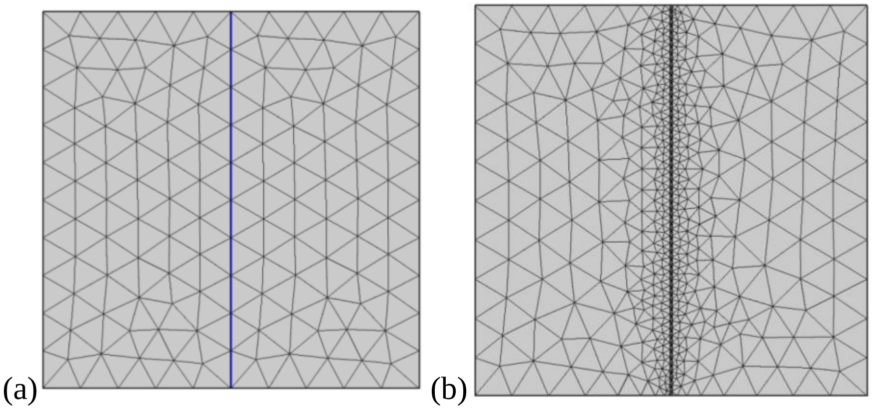

Figure 6-1: Bicrystal Models with GB Meshed with (a) 2-D Elements (b) 3-D Elements.

To verify the results of GB diffusion using the two models shown above, boundary conditions are applied to give a concentration gradient along the vertical direction, parallel to the GB plane, while keeping the sides insulated. The GB diffusivity is set to be 5 orders of magnitude higher than the grain bulk, and the GB thickness, δ, in the equation for 2-D GB elements takes the same value used for the 3-D GB. The unsteady simulation was conducted up to a time when a fair amount of diffusion along the GB can be observed. The concentration profiles for the 2-D and 3-D GB models are shown in Figure 6-2(a) and (b), respectively. At the same time step, it appears that the two simulations have the same concentration profile. To better compare the results, a line profile was plotted horizontally across the GB, 5 μm away from the tope surface, as shown in Figure 6-2c. The two lines are basically identical except that the GB thickness is not present in the 2-D case. The same approach can be applied to model TJs by assigning the equation developed for 1-D elements to the edges of the model. The TJs can then also act as fast diffusions paths as shown in Figure 6-3.

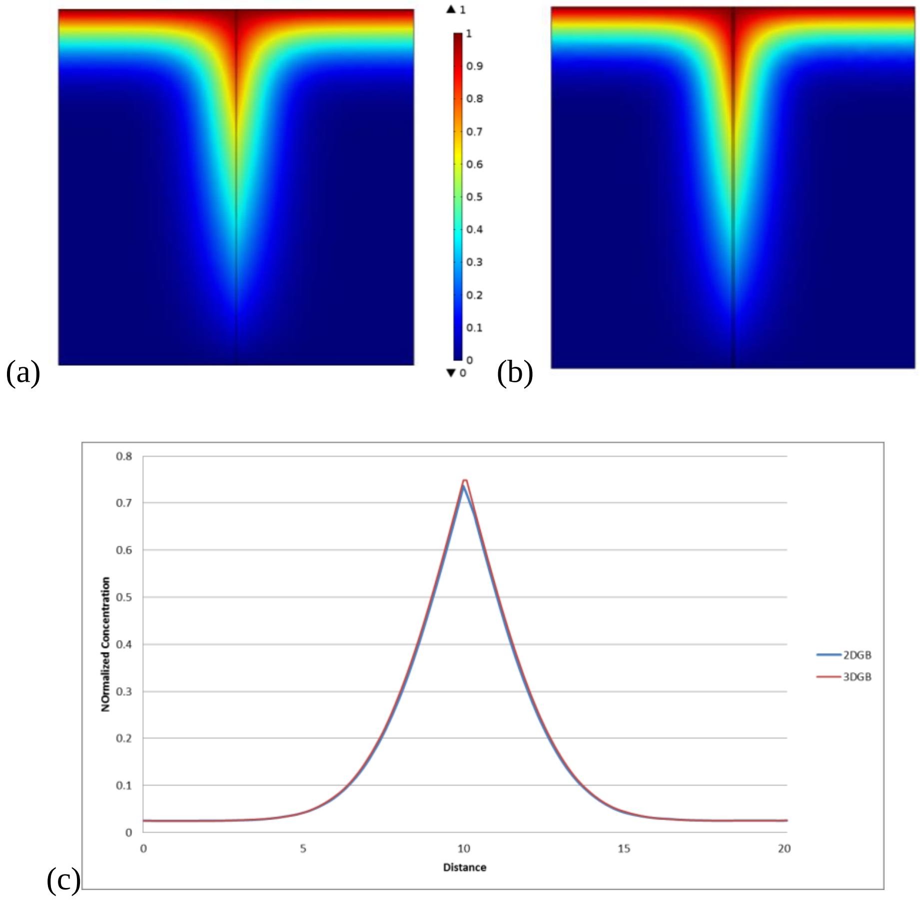

Figure 6-2: The Concentration Profile for Bicrystal Model with a GB Treated as (a) 2-D (b) 3-D (c) Concentration Profiles across the GBs for both models.

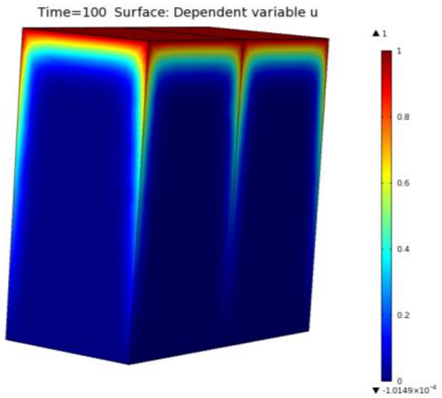

Figure 6-3: Modeling Diffusion along TJs using 1-D edge Elements.

6.1.2 Grain Boundary Thermal Resistance: Bicrystal Verification

Another phenomenon that is commonly observed in GBs is GB thermal resistance, also known as the Kapitza resistance. In a fashion similar to the GB diffusion approach shown in the last section, the idea here is to illustrate that the temperature drop across a GB can be captured by 2-D elements. The theory for Kapitza resistance was discussed in the literature review, and the analytical equations were developed in Chapter 5. By applying Equation 6-1, the thickness of a GB is incorporated into the appropriate equation and the heat flux from the grain bulk leads to a temperature drop across the GB. Note that the GB conductivity is dependent on the GB resistivity term in Equation 5-16, which is a function of the fraction of the GB covered with FG bubbles. The fractional coverage term is a function of FG concentration based on Equation 5-17. In other words, the temperature distribution is now dependent on FG concentration.

$$-\mathrm{n} \cdot (\mathrm{k}_{bulk} \nabla \mathrm{T}) = -\frac{\mathrm{k}_{GB}}{d_s}(T_u - T_d) \qquad \text{Equation 6-1}$$

The boundary conditions are applied as shown in Figure 6-4a, where a normalized concentration gradient is imposed from top to bottom and a temperature gradient is applied normal to the concentration gradient to see the effect of the Kapitza resistance. For this run, the concentration is normalized such that *C1* is 1 and *C2* is 0. Temperature *T1* is set to be 800 K at the left boundary with the outward heat flux *q* set to be 100 MW/m^2 at the right boundary, conditions that follow the work done in [48] for comparison. The thermal conductivity of the GB has an initial value of 0.1 W/mK and decreases with the increase in FG concentration. The maximum concentration in the simulation is normalized to have the maximum GB coverage fraction of about 0.5, a typically observed value from experimental work. After solving the model to a steady state, the temperature profiles across the top (high concentration) and bottom (low concentration) of the model are shown in Figure 6-4b.

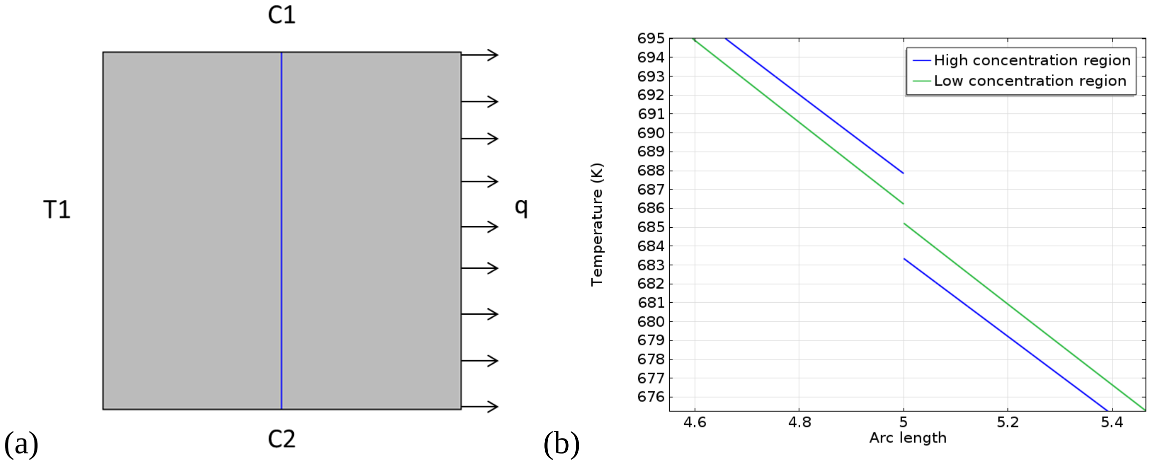

Figure 6-4: (a) Boundary Conditions of the Bicrystal Model Used to Verify the Effect of Kapitza Resistance. *C*: Concentration, *T*: Temperature, *q*: Heat Flux. (b) Resulting Temperature Profiles Close to the Top Boundary (High Concentration region) and Bottom Boundary (Low Concentration Region) .

The Kapitza conductance, in the high concentration region, is calculated to be close to 20 MW/m^2/K with the equation, $G_k = \frac{j}{\Delta T}$, where j is the heat flux. The calculated value, representing the lower bound here, is still higher than the upper bound value in the literature [65]. The discrepancy should be a result of GB thickness. The model here uses a GB thickness of 1 nm, and is suitable to model fuel behavior at low burnup, before the fission gases coalesce in GBs. The geometric effect of fission gas bubbles, which is not considered in this model, can be incorporated given a homogenized representation. The work presented here is to show that GB resistance, as a function of fission gas concentration, can be simulated in this finite element model, and that the temperature drop across the GBs can impact thermal performance of the fuel.

6.2 Controlling Parameters

The transport of FPs is a function of many factors as discussed in the previous chapters. The goal of the simulation work done here is to isolate the effect of each factor and conduct simulations with only one controlling factor at a time to study the effect of each parameter. The parameters to be considered in the model are: sample stoichiometry, temperature effect, Kapitza resistance, heterogeneous GB properties and mass generation.

6.2.1 Baseline 3-D Microstructure Models

A preliminary 3-D simulation was conducted using the reconstructed microstructures from the three samples with different compositions. To setup a baseline model for future comparisons, it is first assumed that all GBs have a high diffusivity value that is five orders of magnitude larger than bulk diffusivity. This choice of the GB diffusivity value serves two purposes. Firstly, the ratio D_{GB}/D_{bulk} is such that the percolation effect becomes significant, as suggested in [111]. Secondly, the value is well within the range of the calculated xenon GB diffusivities as well as experimentally observed values in other materials [112]. The temperature is set to be constant for this case at 1585 K, an average value obtained from the calculated temperature profile across the pellet radius. The same material properties and boundary conditions are applied to all three models to examine the effect of different microstructures. The boundary conditions are applied similarly to those for the bicrystal simulations in section 6.1, where a normalized concentration gradient is applied from top to bottom with the sides insulated. The boundary conditions are set up to create a one-directional diffusion effect, similar to the radial direction in a fuel pellet or a gradient toward a spherical sink. Steady state solutions are obtained for each model, and the concentration profiles for the three different models are shown in Figure 6-5.

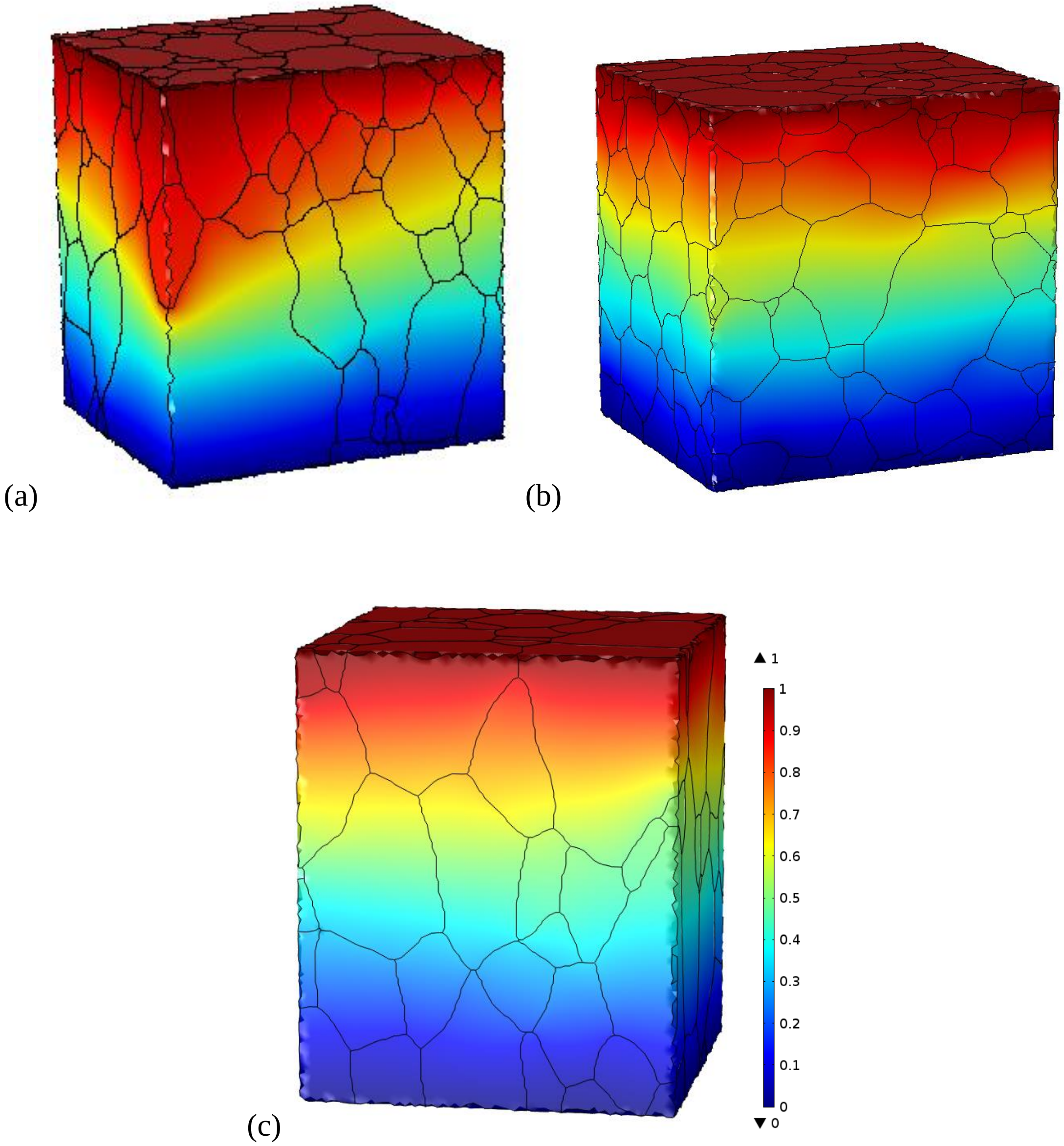

Figure 6-5: 3-D Finite Element Simulation Showing the Effect of High Diffusivity Grain Boundaries on the Diffusion of Fission Products (a) $UO_{2.0}$ (b) $UO_{2.06}$ (c) $UO_{2.14}$.

As seen in Figure 6-5, different models have different concentration distributions, even though they have the same GB properties and are under the same concentration gradient. When all GBs have the same high diffusivity, lateral variation in concentration seems to be affected by the distribution of GBs, which is dictated by grain sizes and shapes. The variation is most significant for sample $UO_{2.00}$ as it has several very large grains that are surrounded by small grains. The diffusional paths are hindered when some GBs lead to the top of a grain bulk (the lower left of Figure 6-5a), and the resulting concentration gradient becomes steep in the region. The $UO_{2.06}$ model, as shown in Figure 6-5b, has a much more uniform concentration distribution due to its small and uniform grain size. The third model, $UO_{2.14}$, has a slight lateral variation that sits between the first two models. However, the work in Chapter 5 showed that the $UO_{2.14}$ model actually has a very similar grain size distribution and average grain size as those for the $UO_{2.00}$ model. The different concentration distribution suggests that the local behavior is sensitive to the neighboring geometry and GB distribution, and that overall statistical information alone is not enough to capture this effect. This is especially important when one takes into account that it is commonly accepted that long-range diffusion does not have a major contribution to FGR [34]. These results suggest that the local behavior that leads to interconnected bubbles can be strongly affected by local variation in microstructural geometry and crystallography.

Another way to examine the concentration profile is shown in Figure 6-6, where the vertical concentration profiles of the three models are plotted. The profiles follow cut lines made close to the centers of x-y planes that probe the regions that cannot be seen from the outer surface. The line distances are normalized to eliminate the effect from the different dimensions in different models. The deviation from a uniform distribution, which should be a straight line with a fixed slope, can be observed for each case as the slope changes. The variation in the concentration profiles in Figure 6-6 follows qualitatively to what was observed in Figure 6-5 with the $UO_{2.00}$ model showing the largest variation.

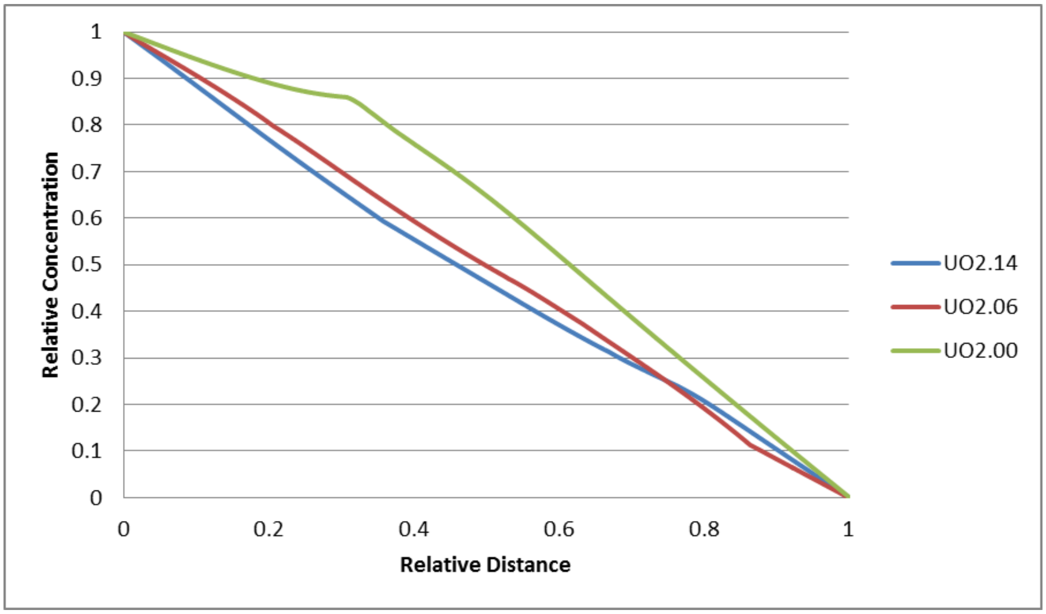

Figure 6-6: Vertical Concentration Profiles along a Cut Line across the Three Models.

It is noticed that a kink in the curve occurs at a relative distance of about 0.3 in the $UO_{2.00}$ microstructure, indicating a discrete change in effective diffusion in the region. To investigate the unexpected phenomenon, the magnitudes of the concentration gradient are plotted in Figure 6-7, showing two perpendicular surfaces containing the cut line used for Figure 6-6. In both surfaces, the cutline started in a smaller grain region and ends in a very large grain that takes almost one third of the area. The GBs in the small grain regions, acting as the fast transport paths, are driving the FGs through the area quickly until they end in the large grain where no GB along the applied concentration gradient is present. The FGs have to either move with the horizontally oriented GBs to the other side of the microstructure or accumulate in the low diffusivity large grain, the latter of which can be observed in the concentration profile shown in Figure 6-5a. The lateral transport can be observed in both surfaces Figure 6-7, indicated by the more continuous and lower concentration paths that are going around the big grain.

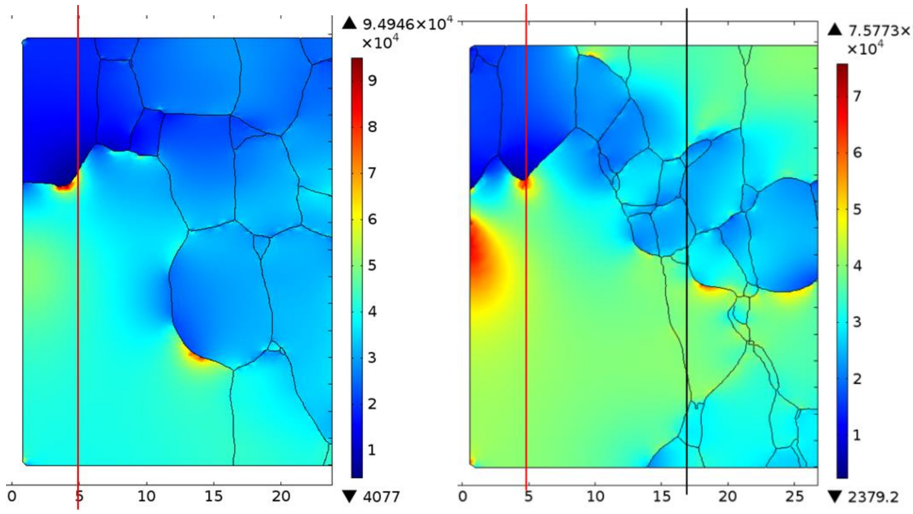

Figure 6-7: Magnitude of Concentration Gradient in Two Perpendicular Cut Planes Containing the $UO_{2.00}$ Concentration Line Plotted in Figure 6-6, as Marked by the Red Lines.

It is also noticed from the right surface in Figure 6-7 that the magnitude of the concentration gradient is determined by the surrounding grains. The regions with large grains have larger concentration gradient, indicating a lower effective diffusivity, and the contrary is observed in small grains region. The black line plotted in the right surface in Figure 6-7 probes a region with different grain size. It goes through four regions of different grain sizes: large - small - large – small, and the concentration profile along the line, plotted in Figure 6-8 can be fitted with four straight lines of different slopes, showing that the effective diffusivity is heavily affected by the local microstructure, which suggests that control of FG transport is possible with a bimodal grain size distributions.

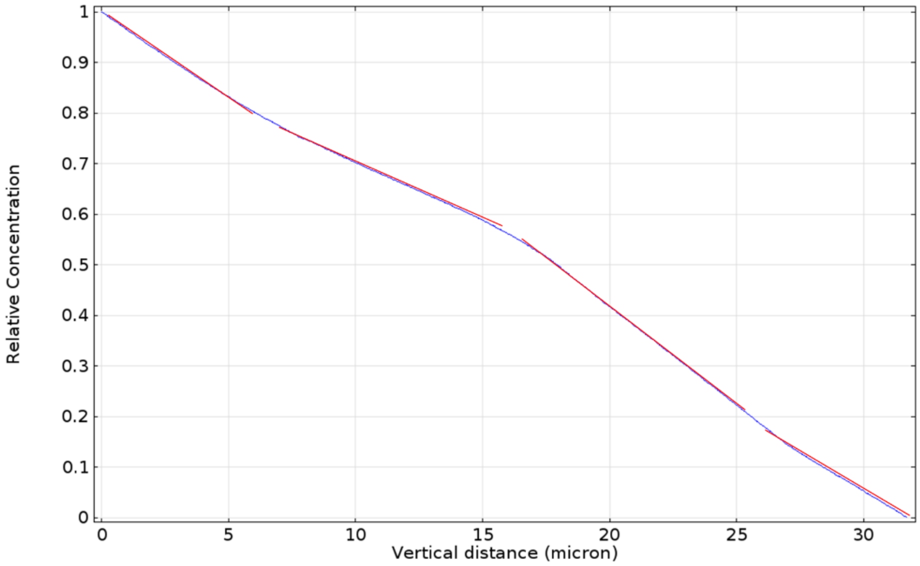

Figure 6-8: The Concentration Profile along the Black Line in Figure 6-7 Showing Different Slopes Due to Differences in Microstructure.

The effective diffusivity can be calculated by running the same simulation but with a mass flux applied at the bottom boundary instead of using zero concentration. The average concentration at the bottom boundaries can be calculated and the effective diffusivity can be derived by dividing the applied flux by the resulting concentration gradient. For all three models, a fixed flux, $4.0\text{x}10^{-15}$ mole/m^{2}s, a value comparable to bulk diffusional flux, is used, and the calculated values are shown in Table 6-1. The $UO_{2.06}$ microstructure has the highest effective diffusivity, which is expected due to its small grain size and uniformly distributed GBs. The $UO_{2.00}$ and $UO_{2.14}$ microstructures have similar grains size, but $UO_{2.14}$ has a higher effective diffusivity. It is most likely the result of several very large and columnar grains that block the diffusion paths in the

$UO_{2.00}$ model. These effective diffusivity values calculated for the three base simulations, which assume a uniform high diffusivity GBs, are the upper bound values at the temperature studied, and will be used as references to compare with other simulations with different physics considered.

Table 6-1: The Calculated D_{eff} from the Base Simulations

Model	Average Concentration	D_{eff} (m^2/s)	D_{eff} / D_{bulk}
UO200	0.925	1.69E-18	10.1
UO206	0.968	3.03E-18	18.1
UO214	0.953	2.57E-18	15.3

The baseline models have shown the effect of microstructure and GB diffusion on the distribution of FGs. Several regions with different grain size distributions were identified, and it was shown that they can affect the FG concentration distribution and the local effective diffusivity. It was also shown that the presence of large grains can reduce the effective diffusivity by up to 44%, due to effects of the variation in microstructures of the studied models, suggesting that FG transport can be controlled locally by modifying the grain size distribution. The models will be modified to include other parameters such as TJ diffusion, temperature gradient, heterogeneous GB properties and mass generation to make the model more realistic in terms of simulating the actual fuel behavior in a reactor.

6.2.2 Triple Junction Diffusion

In addition to GB diffusion, TJs have also been shown to be possible high diffusivity paths for material transport, as discussed in literature review. Many irradiated fuel images have also suggested that interconnected bubbles can develop sooner at TJs than GBs [45]. As a consequence, it is desired to include the TJ networks in the models to study their effects on the transport behavior of FPs. Although experimental data for TJ diffusion is scarce, in the atomistic scale, it is a disordered structure that should require lower energy for dopant atoms to travel in. In the developed multi-physics model, the effect of TJs can be simulated in addition to the GB diffusion using Equation 5-13. The diffusivity value applied in this model is set to be three orders of magnitude higher than GB diffusivity, using the experimental work of Zn diffusing in the TJs of Al from [67] as a reference. The TJ network for the $UO_{2.14}$ model is shown in Figure 6-9. It is assumed here that there is no variation in TJ property. The same boundary conditions as the baseline models are applied.

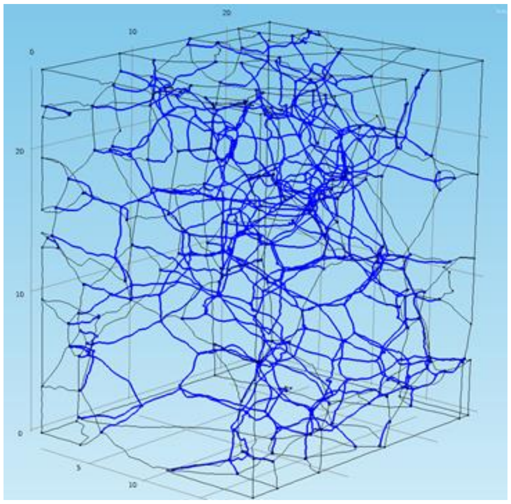

Figure 6-9: Triple Junctions in the $UO_{2.14}$ Microstructure Labeled with Blue Lines.

The simulation result is compared with the baseline model in terms of the vertical concentration profile as plotted in Figure 6-10 for both $UO_{2.00}$ and $UO_{2.14}$ microstructures. In Figure 6-10a, it shows a slight decrease in the concentration in the middle of the line, and the concentration is almost identical after a distance of 20 μm. The effect of TJ diffusion seems limited for this simulation when all GBs have a high diffusivity, and the distribution of GBs is still the dominating factor. The same was observed in the $UO_{2.00}$ microstructure. Figure 6-10b showed that the concentration profile, which is heavily affected by a big grain in the base simulations, is almost identical with the presence of TJ diffusion. The results obtained here have suggested that the TJ diffusion does not have a significant contribution to the non-uniform FG distribution induced by the GB diffusion and variations in microstructure. However, the work in [113] has showed that the TJ diffusion significantly reduced the non-uniformity on FG distribution imposed by heterogeneous GB properties. The part of work will be verified again when GBs of different character are incorporated in the models.

(a) 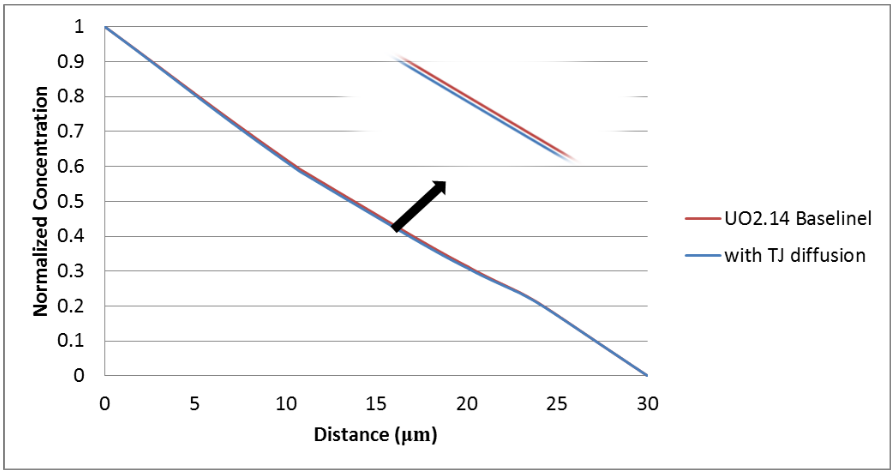

(b) 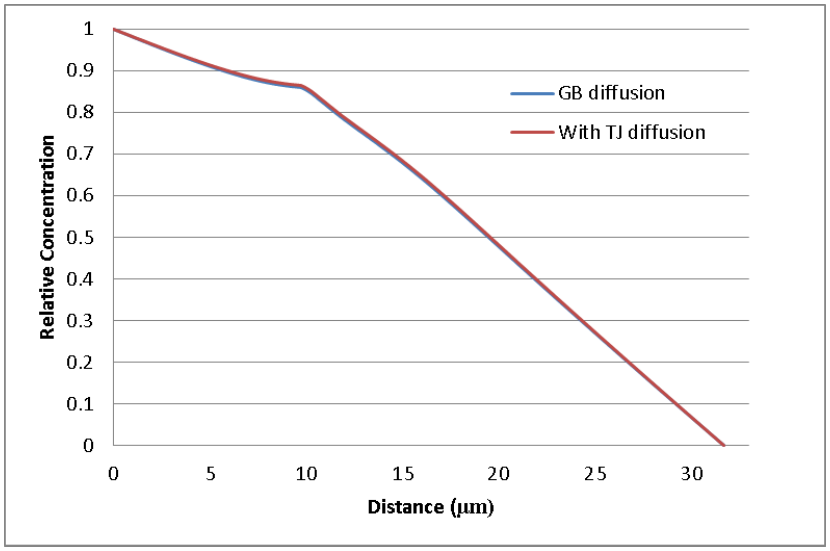

Figure 6-10: The Concentration Profiles along a Vertical Line with and without TJ Diffusion in the (a) $UO_{2.14}$ and (b) $UO_{2.00}$ Microstructure.

6.2.3 Stoichiometry Effect

The study of stoichiometry effects requires the use of the experimental data obtained by Miekeley and Felix [25] and Matzke [38] as they are the few FGR studies available in the literature that took stoichiometry into account. The stoichiometry effect on thermal conductivity is ignored for now as it is not as significant as diffusivity, and the effect also diminishes at elevated temperature. The diffusivity value for $UO_{2.00}$ by Miekeley and Felix is higher than the value from Davies and Long [101] at the temperature studied. The application of the value is then first compared with the diffusivity value from Davies and Long. At the simulation temperature of 1585 K, the diffusivity from Miekeley and Felix for $UO_{2.00}$ is 3.93×10^{-16} m^2/s while it is 1.68×10^{-19} m^2/s from Davies and Long. The difference is over three orders of magnitude. The new $UO_{2.00}$ diffusivity is applied to the $UO_{2.00}$ model, chosen for its larger lateral variation in the concentration profile of the baseline model, with everything else the same.

The obtained concentration profile from the simulation using Miekeley's diffusivity shows little change in concentration gradient. Cut lines are made to probe the variation in the concentration in the middle of the $UO_{2.00}$ microstructure and compare with the base simulation. The results are plotted in Figure 6-11. The concentration profile under the effect of Miekeley's bulk diffusivity is almost linear with very little change in slope; in contrast to the kink that is observed in the base simulation. The higher bulk diffusivity has diminished effect of the percolated high diffusivity GBs as the D_{GB}/D_{bulk} ratio is now less than 800, which is in agreement with the work from [81, 111], which stated that the percolation effect is only significant at the diffusivity ratio of 10^5 or higher. However, the horizontal concentration profile, shown in Figure 6-11b, showed the lateral variation in concentration is still present with the maximum difference of .029, which is an almost 20% difference. It shows that even at a diffusivity ratio as low as 800, GB diffusion can still alter the FG distribution locally.

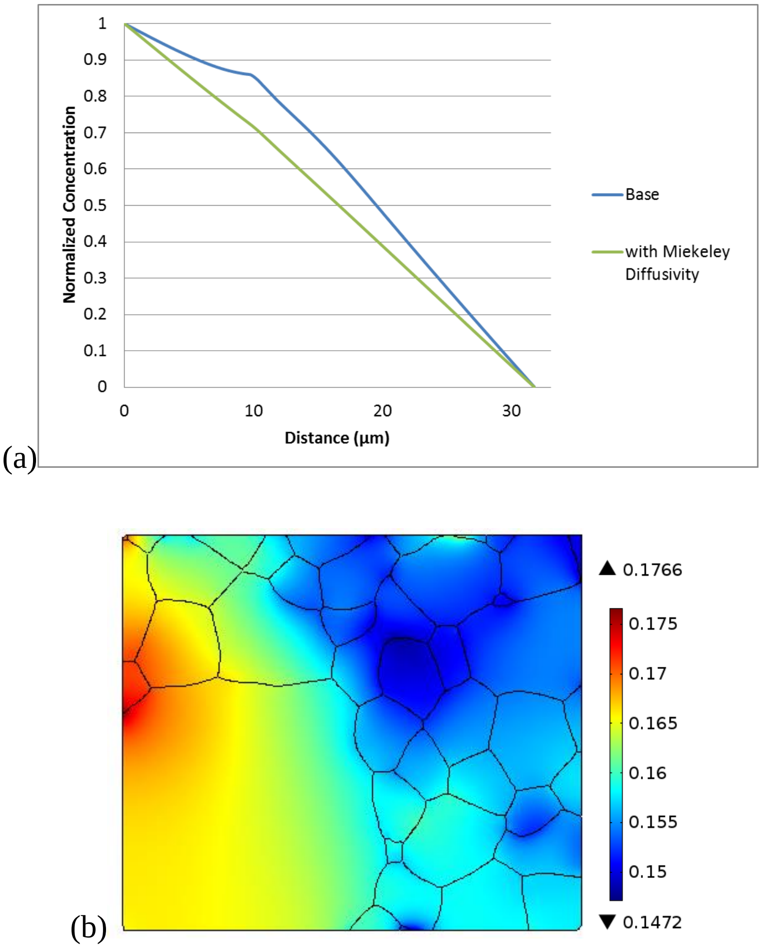

Figure 6-11: (a) Concentration Profile of a Vertical Cut Line across the $UO_{2.00}$ Model, Comparing between the Two Simulations using the Bulk Diffusivity from Miekeley and Davies and Long (Baseline Model). (b) Concentration Profile in a Horizontal Plane 5 μm Away from the Bottom Surface from the Simulation Using Miekeley's Diffusivity.

As it is found that the higher diffusivity applied to grain bulks diminished the variation in concentration profile induced by GB diffusion, it is expected to see similar or stronger effects if the diffusivity of UO_{2+x} is applied to grain bulks. Although the data for hyper-stoichiometric diffusivity differ by a couple orders of magnitudes, it is important to keep in mind that if the bulk diffusivity is enhanced to high enough levels due to stoichiometry, the effect of GB diffusion can be neglected.

6.2.4 Temperature Effect

The material properties needed for the simulations are all temperature dependent, especially the FP diffusivities, which have an Arrhenius relationship with the temperature. The diffusivity values can span a few orders of magnitude given the high temperature gradient found in a fuel pellet. The effect of temperature is studied by applying the highest observed temperature gradient in a fuel pellet, which is about 10000 °C/cm [6], to the developed models. The GB diffusivity, in this case cannot be set to a fixed ratio with D_{bulk} because it is also temperature dependent with different activation energy. Using the GB diffusivity (D_{GB}) derived by Olander (Olander 1 in Figure 5-9), calculated using the bulk diffusivity data by Davies and Long [101], one can plot the ratio between D_{GB} and D_{bulk} as shown in Figure 6-12. Note that the difference is larger at low temperatures and decreases with increasing temperatures. It is desired to investigate regions with different temperatures to check if different behaviors exist.

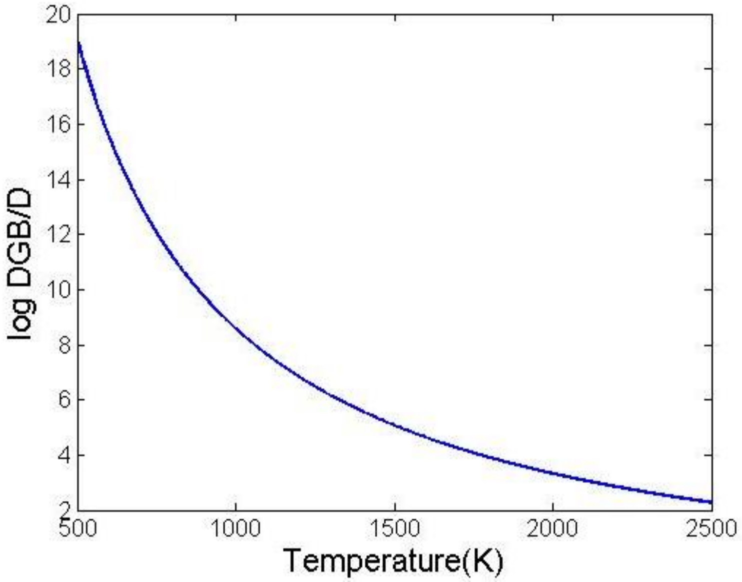

Figure 6-12: Ratio Between Grain Boundary Diffusivity and Bulk Diffusivity. The Values Are Based on Davies and Long (Bulk) and Calculation from Olander (GB).

The simulation is first done using the $UO_{2.00}$ microstructure. A temperature gradient, from 1600 K to 1570 K, is applied in the same direction as the concentration gradient. The temperature gradient should introduce a higher diffusivity in the hot region while a lower diffusivity in the cold region. Simulations, with and without a temperature gradient, were conducted, and the vertical concentration profiles along two different lines, shown in Figure 6-13a, are plotted in Figure 6-13b. In both concentration profiles, the temperature effect introduces a higher and flatter concentration profile in the hot region to accommodate the higher diffusivity followed by a sharp drop in the cold region. The behavior is expected when the FG travels faster in the hot region and gets slowed down in the cold region.

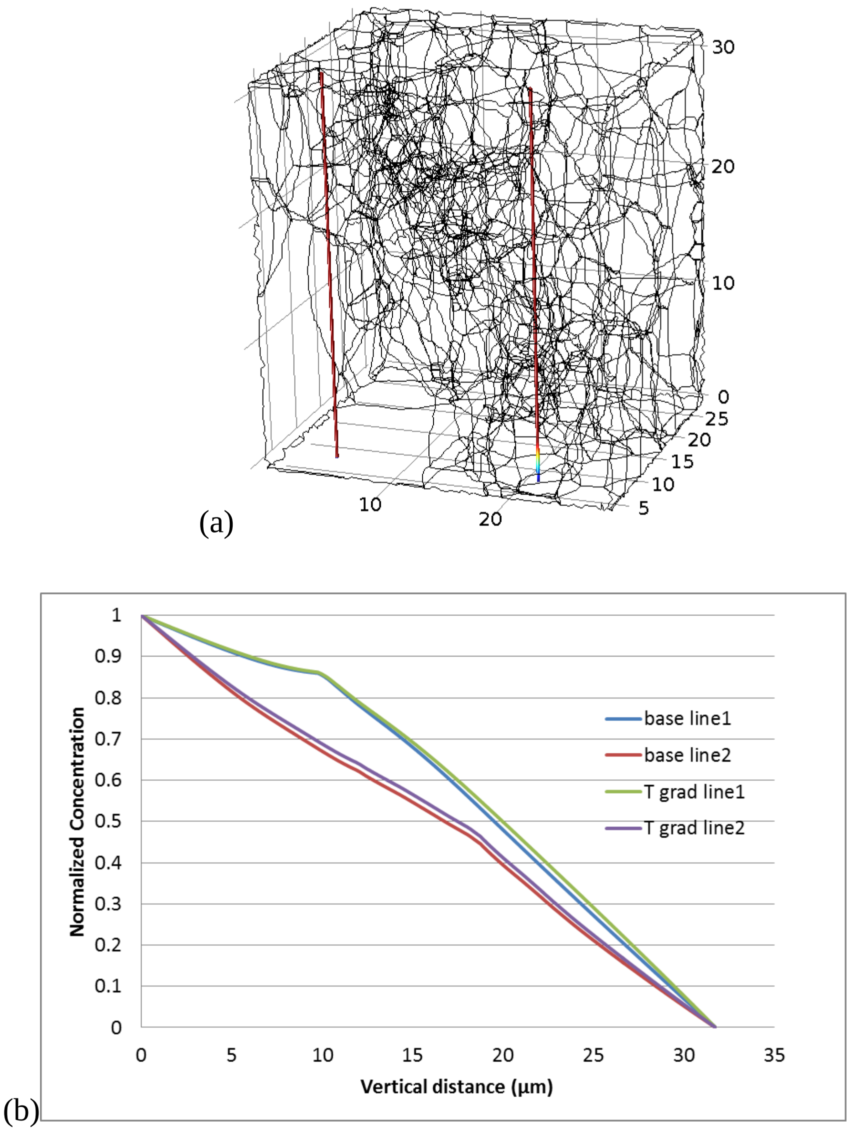

Figure 6-13: (a) The Two Vertical Lines Indicating the Locations the Line Profiles Are Plotted with Line1 on the Left and Line2 on the Right. (b) The Vertical Concentration Profiles along the Two Vertical Lines in (a) Comparing the Effect of the Temperature Gradient with the Base Simulation in the $UO_{2.00}$ Microstructure.

It has been discussed that the direction of a temperature gradient does not necessary follow the concentration gradient. The pellet temperature is usually the highest in the center and decreases along the radial direction while the FG concentration is usually the highest at the edge and can be heavily affected by the presence of local porosity. To investigate the effect of different temperature gradient directions, the same simulation was conducted using the $UO_{2.14}$ microstructure and included the effect of a reverse temperature gradient. The resulting vertical concentration profile is plotted in Figure 6-14, in comparison with the base model and the simulation with a forward temperature gradient. Similar to previous simulation, the case with a forward temperature gradient is found to increase the concentration in the hot region and results in a sharper drop in the cold region. For the case of the reverse temperature gradient, the effect is inverted with a lower overall concentration across the line. The first 10 μm of the vertical line is now the cold region with a lower diffusivity, with which a larger concentration gradient is needed to sustain the applied mass flux. In the lower hot region, the concentration gradient decreased due to a corresponding the increase in diffusivity.

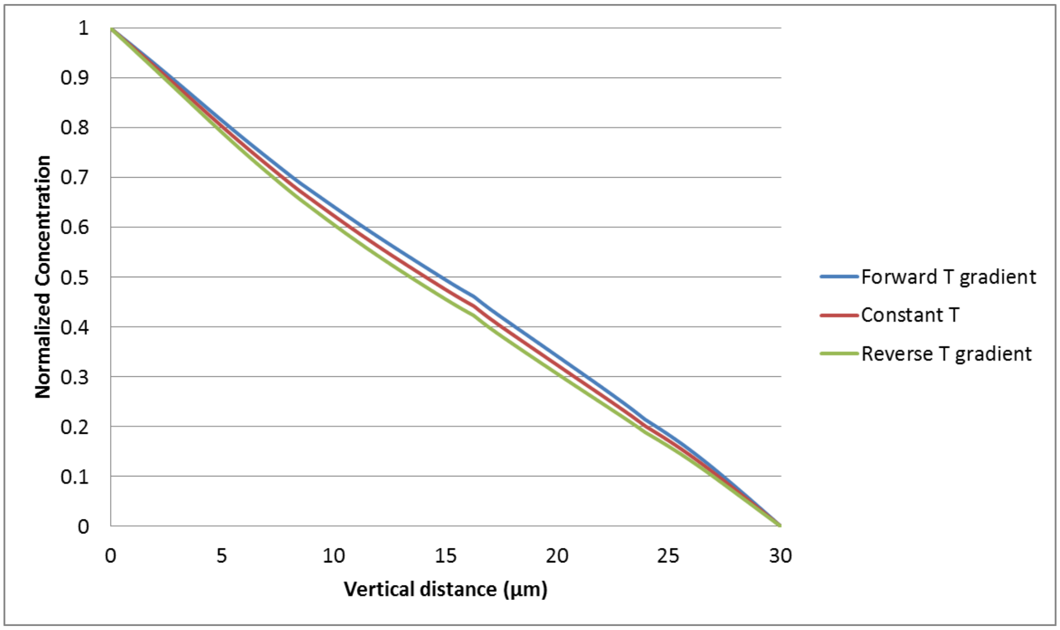

Figure 6-14: The Linear Concentration Profiles under the Effect of a Constant Temperature, a Forward Temperature Gradient and a Reverse Temperature Gradient.

From Figure 6-12, the GB diffusivity is much higher than bulk diffusivity at lower temperatures. To observe the difference, a temperature gradient from 830 K to 800 K is applied to the $UO_{2.14}$ microstructure. The temperature range matches the region close to the edge of the pellet. The diffusivity ratio is over 8 orders of magnitude at this temperature range. The resulting concentration profile is plotted in Figure 6-15 in comparison with the concentration profile obtained above. At low temperature, the concentration profile follows a similar trend as the high temperature profile since they have the same GB distribution. The low temperature line has an overall higher concentration, which is likely due to the overall lower diffusivity. The low temperature profile also deviates from the reference line showing the effect of a higher diffusivity ratio.

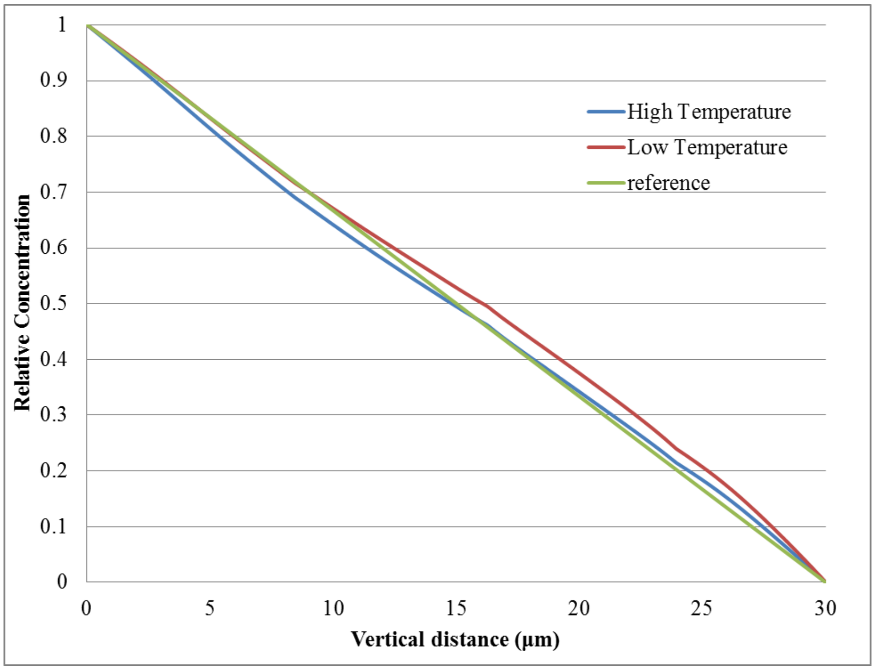

Figure 6-15: The Concentration Profiles under the Influence of High Temperature (1600 K – 1570 K) and Low Temperature (830 K – 800 K). The Reference Line Is a Straight Line Representing a Perfectively Uniform Concentration Gradient.

6.2.5 Effects of Heterogeneous Grain Boundary Properties

The EBSD data provide information for the distribution of the GB types, as classified by their misorientation angle and CSL type. The GBs of different characters, defined in Table 5-1, are now assigned with different diffusivities. A two-level diffusivity system is applied with the high angle GBs assigned with a high diffusivity value (Olander1 in Figure 5-9), and the middle angle GB along with the low angle and CSL GBs assigned with a low diffusivity, the same value as bulk diffusivity. Steady state solutions are obtained at a constant temperature of 1585 K. The distribution of the high diffusivity GBs and the resulting concentration profiles for each microstructure are plotted in Figure 6-16.

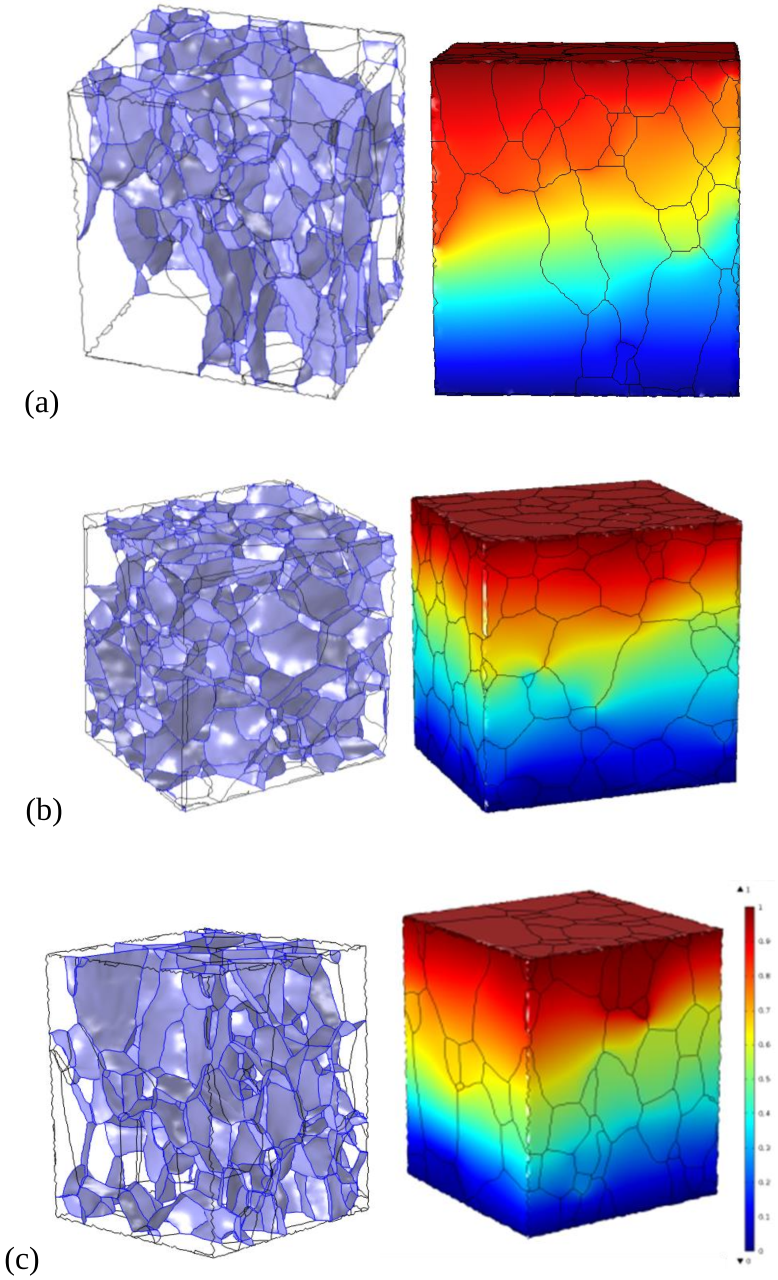

(a)

(b)

(c)

Figure 6-16: The Distribution of GBs Assigned with a High Diffusivity Value and the Resulting Surface Concentration Profiles for Sample (a) $UO_{2.00}$ (b) $UO_{2.06}$, (c) $UO_{2.14}$.

The first significant observation from the concentration profiles is that the presence of the two-level heterogeneous GB properties increased the non-uniformity in the concentration profiles as compared with the base simulations. The distribution of FGs is no longer controlled only by the grain size distribution, which is the main reason for the variation of concentration in the base models. Even though the fractions of high diffusivity GBs in all three cases are still much higher than some calculated 3-D percolation threshold values, e.g., about 0.25 for a cubic boundary network [53], the presence of a small fraction of low diffusivity GBs still alters the concentration distribution.

The effect can be better explained by making cross-sectional concentration profiles as shown in Figure 6-17 and Figure 6-18, which capture some lateral variations in concentration through the depth of the models. First of all, these concentration profiles show that the high concentration region is not limited to one side of the model and can change fairly quickly through the thickness. Secondly, the distribution of high concentration region is no longer controlled solely by the grain sizes. The distribution of high and low diffusivity GBs is also very important as the concentration profile now shows several small grains with high concentrations, which differ from the conclusion drawn from the base simulation stating that the small grain region results in lower concentration laterally.

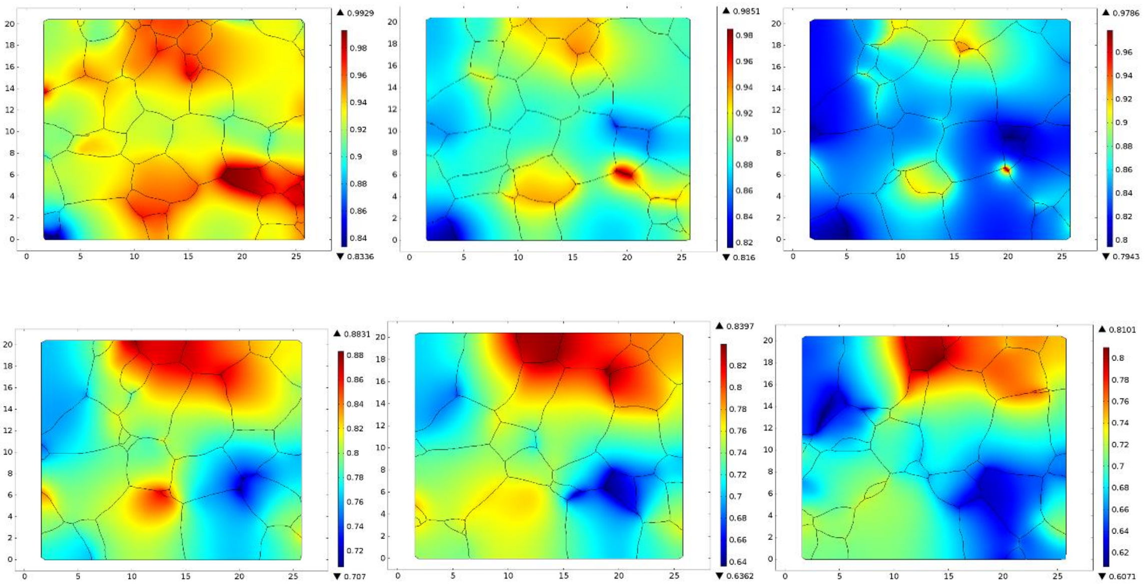

Figure 6-17: The Cross Sectional Concentration Profiles Showing the Changes in Relative Concentration through the Thickness of the $UO_{2.06}$ Model. Each Slice Is 1 μm Apart.

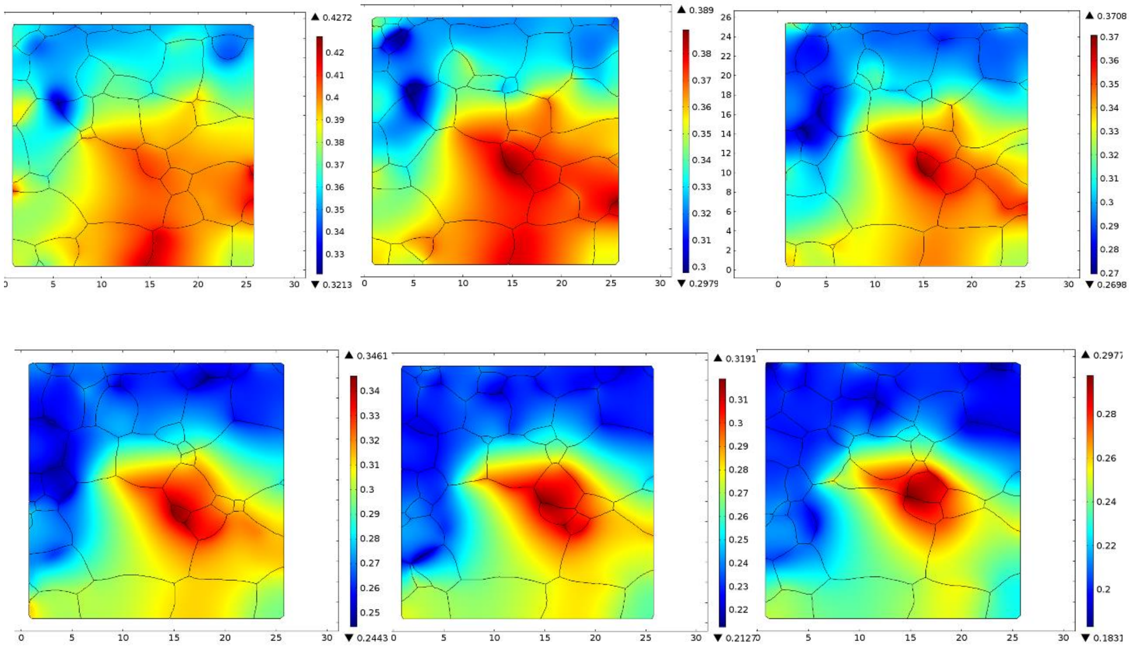

Figure 6-18: The Cross Sectional Concentration Profiles Showing the Change in Relative Concentration through the Thickness of the $UO_{2.14}$ Model. Each Slice Is 1 μm Apart.

The formation of these regions of high concentration can be explained by exploring the grain shape and GB properties locally in the 3-D microstructure. In Figure 6-19a, the highly concentrated grain in the $UO_{2.06}$ simulation is identified from the 3-D grain structure with the high diffusivity GB labeled. The 3-D grain structure shows that the high diffusivity GBs become discontinuous at the bottom of the grain, as boxed in red. The FG atoms that are transported to the region have to accumulate in the area and that eventually results in a high concentration region. Similarly, Figure 6-19b shows the high concentration grain in the center of the cross sectional cut 23 μm away from the top surface. The discontinuity in high diffusivity GBs is also found to result in the high concentration region. Note that the two cases discussed here both have grains that are well surrounded by the high diffusivity GBs; however, it is the nature of the GBs that follow along the applied concentration gradient that leads to the regions with local high concentration. The work presented here shows that the distribution of FGs not only depends on the distribution of the GBs, but also on their connectivity and the orientation to the concentration gradient. The GBs in the high concentration regions are expected to capture enough FGs for bubble interconnection earlier than other GBs do.

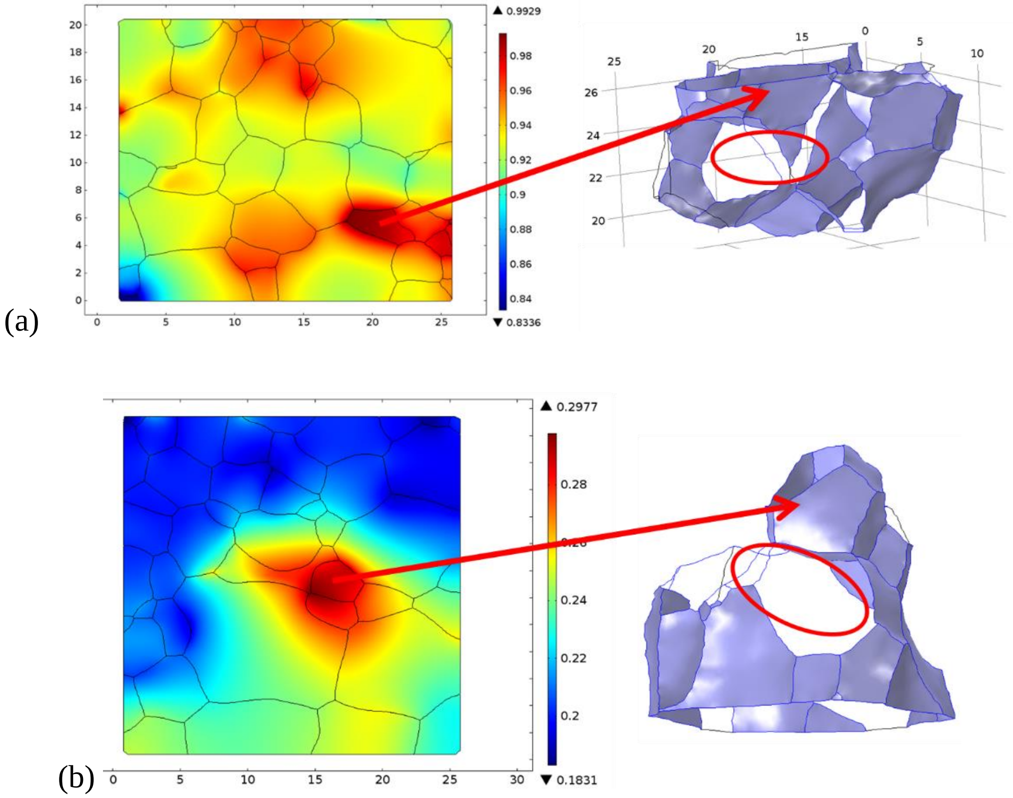

Figure 6-19: A Highly Concentrated Grain and Its Neighboring Grain Structure in 3-D with High Diffusivity GB Labeled (a) in UO$_{2.06}$ Model (b) UO$_{2.14}$ Model. The Red Circles Indicate the Discontinuity in High Diffusivity GBs.

It has been discussed that the connectivity of GBs is correlated by crystallographic constraints, and that the resulting GB network is different from a random GB network as suggested in [56]. The GBs with heterogeneous properties are categorized based on characterization results and can be considered as correlated GBs. Using the same $UO_{2.06}$ microstructure model, a different simulation can be conducted by assigning GB properties at random. The same 71 % high diffusivity GBs are chosen using a random number generator and assigned to the model. The simulation is conducted using the same boundary conditions, and the resulting concentration profiles under the effect of correlated GBs and random GBs are plotted in Figure 6-20, along with the distribution of the assigned low diffusivity GBs. The difference is actually significant as the random GBs resulted in a much more uniform concentration profile. It also appears that the low diffusivity GBs are much more evenly distributed in the random GB case. In principle, it agrees with the literature [114], which suggests that two CSL GBs connected at a TJ requires a third CSL GB, in a way that the correlated GBs model has a better connected low diffusivity GBs and thus a higher lateral variation in concentration. However, the fraction of CSL GB is fairly small in these models studied, and a bigger network along with more analysis will be needed before such conclusion can be drawn. The quick message here is that the correlated GBs will result in a different FG distribution as compared with the random GB case.

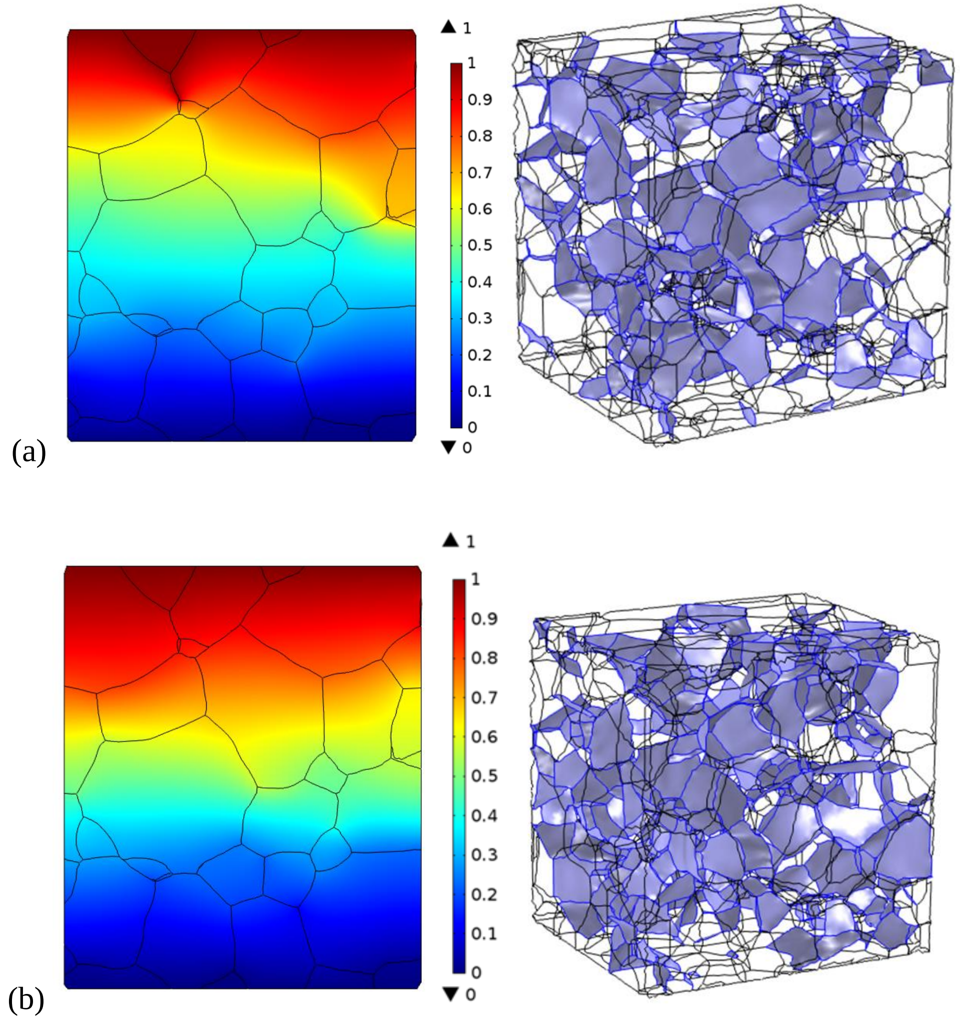

Figure 6-20: The Concentration Profiles under the Effect of (a) Correlated GBs (b) Random GBs with the Low Diffusivity GB Labeled.

Finally, the effect of TJ is revisited by apply a high diffusivity to all TJs in the $UO_{2.14}$ model with heterogeneous GB properties. The resulting change in concentration profile is shown in Figure 6-21, which shows that the TJ diffusion straightens the concentration line profile. The effect is more obvious than what is observed from the base simulation as the heterogeneous models are expected to have more disconnected high diffusivity GBs, and the presence of the high diffusivity TJs compensates for these discontinuities and thus results in a more uniform concentration profile.

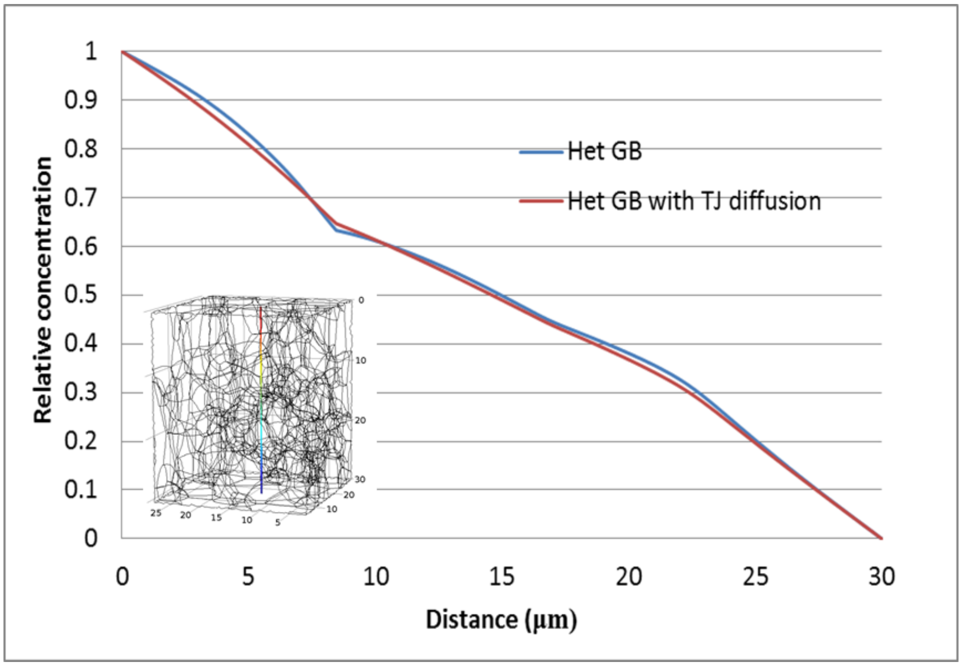

Figure 6-21: The Effect of TJ Diffusion in the Heterogeneous GB Properties Model in the $UO_{2.14}$ Microstructure.

6.2.6 Mass Generation

The rate of fission gas generation was calculated in the previous chapter and the result can be applied to grain bulks as a source term. Now, instead of applying a normalized concentration gradient, the evolution of the fission gas generation can be studied from the very beginning of fuel life when the FG concentration is zero everywhere. The simulation was conducted by assigning only the bottom boundaries with a fixed zero concentration, representing a sink for FGs, with other boundaries insulated. The source term is included in the partial differential equation for mass diffusion for grain bulks where the FGs are generated. The surface boundaries are now given the same diffusivity as the GBs to allow tangential mass diffusion to prevent the high concentration region from forming at the surfaces due to the insulated boundary condition.

The resulting concentration cross section is plotted in Figure 6-22. At steady state, the regions with high concentration reside within the large grains. The closer they are to the GBs, the lower the concentration is. A similar behavior was also observed in the base simulations, which showed higher concentrations in regions with large grains. The approach of assigning mass generation can be used to identify the GBs where the bubbles first become interconnected when unsteady simulations can be conducted. The results obtained also offer a better comparison with experimental data. A concentration line profile across a grain in Figure 6-22 is plotted in Figure 6-23a, which shows that the highest concentration is at the center of the grain. This behavior was also observed by Walker [107] during a study of xenon concentration across a grain using electron probe microanalysis.

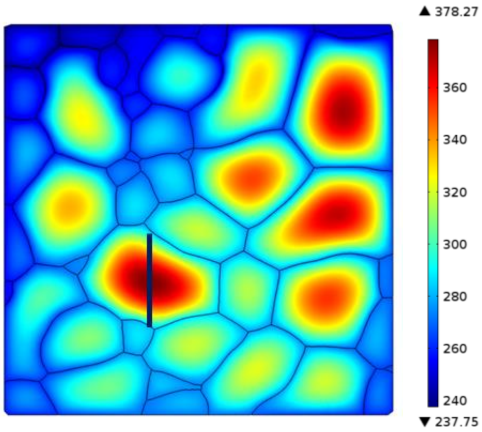

Figure 6-22: Concentration Profile of a Cut Plane 15 Micron Away from the Top Surface from a Mass Generation Simulation for the $UO_{2.14}$ Microstructure

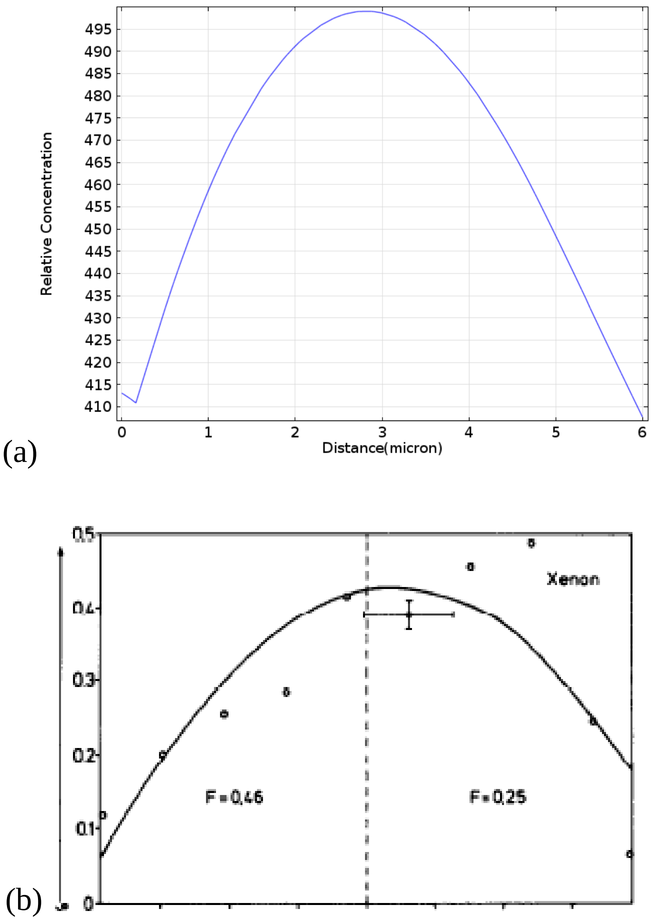

Figure 6-23: (a) The Concentration Profile across the Black Line in Figure 6-22 (b) Experimentally Measured Xenon Concentration across a Grain at a Normalized Radial Position of 0.6 [107].

6.2.7 Grain Boundary Kapitza Resistance in Polycrystalline Models

The approach to simulate GB Kapitza resistance that was demonstrated with a bicrystal model is now applied to the $UO_{2.14}$ microstructure to demonstrate its effect in a polycrystalline microstructure. The same boundary conditions as the bicrystal model are used, and the applied concentration is normalized in a way that the maximum GB coverage, which is the X_{GB} term in Equation 5-16, is 50% to match experimental observations [79]. The resulting temperature profile along a horizontal cutline is plotted in Figure 6-24. Several temperature drops, which are induced by the GB resistance, can be observed. The resulting temperature profile in the right surface is shown in Figure 6-25, which has a maximum temperature difference of about 12 K. The difference in temperature distribution is affected by the grain shapes. The average temperature in the right surface can be calculated, and the effective thermal conductivity can be calculated.

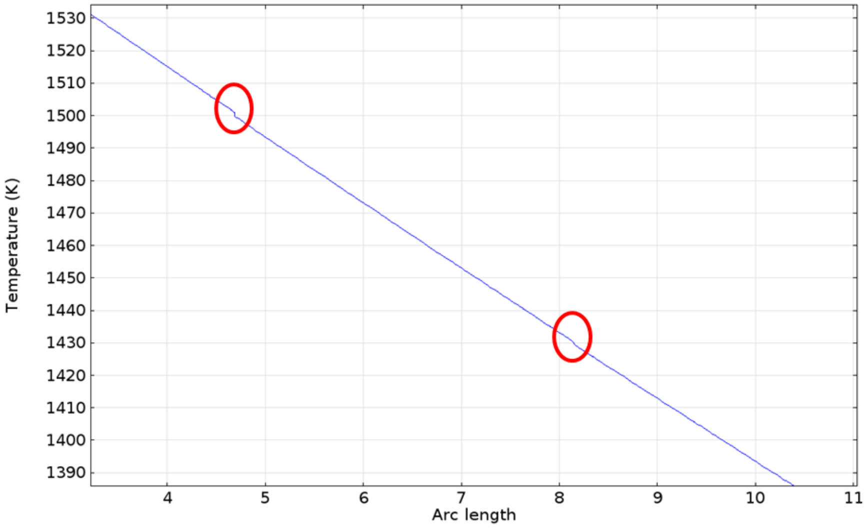

Figure 6-24: A Section of the Temperature Profile in the $UO_{2.14}$ Model Showing the Temperature Drops under the Effect of the Kaptiza Resistance.

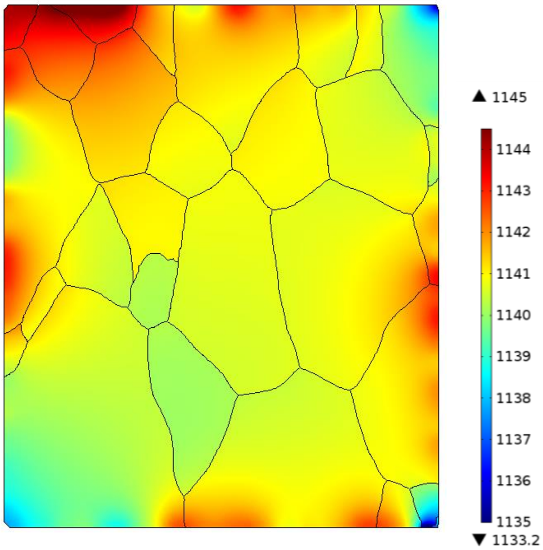

Figure 6-25: The Temperature Profile (K) on the Right Surface of the Model under the Effect of GB Resistance.

To compare the results in the different microstructures, the same simulation was conducted on the three reconstructed models: $UO_{2.00}$, $UO_{2.06}$ and $UO_{2.14}$, with and without the effect of GB Kapitza resistance. The results are shown in Table 6-2 in terms of the percent change in effective thermal conductivity and the temperature difference per micrometer induced by GB Kapitza resistance. The results are similar in all three models with the % change in k_{eff} from 0.54 % to 0.60 % and the temperature drop per micrometer from 0.10 K/µm to 0.12 K/µm. The values seem to be dependent on the number of grains, which is the largest in $UO_{2.06}$ and the smallest in $UO_{2.14}$. Although the changes in temperature seem small in the microstructure models, the overall effect over the whole radius of a fuel pellet can be significant. However, a direct comparison should be made here as the heat flux may vary in the fuel pellet. The work here demonstrated that the model can be used to study the thermal performance of a fuel pellet under the effect of microstructure and FGs.

Table 6-2: The Change in Effective Thermal Conductivity in the Three Different Microstructures.

Model	% change in k_{eff}	ΔT(K) / μm
$UO_{2.00}$	0.60	0.11
$UO_{2.06}$	0.65	0.12
$UO_{2.14}$	0.54	0.10

6.3 Multi-Physics Effects on Fission Product Transport

The simulations conducted in section 6.2 provided a basic idea on the effect that each phenomenon of interest to this work had on the transport of FPs. The multiphysics effect, which is the goal of creating such models, is studied next. The different physics are coupled by the transport properties, which are temperature dependent, as well as the concentration-dependent GB resistance, which has been shown to affect the temperature profile. It is important to point out again that this model is suitable for simulating the behavior before the formation of interconnected bubbles, i.e., at low burnups. The three reconstructed models of different stoichiometry will be used to study the transport behavior at different radial positions of a fuel pellet. Finally, a sensitivity study will be conducted to discuss the effect of the large spread in some experimentally obtained material properties.

6.3.1 Microstructurally Explicit Simulation of $UO_{2.00}$, $UO_{2.06}$ and $UO_{2.14}$

The three microstructures, each representing a different stoichiometry, are used to probe the transport behavior of FGs at different radial position using the window method [115]. The technique places a representative volume element (RVE) that is microstructurally explicit in a homogeneous matrix to study the interaction between the micro and macroscale. The stoichiometry of fuel elements changes with increase in burnup due to uranium consumption as well as oxygen migration. According to Figure 2-2, sample oxygen stoichiometries of 2.14, 2.06 and 2.00 can be used to approximate the center, mid-radius and edge stoichiometry in a fuel pellet, respectively. The temperature range at each location is also approximated from the temperature profile derived and plotted in Figure 5-11. The three reconstructed models are used to conduct multi-physics simulations that include the effect of stoichiometry, temperature, Kapitza resistance and heterogeneous GB properties.

Similar to previous simulations, a normalized concentration gradient is applied along with other temperature dependent material properties. For the effective Kapitza resistance calculation to make physical sense, the maximum concentration value is normalized to have GB coverage of 50% to study the FG distribution before the bubbles interconnect. The bulk diffusivity values now depend not only on the temperature, but also on the stoichiometry. The hyper-stoichiometric diffusivity data derived by Miekeley and Felix [25] has no x dependence in UO_{2+x}. As a result, the work by Matzke [38], which has the diffusivity data for two hyper-stoichiometric samples, is used and interpolated to be applied to the $UO_{2.06}$ and $UO_{2.14}$ models. Grain boundary diffusivity is kept the same for all three models with the two-level heterogeneous GB distribution, the same as the work in 6.2.5. Table 6-3 lists the parameters used for each model. Now the microstructurally explicit models that are coupled with the thermal transport can be used to study the FG behavior at low burnup.

Table 6-3: Parameters for Multiphysics Simulations.

Model	Radial position	Temperature range (K)	Diffusivity
$UO_{2.00}$	edge	830-800	D_{bulk}
$UO_{2.06}$	middle	1600-1570	$57.5D_{bulk}(T=1585)$
$UO_{2.14}$	center	1900-1870	$35.6D_{bulk}(T=1885)$

The three models are calculated and the FG concentration profiles are collected. It is first noticed that the simulation results for both $UO_{2.14}$ and $UO_{2.06}$ show no lateral variation from the surface concentration plots, as shown in Figure 6-26a and Figure 6-27a. The reduction in the D_{GB}/D_{bulk} ratio along with the increase in bulk diffusivity due to stoichiometry has eliminated the GB effect that was observed before. However, it is found that a slight local variation produced by GBs are still present in the cross sectional concentration profile for the $UO_{2.06}$ model, as shown in Figure 6-26b. A maximum concentration difference from the concentration profile is about 0.03, which is 4 % of the minimum concentration, comparing with that of less than 1 % in the $UO_{2.14}$ model shown in Figure 6-27. The results indicate that the effect of GB diffusion diminishes with increases in temperature and oxygen content.

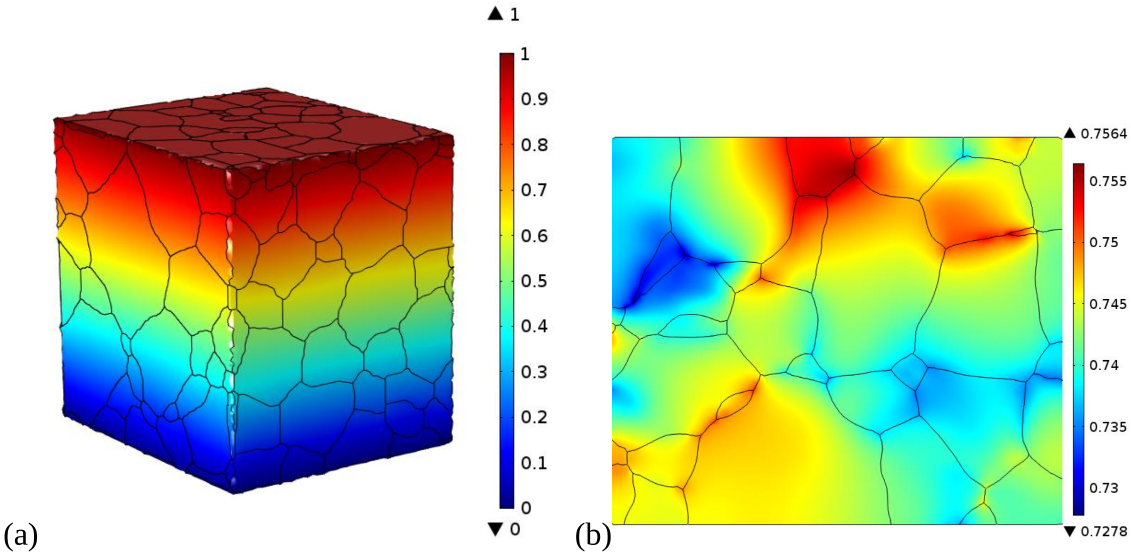

Figure 6-26: (a) The Concentration Profile of the $UO_{2.06}$ Model under Mid-Radius Conditions (b) A Horizontal Cross-Sectional Slice of the Concentration Profile.

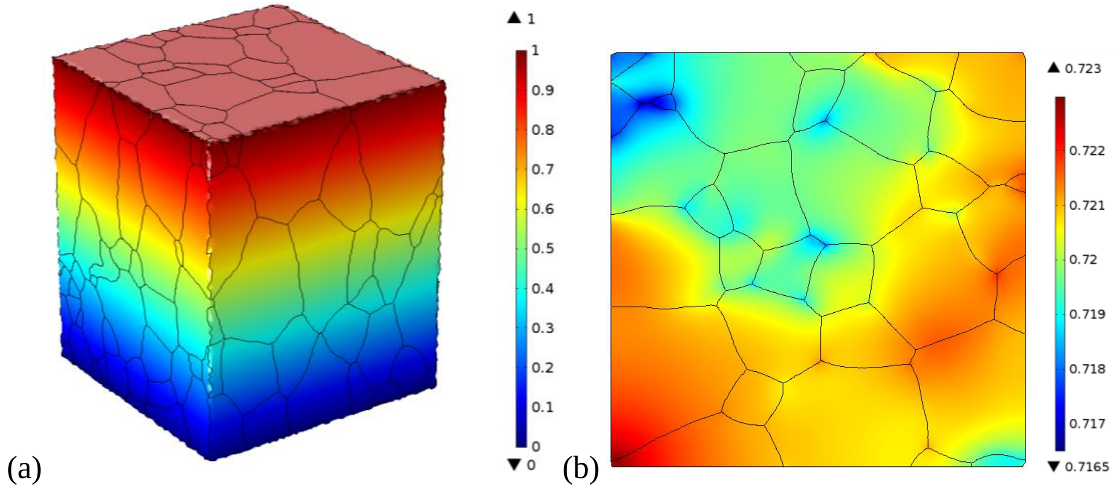

Figure 6-27: (a) The Concentration Profile of the $UO_{2.14}$ Model under Center Pellet Conditions (b) A Horizontal Cross-Sectional Slice of the Concentration Profile.

The increase in bulk diffusivity due to the oxygen content as a multiple of intrinsic bulk diffusivity (Davies and Long) is listed in Table 6-3, calculated with respect to the corresponding simulation temperatures. The increase in bulk diffusivity as compared to the intrinsic diffusivity in the $UO_{2.06}$ model is about 57 fold. Although the number is much smaller compared to the ratio between GB diffusivity and bulk diffusivity, it is large enough to diminish the effect of GBs that was observed in the base simulation and the simulation with heterogeneous GB properties. In the $UO_{2.14}$ model, which is simulated at a higher temperature, the D_{GB}/D_{bulk} ratio is even smaller according to Figure 6-12. The stoichiometry of 2.14 also makes the bulk diffusivity 35.6 times larger at the temperature range studied. The combined effects result in a uniformly distributed concentration profile that shows little GB effect.

The $UO_{2.00}$ model, on the other hand, has the largest D_{GB}/D_{bulk} ratio, given that the bulk diffusivity is the reference. The resulting concentration profile, which is plotted in Figure 6-28, shows large lateral variations induced by the GB diffusion. To make good comparisons among the models, the effective diffusivity (D_{eff}) for each model is calculated by applying a fixed flux and measuring the resulting concentration gradient. The value for each model is listed in Table 6-4. Although this parameter is heavily affected by the temperature, its ratio to the applied bulk diffusivity (D_{UO2+x}) value at the same temperature range provides insights into the GB effect. The D_{eff}/D_{UO2+x} calculated for $UO_{2.00}$, $UO_{2.06}$ and $UO_{2.14}$ models are 6.35, 1.2 and 1.02. These values provide ideas for the effective diffusivity enhanced by GB diffusion, and they showed that the D_{eff} for $UO_{2.06}$ and $UO_{2.14}$ are only slightly larger than the diffusivity of the bulk. This explains why uniform concentration profiles were observed for both cases.

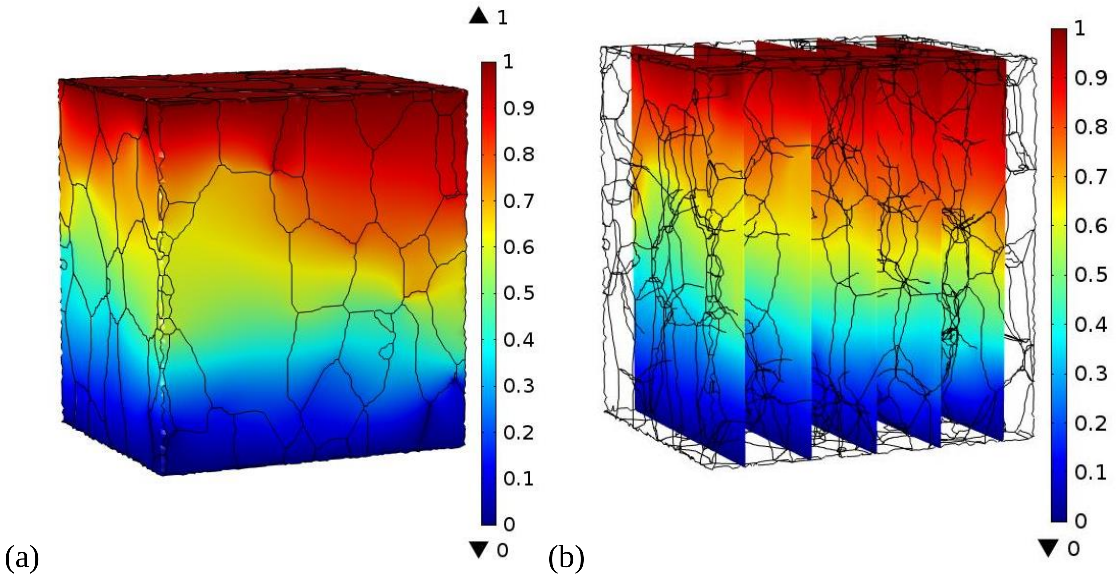

Figure 6-28: (a) The Concentration Profile for the Multiphysics Simulation of the $UO_{2.00}$ Model under Edge Conditions (b) Vertical Slices of the Concentration Profile with the Outline of the Microstructure.

Table 6-4: The Effective Diffusivities Calculated from the Multiphysics Simulations.

Model	D_{eff} (m^2/s)	D_{eff} / D_{bulk}	D_{eff} / D_{UO2+x}
$UO_{2.00}$	8.02E-28	6.35	6.35
$UO_{2.06}$	1.16E-17	69.1	1.2
$UO_{2.14}$	2.11E-16	36.5	1.02

The results suggest that the GB diffusion is not making a contribution to the fission gas transport in the high temperature regions, especially in the center of a fuel pellet. The bulk diffusion enhanced by excess oxygen is the key parameter. In addition, other effects such as evaporation and GB sweeping that are most commonly observed in the hot region will also take over the diffusion and become the major mechanism for FGR. The GB effect, on the other hand, is the most significant at the edge of a fuel pellet. The results showed that the distribution of FGs is heavily affected by the distribution of different GBs, despite the fact that the number of high diffusivity GBs is much higher than the percolation threshold calculated for a cubic boundary network. The microstructure at the edge is also the least affected by the microstructure reconstruction due to temperature and stoichiometry enhanced diffusion. The results obtained here provide insight as how the FGR can be better predicted. The controlled release is also possible by coupling the present microstructure models with the control of grain sizes, e.g., bi-modal grain size distribution, or GB engineering, which can alter the fraction of high and low diffusivity GBs.

6.3.2 Sensitivity Analysis

The applied values with large uncertainty in the experimental work include GB thickness, bulk diffusivity and GB diffusivity. Sensitivity analysis was conducted using the $UO_{2.14}$ model to test the effect of different GB thickness on effective diffusivity. The GB thickness values of 0.5, 1, 5, 10 and 50 nm are simulated, and the results in terms of effective diffusivity are compared. The effect of bulk and GB diffusivity will be tested in various combinations, using the higher and lower bound values collected from the literature. Table 6-5 below shows all the combinations used in the sensitivity study.

Table 6-5: Applied Diffusivity Combinations for Sensitivity Analysis.

Study	D_{bulk}	D_{GB}
Base	D_{mid} (Davies and Long)	D_{mid} (Olander 1)
1	D_{high} (Miekeley)	D_{high} (Gover)
2	D_{high}	D_{low} (Olander 2)
3	D_{low} (Cornell)	D_{high}
4	D_{low}	D_{low}

The GB thickness is examined first because it directly affects the effective value of GB diffusivity. The study is conducted by re-running the multi-physics simulations for the three models from 6.3.1. Results show no significant change in the concentration profiles for the whole surfaces with increasing GB thickness. However, in the cross sectional concentration profile for the $UO_{2.14}$ model, which showed no effect of GB diffusion, variations start to show with the increase in GB thickness. Figure 6-29 shows a concentration profile of the model ran with a 10 nm GB thickness. The maximum concentration difference is now 0.047, which is close to a 10% variation.

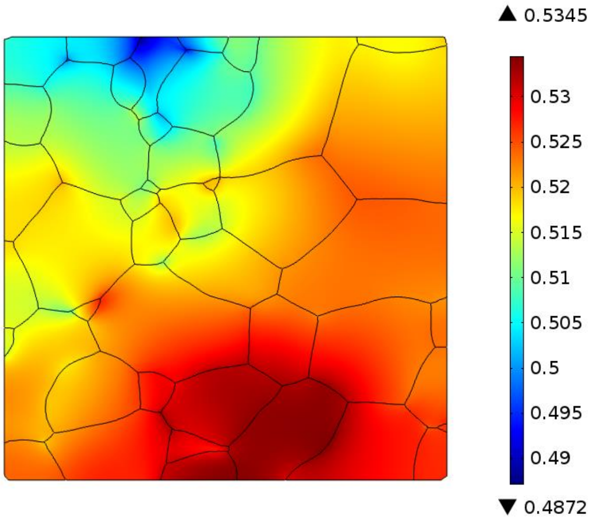

Figure 6-29: The Cross-Sectional Concentration Profile for a $UO_{2.14}$ Multiphysics Simulation with a 10 nm GB Thickness.

The effective diffusivity for $UO_{2.00}$ is calculated with respect to the increase in GB thickness as plotted in Figure 6-30 below. This model, which was previously shown to be strongly influenced by GB diffusion, does not show much increase in D_{eff} with increases in GB thickness. The result agrees with the work by Chen [55], which showed the change in D_{eff} is small when the fraction of high diffusivity GB passes the percolation threshold. The value stops increasing with a GB thickness of 5 nm or higher.

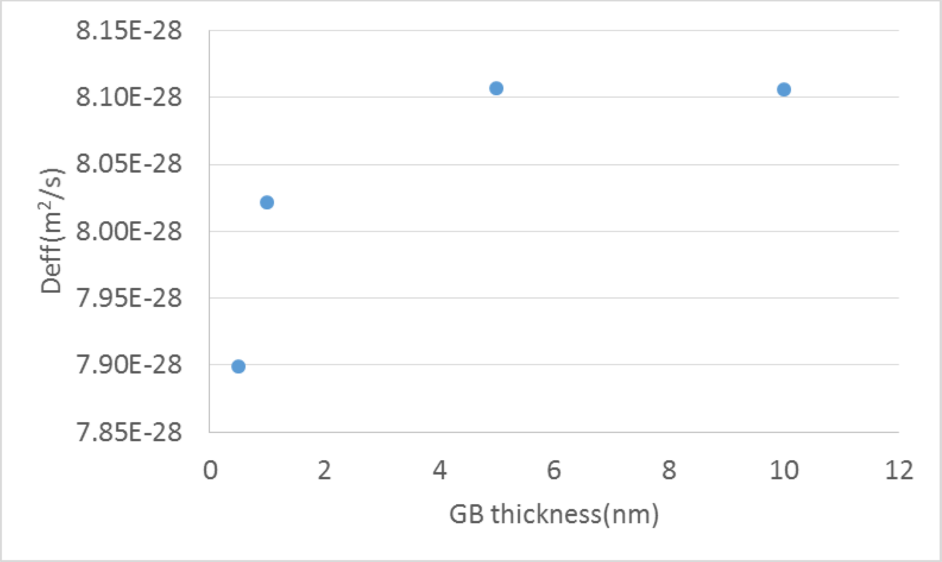

Figure 6-30: The Effective Diffusivity of the $UO_{2.00}$ Model with Respect to GB Thickness.

The Effective diffusivity for $UO_{2.14}$ is plotted in Figure 6-31. Unlike the $UO_{2.00}$ model, the plot shows a larger and linear increase in diffusivity with respect to the GB thickness. The different behavior occurs due to the fact that $UO_{2.14}$ model had a D_{GB}/D_{bulk} ratio less than 10^5, a threshold value suggested in literature for the GB diffusion to be significant. The increase in GB thickness increases the δD_{GB} term, which steadily brings the D_{GB} to D_{bulk} ratio closer or above the threshold value, resulting in the increase in effective diffusivity.

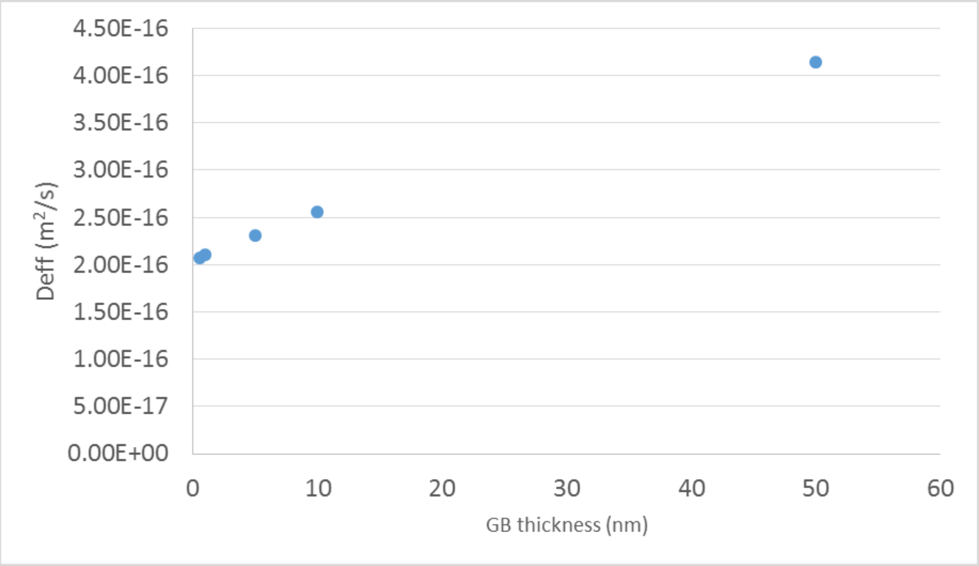

Figure 6-31: The Effective Diffusivity of $UO_{2.14}$ Model with Respect to the GB Thickness.

The four cases listed in Table 6-5 are simulated using the $UO_{2.06}$ microstructure and the mid-radius pellet temperature range, as it was the model that showed ambiguity in the effect of GB, i.e., the effect of GB diminishes under certain conditions. The concentration profile for each case is plotted in Figure 6-32 with cases 1 and 3 overlapping. First of all, the results showed that all cases, except for case 2, have multiple changes in slopes in the concentration profile, showing the effect of GB diffusion. Case 2 with a high bulk diffusivity and a low GB diffusivity has a D_{GB}/D_{bulk} ratio of 420, which is much smaller than the cutoff value of 10^5. The resulting concentration profile is almost a straight line. On the other hand, case 1 and case 3 both have the highest GB diffusivity, but case 3 has a low bulk diffusivity while case 1 has a high bulk diffusivity. The almost identical concentration profiles suggest that the concentration profiles stop changing when the D_{GB}/D_{bulk} exceeds a certain value, which must be equal or smaller than the calculated value of 7.8x10^5 for case 3.

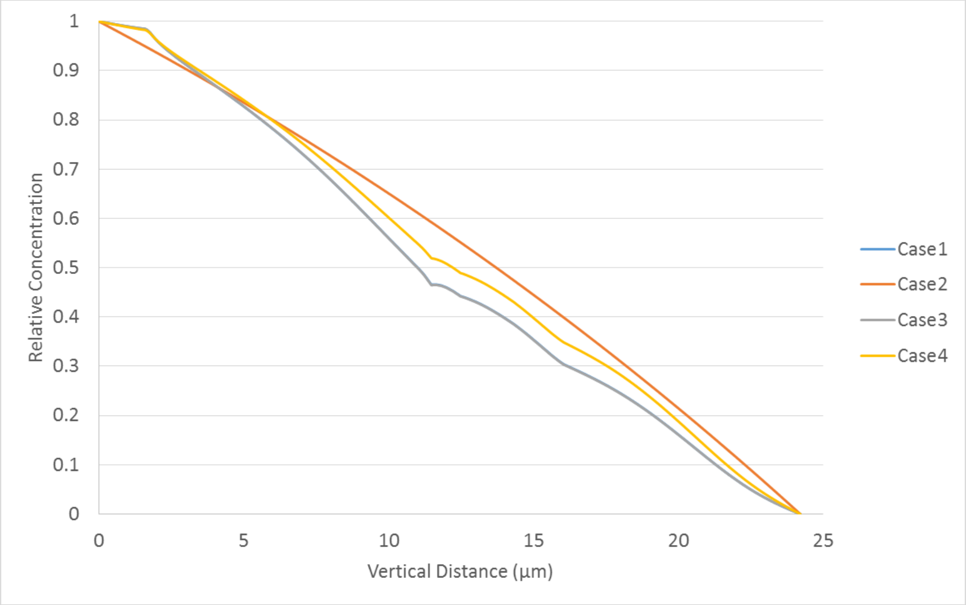

Figure 6-32: The Concentration Profile Plotted Based on the Four Cases Described in Table 6-5 for Sensitivity Analysis.

To summarize, the work presented in this chapter has showed that the GB diffusivity, coupled with heat transfer, can be studied using the developed polycrystalline models, taking into account the different physics, including GB diffusion, GB heterogeneity, temperature gradient, TJ diffusion, Kapitza resistance and UO_2 composition. The physics is fully coupled as the heat transfer is affected by the FG concentration in the GB through the GB Kapitza resistance. The simulation began with bicrystal models to verify assumptions made on GB diffusion and thermal resistance. After it was verified that the 2-D GBs can be used in models of the 3-D microstructure, the effect of each physics is studied independently in the three reconstructed polycrystalline models. With all simulations performed with the same uniform concentration gradient from top to bottom, the resulting concentration profiles can be different depending on the temperature, grain size distribution and the connectivity of high diffusivity GBs. The three microstructures are then used to probe the FG behavior at different radial locations, taking into account the coupling physics and the stoichiometry effect. The results showed that the GB effect is most significant at the edge of a pellet and that GB engineering to control the FGR can be simulated in the region. Lastly, the results from the sensitivity analysis are affected by the D_{GB}/D_{bulk}, in a way that the increase in GB thickness does not further increase the D_{eff} once the cutoff ratio of 10^5 is met. The study of different GB and bulk diffusivity showed that only the lowest collected GB diffusivity in combination with the highest collected bulk diffusivity will negate the effect of GB on the distribution of FGs, again, suggesting the importance of the developed microstructurally explicit models.

7. CONCLUSIONS AND FUTURE WORKS

7.1 Conclusions

The work presented began with background on the behavior of FPs, in general, and FGs, in particular, which is known to affect nuclear fuel performance. Much effort has been dedicated to the field since the 1960s; however, the FP release mechanism is still not fully understood. Although it has been shown that microstructure plays an important role, no computational work has been performed to take into account the effect of complex microstructures and material properties affected by crystallography. The work presented here tries to fill in this gap by developing microstructurally explicit models to simulate the transport behavior of FGs at the early stage of fuel life accounting full geometric and crystallographic features and constraints of actual fuel microstructures.

A finite element modeling framework has been developed to study FGR. The work took advantage of the characterization and modeling capability and developed techniques to conduct 3-D microstructure reconstruction using actual microstructure of UO_2 samples. Three UO_2 samples of different compositions were scanned with EBSD and serial sectioning using FIB. A series of OIM images were obtained for 3-D microstructure reconstruction, which used Dream3D™ and AVIZO™ for a series of image processing, segmentation, visualization and meshing steps. Statistical data have been collected in both 2-D and 3-D, and GB properties were assigned to the meshed models based on GB misorientation angles and CSL types obtained from EBSD data.

Simulations were conducted on the three different microstructures to study the transport behavior of fission product under effect of different microstructures and different physics, including bulk and GB diffusion, GB Kapitza resistance, TJ diffusion, as well as temperature and stoichiometry effects. These effects were coupled in a way that the diffusion process is temperature dependent while the heat conduction is affected by the FGs in the GBs. The coupled physics allowed better understanding of the complex environment in a fuel element. Finally, based on the simulation results, the following conclusions were drawn:

1. The approach of modeling GBs using 2-D elements was verified and compared with 3-D GB models and the results showed that the derived equations can be applied to simulate GB diffusion and GB Kapitza resistance using 2-D elements to save on the computational cost.
2. Effective GB diffusivity models that took the effect of bubble trapping into account were developed and the effective diffusivity as a function of bubble coverage at GBs was derived.
3. The simulations using microstructurally explicit models, assuming all GBs have higher diffusivity than the bulk, showed that the FG distribution is heavily affected by the microstructure. The variation in grain size resulted in a non-uniform FG distribution with high concentration in the large grain regions due to a smaller fraction of GBs.
4. The presence of a temperature gradient that simulates the reactor environment changed the diffusivities for both grain bulk and GB. The higher temperature region resulted in a higher diffusivity and thus a smaller concentration gradient. The distribution of FGs is altered by the temperature effect.

5. Kapitza resistance was incorporated into the polycrystalline models to study the effective thermal conductivity of each microstructure. The effective thermal conductivity is reduced by the GB in each microstructure by about a half percentage. The effect seems small in the size of the model studies but can be significant over a long range due to the cumulative effects of many GBs.
6. A two-level heterogeneous GB property was assigned based on the characterization data to reflect the fact that GBs have different properties due to their different structure. The results suggested that the distribution of FG was no longer affected only by the grain size distribution. The presence of a small fraction (about 30%) of low diffusivity GB was breaking the continuity of high diffusivity GBs and creating many locally high concentration regions. The geometrical orientation of these GBs with respect to the concentration gradient was also an important factor.
7. The presence of TJ diffusion can reduce the non-uniformity in the FG distribution induced by heterogeneous GB properties. The effect is small when all GBs have the same high diffusivity value, but becomes more significant when GBs have different properties.
8. Window methods were applied to probe the FG behavior at different radial positions in a fuel pellet using multi-physics simulations. The microstructure models of the three different samples, $UO_{2.14}$, $UO_{2.06}$ and $UO_{2.00}$, were placed at the center, mid-radius and edge of a fuel pellet to reflect the difference in oxygen content and temperature. The effect of heterogeneous GB properties, GB Kapitza resistance, temperature and oxygen enhanced diffusivity are all considered in

these simulations. The results showed that the GB effect is the most significant from the mid-radius to edge region where high D_{GB}/D_{bulk} ratios are present. In these regions, high concentration regions formed either due to grain size distribution or difference in GB properties. These regions are the likely places where FG bubbles first grow and become interconnected. The locations and the connectivity of the GBs in these regions can provide insights to the development of the interconnected open GBs that lead to the burst release phenomenon.

7.2 Future Work

The work presented here has shown the capabilities of the models to simulate the transport behavior of FGs at low burnup. In the future, different directions can be taken using the developed framework for different studies. First of all, a percolation study can be conducted based on the existing results. Compared with the percolation of high diffusivity GBs, the connectivity of highly concentrated GBs is more important because they will be the GBs that interconnect first and contribute to the later stage of FGR. The work can be combined with the homology metrics that was presented as part of the characterization results. The homology metrics can be applied to the 3-D models to examine the connectivity of different GBs in 3-D. The results, in addition to the percolation study, can provide more precise inputs to the transport of FG from the statistical perspective. Ideally, the work is to be linked with the sample fabrication to test the effect of GB engineering.

The developed model can also be used to examine the experimental FGR data. To do so, the simulation needs to be conducted in a time dependent fashion, and the fractional release for the RVE can be calculated and compared with the samples It is desired to use the model to study the fractional release data for samples irradiated to low burnups. If samples with high burnups are to be studied, the developed effective GB trapping model needs to be applied and the physics of FG flow through the interconnected GBs or TJs needs to be developed.

In addition, the work has so far focused on the coupled relationship between heat and mass transport and ignored the effect of irradiation damage. The models for high burnups will require the incorporation of irradiation damage, which will affect the diffusion behavior of FGs. With the capability of simulating FG behavior from the beginning of fuel life to high burnups, the information will provide inputs to some of the existing fuel performance codes to perform better predictions of the overall FG transport in an actual reactor, as well as its local variability due to microstructure heterogeneity.

REFERENCES

[1] 2012, "Nuclear Power in the World Today."

[2] Olander, D., 2009, "Nuclear fuels - Present and future," Journal of Nuclear Materials, 389(1), pp. 1-22.

[3] Graham Jr, T., Hecker, S. S., Reis, V. H., Moniz, E. J., and Pellaud, B., 2004, "Preventing nuclear proliferation," Issues in Science & Technology, 20(4), pp. 5-9.

[4] Murray, R. L., 2008, Nuclear Energy : An Introduction to the Concepts, Systems, and Applications of Nuclear Processes, Elsevier Science & Technology.

[5] Salvatores, M., Zaetta, A., Girard, C., Delpech, M., Slessarev, I., and Tommasi, J., 1995, "Nuclear waste transmutation," Applied Radiation and Isotopes, 46(6-7), pp. 681-687.

[6] Olander, D., 1976, Fundamental Aspects of Nuclear Reactor Fuel Element, Technical Information Center, Office of Public Affairs Energy Research and Development Administration, United States of America.

[7] Roberts, J. T. A., 1981, Structural materials in nuclear power systems, Plenum Press, New York.

[8] Was, G. S., MyiLibrary, and SpringerLink, 2007, Fundamentals of radiation materials science, Springer, Berlin; New York.

[9] Schaffer, M. B., 2013, "Abundant thorium as an alternative nuclear fuel: Important waste disposal and weapon proliferation advantages," Energy Policy, 60(0), pp. 4-12.

[10] Frost, B. R. T., "- Nuclear fuel elements :design, fabrication, and performance Y1 - 1982," - Pergamon international library of science, technology, engineering, and social studies, pp. - 275.

[11] Pramanik, D., Ravindran, M., Rao, G. V. S. H., and Jayaraj, R. N., "Innovative Process Techniques to Optimize Quality and Microstructure Fuel for PHWRs in India," Proc. Advanced Fuel Pellet Materials and Fuel Rod Design for Water Cooled Reactors, International Atomic Energy Agency.

[12] Hiernaut, J. P., Wiss, T., Papaioannou, D., Konings, R. J. M., and Rondinella, V. V., 2008, "Volatile fission product behaviour during thermal annealing of irradiated UO2 fuel oxidised up to U3O8," Journal of Nuclear Materials, 372(2-3), pp. 215-225.

[13] Cox, B., 1990, "Pellet-clad interaction (PCI) failures of zirconium alloy fuel cladding — A review," Journal of Nuclear Materials, 172(3), pp. 249-292.

[14] King, W. E., Tumey, S. J., Rest, J., and Gilmer, G. H., 2011, "The effect of lattice and grain boundary diffusion on the redistribution of Xe in metallic nuclear fuels: Implications for the use of ion implantation to study fission-gas-bubble nucleation mechanisms," Journal of Nuclear Materials, 415(1), pp. 38-54.

[15] Speight, M. V., Cornell, R. M., and Masters, B. C., 1969, "The role of bubbles in fission gas release," 30, pp. 170-178.

[16] Kim, Y.-s., 2004, "Theoretical analysis of two-stage fission gas release processes: grain lattice and grain boundary diffusion," Journal of Nuclear Materials, 326(2-3), pp. 97-105.

[17] Fisher, S. B., White, R. J., Cook, P. M. A., Bremier, S., Corcoran, R. C., Stratton, R., Walker, C. T., Ivison, P. K., and Palmer, I. D., 2002, "Microstructure of irradiated SBR MOX fuel and its relationship to fission gas release," Journal of Nuclear Materials, 306(2-3), pp. 153-172.

[18] Turnbull, J. A., and Beyer, C. E., 2010, "Background and Derivation of ANS-5 . 4 Standard Fission Product Release Model."

[19] Une, K., and Kashibe, S., 1990, "Fission Gas Release during Post Irradiation Annealing of BWR Fuels," Journal of Nuclear Science and Technology, 27(11), pp. 1002-1016.

[20] Turnbull, J. A., and Friskney, C. A., 1978, "The relation between microstructure and the release of unstable fission products during high temperature irradiation of uranium dioxide," Journal of Nuclear Materials, 71(2), pp. 238-248.

[21] Carbajo, J. J., 2001, "A review of the thermophysical properties of MOX and UO2 fuels," Journal of Nuclear Materials, 299(3), pp. 181-198.

[22] Fink, J. K., 2000, "Thermophysical properties of uranium dioxide," Journal of Nuclear Materials, 279(1), pp. 1-18.

[23] Lawrence, G. T., 1978, "A review of the diffusion coefficient of fission-product rare gases in uranium dioxide," Journal of Nuclear Materials, 71(2), pp. 195-218.

[24] Booth, A. H., 1957, "A method of calculating fission gas diffusion from UO 2 fuel and its application to the X-2-f loop test," (496).

[25] Miekeley, W., and Felix, F. W., 1972, "Effect of stoichiometry on diffusion of xenon in UO2," Journal of Nuclear Materials, 42(3), pp. 297-306.

[26] Turnbull, J. A., Friskney, C. A., Findlay, J. R., Johnson, F. A., and Walter, A. J., 1982, "The diffusion coefficients of gaseous and volatile species during the irradiation of uranium dioxide," Journal of Nuclear Materials, 107(2-3), pp. 168-184.

[27] White, R. J., and Tucker, M. O., 1983, "A new fission-gas release model," Journal of Nuclear Materials, 118(1), pp. 1-38.

[28] Forsberg, K., and Massih, A. R., 1985, "Diffusion theory of fission gas migration in irradiated nuclear fuel UO2," Journal of Nuclear Materials, 135(2–3), pp. 140-148.

[29] Turnbull, J. A., Beyer, C. E., and Commission, U. S. N. R., "- Background and derivation of ANS-5.4 standard fission product release model Y1 - 2010," pp. - 41.

[30] Booth, A. H., 1957, "A METHOD OF CALCULATING FISSION GAS DIFFUSION FROM UO2 FUEL AND ITS APPLICATION TO THE X-2-f LOOP TEST," No. CRDC-721; AECL-496 CanadaWed Dec 12 09:09:04 EST 2012DTIE; NSA-12-000399English, Atomic Energy of Canada Limited Chalk River Project Research and Development.

[31] CORNELL, R., 1969, "GROWTH OF FISSION GAS BUBBLES IN IRRADIATED URANIUM DIOXIDE," Philosophical Magazine, 19(159), pp. 539-&.

[32] Davies, D., Long, G., and United Kingdom Atomic Energy Authority. Research Group. Atomic Energy Research Establishment, H. B. E., 1963, THE EMISSION OF XENON-133 FROM LIGHTLY IRRADIATED URANIUM DIOXIDE SPHEROIDS AND POWDERS, United Kingdom.

[33] MATZKE, H., 1990, "ATOMIC MECHANISMS OF MASS-TRANSPORT IN CERAMIC NUCLEAR-FUEL MATERIALS," Journal of the Chemical Society-Faraday Transactions, 86(8), pp. 1243-1256.

[34] Olander, D. R., and Van Uffelen, P., 2001, "On the role of grain boundary diffusion in fission gas release," Journal of Nuclear Materials, 288(2-3), pp. 137-147.

[35] Millett, P. C., Tonks, M. R., and Biner, S. B., 2012, "Grain boundary percolation modeling of fission gas release in oxide fuels," Journal of Nuclear Materials, 424(1–3), pp. 176-182.

[36] Kaimal, K. N. G., Naik, M. C., and Paul, A. R., 1989, "Temperature dependence of diffusivity of xenon in high dose irradiated UO 2," Journal of Nuclear Materials, 168, pp. 188-190.

[37] Kashibe, S., and Une, K., 1998, "Effect of additives (Cr2O3, Al2O3, SiO2, MgO) on diffusional release of from UO2 fuels," Journal of Nuclear Materials(254), pp. 234-242.

[38] Nicoll, S., Matzke, H., and Catlow, C. R. A., 1995, "A computational study of the effect of Xe concentration on the behaviour of single Xe atoms in UO 2," Journal of Nuclear Materials, 226, pp. 51-57.

[39] 1981, Nonstoichiometric Oxides.

[40] Sutton, A. P., and Balluffi, R. W., 1995, Interfaces in crystalline materials, Clarendon Press, Oxford England.

[41] Shewmon, P., 1989, Diffusion in Solids, TMS, Warrandale, PA.

[42] Porter, D. A., and Easterling, K. E., 1992, Phase transformations in metals and alloys, Chapman & Hall, London ; New York.

[43] Rohrer, G., 2011, "Grain boundary energy anisotropy: a review," Journal of Materials Science, 46(18), pp. 5881-5895.

[44] Pankaj V. Nerikar, K. R., 2011, "Grain Boundaries in Uranium Dioxide: Scanning Electron Microscopy Experiments and Atomistic Simulations," The American Ceramic Society.

[45] Oecd, and Nuclear Energy, A., 2002, Fission Gas Behaviour in Water Reactor Fuels, Organisation for Economic Co-operation and Development.

[46] Fisher, J. C., 1951, "Calculations of diffusion penetration curves for surface and grain boundary diffusion," Journal of Applied Physics, 22(1), pp. 74-77.

[47] Whipple, R. T. P., 1954, "Concentration contours in grain boundary diffusion," Philosophical magazine (Abingdon, England), 45(371), pp. 1225-1236.

[48] Millett, P. C., and Tonks, M., 2011, "Meso-scale modeling of the influence of intergranular gas bubbles on effective thermal conductivity," Journal of Nuclear Materials, 412(3), pp. 281-286.

[49] Stubican, V. S., and Osenbach, J. W., 1984, "Influence of anisotropy and doping on grain boundary diffusion in oxide systems," Solid State Ionics, 12(0), pp. 375-381.

[50] Mishin, Y., and Herzig, C., 1999, "Grain boundary diffusion: recent progress and future research," Materials Science and Engineering: A, 260(1-2), pp. 55-71.

[51] Inderjeet, K., Mishin, Y., and Gust, W., 1995, Fundamentals of grain and interphase boundary diffusion, John Wiley, Chichester; New York.

[52] Fisher, C. A. J., and Matsubara, H., 1999, "The influence of grain boundary misorientation on ionic conductivity in YSZ," Journal of the European Ceramic Society, 19(6-7), pp. 703-707.

[53] Stauffer, D., and Aharony, A., 1992, Introduction to percolation theory, Taylor & Francis, London ; Washington, D.C.

[54] Sahimi, M., 1993, Applications of percolation theory, Taylor & Francis, Bristol, PA.

[55] Chen, Y., and Schuh, C. A., 2006, "Diffusion on grain boundary networks: Percolation theory and effective medium approximations," Acta Materialia, 54(18), pp. 4709-4720.

[56] Frary, M., and Schuh, C. A., 2005, "Grain boundary networks : Scaling laws , preferred cluster structure , and their implications for grain boundary engineering," 53, pp. 4323-4335.

[57] Phillpot, S. R., El-Azab, A., Chernatynskiy, A., and Tulenko, J. S., 2011, "Thermal Conductivity of UO2 Fuel: Predicting Fuel Performance from Simulation," JOM, 63(8), pp. 73-79.

[58] Lucuta, P. G., Matzke, H., and Hastings, I. J., 1996, "A pragmatic approach to modelling thermal conductivity of irradiated UO2 fuel: Review and recommendations," Journal of Nuclear Materials, 232(2–3), pp. 166-180.

[59] Kapitza, P. L., 1941, J Phys (Moscow)(4), p. 181.

[60] Millett, P. C., 2012, "Percolation on grain boundary networks: Application to fission gas release in nuclear fuels," Computational materials science, 53(1), pp. 31-36.

[61] Lim, H. C., Rudman, K., Krishnan, K., Mcdonald, R., Dickerson, P., Byler, D., Peralta, P., Stanek, C., and Mcclellan, K., 2013, "Microstructurally Explicit Simulation of Intergranular Mass Transport in Oxide Nuclear Fuels," Nuclear Technology(182).

[62] Yang, H.-S., Bai, G. R., Thompson, L. J., and Eastman, J. A., 2002, "Interfacial thermal resistance in nanocrystalline yttria-stabilized zirconia," Acta Materialia, 50(9), pp. 2309-2317.

[63] Smith, D. S., Grandjean, S., Absi, J., Kadiebu, S., and Fayette, S., 2003, "Grain-boundary thermal resistance in polycrystalline oxides: alumina, tin oxide, and magnesia," High Temperatures-High Pressures, 35-6(1), pp. 93-99.

[64] Schelling, P. K., Phillpot, S. R., and Keblinski, P., 2004, "- Kapitza conductance and phonon scattering at grain boundaries by simulation," - 95(- 11), pp. - 6091.

[65] Chockalingam, K., Millett, P. C., and Tonks, M. R., 2012, "Effects of intergranular gas bubbles on thermal conductivity," Journal of Nuclear Materials, 430(1–3), pp. 166-170.

[66] Chen, Y., and Schuh, C. A., 2007, "Contribution of triple junctions to the diffusion anomaly in nanocrystalline materials," Scripta Materialia, 57(3), pp. 253-256.

[67] Bokstein, B., Ivanov, V., Oreshina, O., Peteline, A., and Peteline, S., 2001, "Direct experimental observation of accelerated Zn diffusion along triple junctions in Al," Materials Science and Engineering: A, 302(1), pp. 151-153.

[68] Christopher, S., Roger, M., and Mukul, K., 2003, "Connectivity and percolation in simulated grain-boundary networks," Philosophical Magazine, 83(6), pp. 711-726.

[69] Schuh, C. a., Kumar, M., and King, W. E., 2003, "Analysis of grain boundary networks and their evolution during grain boundary engineering," Acta Materialia, 51(3), pp. 687-700.

[70] Frary, M., and Schuh, C. A., 2005, "Grain boundary networks: Scaling laws, preferred cluster structure, and their implications for grain boundary engineering," Acta Materialia, 53(16), pp. 4323-4335.

[71] Sørensen, O. T., "- Nonstoichiometric oxides Y1 - 1981," - Materials science and technology8, pp. - 441.

[72] Speight, M. V., 1969, "A calculation on the migration of fission gas in material exhibiting precipitation and re-solution of gas atoms under irradiation," Nucl. Sci. Eng.

[73] Turnbull, J. A., 1974, "The effect of grain size on the swelling and gas release properties of uo 2 during irradiation," Journal of Nuclear Materials, 50, pp. 62-68.

[74] Tonks, M. R., Millett, P. C., Nerikar, P., Du, S., Andersson, D., Stanek, C. R., Gaston, D., Andrs, D., and Williamson, R., 2013, "Multiscale development of a fission gas thermal conductivity model: Coupling atomic, meso and continuum level simulations," Journal of Nuclear Materials, 440(1–3), pp. 193-200.

[75] Liu, X. Y., Andersson, D. a., and Uberuaga, B. P., 2012, "First-principles DFT modeling of nuclear fuel materials," Journal of Materials Science, 47(21), pp. 7367-7384.

[76] Andersson, D. A., Garcia, P., Liu, X. Y., Pastore, G., Tonks, M., Millett, P., Dorado, B., Gaston, D. R., Andrs, D., Williamson, R. L., Martineau, R. C., Uberuaga, B. P., and Stanek, C. R., 2014, "Atomistic modeling of intrinsic and radiation-enhanced fission gas (Xe) diffusion in : Implications for nuclear fuel performance modeling," Journal of Nuclear Materials, 451(1–3), pp. 225-242.

[77] Chartier, a., Van Brutzel, L., and Freyss, M., 2010, "Atomistic study of stability of xenon nanoclusters in uranium oxide," Physical Review B, 81(17), pp. 174111-174111.

[78] Nerikar, P. V., Rudman, K., Desai, T. G., Byler, D., Unal, C., McClellan, K. J., Phillpot, S. R., Sinnott, S. B., Peralta, P., Uberuaga, B. P., and Stanek, C. R., 2011, "Grain Boundaries in Uranium Dioxide: Scanning Electron Microscopy Experiments and Atomistic Simulations," Journal of the American Ceramic Society, 94(6), pp. 1893-1900.

[79] Millett, P. C., Tonks, M. R., Biner, S. B., Zhang, L., Chockalingam, K., and Zhang, Y., 2012, "Phase-field simulation of intergranular bubble growth and percolation in bicrystals," Journal of Nuclear Materials, 425(1-3), pp. 130-135.

[80] Millett, P. C., Tonks, M. R., Chockalingam, K., Zhang, Y., and Biner, S. B., 2013, "Three dimensional calculations of the effective Kapitza resistance of UO2 grain boundaries containing intergranular bubbles," Journal of Nuclear Materials, 439(1–3), pp. 117-122.

[81] Rudman, K., Krishnan, K., Peralta, P., Stanek, C., and McClellan, K., 2014, "Statistics of Grain Boundary Crystallography in Surrogates for Oxide Nuclear Fuels and its Effects on Mass Transport: 2-D Measurements and Preliminary Models," Journal of Nuclear Materials (to be submitted).

[82] Rudman, K., Dickerson, P., Byler, D., McDonald, R., Lim, H., Peralta, P., Stanek, C., and McClellan, K., 2013, "Three-Dimensional Characterization of Sintered UO 2: Effects of Oxygen Content on Microstructure and Its Evolution," Nuclear Technology, 182, pp. 145-145.

[83] Rudman, K., 2014, "EFFECT ON PROCESSING CONDITION ON GRAIN BOUNDARY CHARACTER DISTRIBUTION AND MOBILITY IN OXIDE NUCLEAR FUELS " Doctor of Philosophy, Arizona State University.

[84] Rudman, K., Dickerson, P., Byler, D., McDonald, R., Lim, H., Peralta, P., Stanek, C., and McClellan, K., 2013, "THREE-DIMENSIONAL CHARACTERIZATION OF SINTERED UO2+x: EFFECTS OF OXYGEN CONTENT ON MICROSTRUCTURE AND ITS EVOLUTION," Nuclear Technology, 182(2), pp. 145-154.

[85] 2012, "EDAX OIM Analysis User Manual."

[86] Rohrer, G. S., 2011, "Grain boundary energy anisotropy: a review," Journal of Materials Science, 46(18), pp. 5881-5895.

[87] Khorashadizadeh, a., Raabe, D., Zaefferer, S., Rohrer, G. S., Rollett, a. D., and Winning, M., 2011, "Five-Parameter Grain Boundary Analysis by 3D EBSD of an Ultra Fine Grained CuZr Alloy Processed by Equal Channel Angular Pressing," Advanced Engineering Materials, 13(4), pp. 237-244.

[88] Rohrer, G. S., and Miller, H. M., 2010, "Topological characteristics of plane sections of polycrystals," Acta Materialia, 58(10), pp. 3805-3814.

[89] Gottstein, G., and Shvindlerman, L. S., 1999, Grain boundary migration in metals : thermodynamics, kinetics, applications, CRC Press, Boca Raton, Fla. ; London.

[90] Zhao, B., Gottstein, G., and Shvindlerman, L. S., 2011, "Triple junction effects in solids," Acta Materialia, 59(9), pp. 3510-3518.

[91] William, K., and Pilarczyk, P., 2004, "Computational homology program."

[92] Ghosh, S., Bhandari, Y., and Groeber, M., 2008, "CAD-based reconstruction of 3D polycrystalline alloy microstructures from FIB generated serial sections," Computer-Aided Design, 40(3), pp. 293-310.

[93] Uchic, M. D., Groeber, M. A., and Rollett, A. D., 2011, "Automated Serial Sectioning Methods for Rapid Collection of 3-D Microstructure Data," JOM, 63(3), pp. 25-29.

[94] Lim, H. C., Rudman, K., Krishnan, K., McDonald, R., Dickerson, P., Byler, D., Peralta, P., Stanek, C., and McClellan, K., 2013, "MICROSTRUCTURALLY EXPLICIT SIMULATION OF INTERGRANULAR MASS TRANSPORT IN OXIDE NUCLEAR FUELS," Nuclear Technology, 182(2), pp. 155-163.

[95] King, W. E., Robel, M., and Gilmer, G. H., 2011, "The potential to use fission gas release experiments to measure lattice and grain boundary diffusion in metallic fuels," Journal of Nuclear Materials, 411(1-3), pp. 97-111.

[96] Klinger, L. M., Levin, L., and Petelin, A., 1997, "The model of triple junction diffusion," Defect and diffusion forum.

[97] Thornton, E., 1960, "Viscosity and Thermal Conductivity of Binary Gas Mixtures: Xenon-Krypton, Xenon-Argon, Xenon-Neon and Xenon-Helium," Proceedings of the Physical Society, 76(1), p. 104.

[98] Davies, D., and Long, G., 1963, "The emission of xenon-133 from lightly irradiated uranium dioxide spheroids and powders," United Kingdom Atomic Energy Authority Research Group Report.

[99] Matzke, H. J., 1980, "Gas release mechanisms in UO 2 —a critical review," Radiation Effects, 53(3-4), pp. 219-242.

[100] Mansouri, M. A., and Olander, D. R., 1998, "Fission product release from trace irradiated UO 2+ x," Journal of nuclear materials, pp. 22-33.

[101] Davies, D., Long, G., and United Kingdom Atomic Energy Authority. Research Group. Atomic Energy Research Establishment, H. B. E., 1963, The Emission of Xenon-133 From Lightly Irradiated Uranium Dioxide Spheroid And Powders, United Kingdom.

[102] Kogai, T., 1997, "Modelling of fission gas release and gaseous swelling of light water reactor fuels," Journal of nuclear materials, i, pp. 131-140.

[103] Reynolds, G. L., and Burton, B., 1979, "Grain-boundary diffusion in uranium dioxide: the correlation between sintering and creep and a reinterpretation of creep mechanism," Journal of Nuclear Materials, 82, pp. 22-25.

[104] Govers, K., Lemehov, S. E., and Verwerft, M., 2012, "Molecular Dynamics Study of Grain Boundary Diffusion of Fission Gas in Uranium Dioxide," Defect and Diffusion Forum.

[105] Ma, Q., and Balluffi, R. W., 1993, "Diffusion along [001] tilt boundaries in the Au/Ag system—I. Experimental results," Acta Metallurgica et Materialia, 41(1), pp. 133-141.

[106] Duderstadt, J. J., and Hamilton, L. J., 1976, "- Nuclear reactor analysis," (1), pp. -650.

[107] Walker, C. T., and Lassmann, K., 1986, "Fission gas and caesium gradients in single grains of transient tested UO2 fuel: Results of an EPMA investigation," Journal of Nuclear Materials, 138(2–3), pp. 155-161.

[108] White, R. J., 2004, "The development of grain-face porosity in irradiated oxide fuel," Journal of Nuclear Materials, 325(1), pp. 61-77.

[109] Kashibe, S., and Une, K., 1991, "Effects of Temperature Cycling and Heating Rate on Fission Gas Release of BWR Fuels," Journal of Nuclear Science and Technology, 28(12), pp. 1090-1099.

[110] Kashibe, S., Une, K., and Nogita, K., 1993, "Formation and growth of intragranular fission gas bubbles in UO2 fuels with burnup of 6–83 GWd/t," Journal of Nuclear Materials, 206(1), pp. 22-34.

[111] Chen, Y., and Schuh, C., 2006, "Diffusion on grain boundary networks: Percolation theory and effective medium approximations," Acta Materialia, 54(18), pp. 4709-4720.

[112] Swaroop, S., Kilo, M., Argirusis, C., Borchardt, G., and Chokshi, A. H., 2005, "Lattice and grain boundary diffusion of cations in 3YTZ analyzed using SIMS," Acta Materialia, 53(19), pp. 4975-4985.

[113] Lim, H. C., Rudman, K., and Krishnan, K., 2013, "Microstructurally Explicit Simulation of Intergranular Mass Transport in Oxide Nuclear Fuels," Nuclear Technology, pp. 155-163.

[114] Frary, M., and Schuh, C. a., 2003, "Combination rule for deviant CSL grain boundaries at triple junctions," Acta Materialia, 51(13), pp. 3731-3743.

[115] Gao, Y. X., Yi, J. Z., Lee, P. D., and Lindley, T. C., 2004, "A micro-cell model of the effect of microstructure and defects on fatigue resistance in cast aluminum alloys," Acta Materialia, 52(19), pp. 5435-5449.